Multi-photon decay mode spectroscopy of positronium

Storm Johnson

Supervisors: Dr. Tom Leadbeater and Dr. Pete Jones

Dissertation submitted to the University of Cape Town in fulfilment of the degree of Master of Science (Physics)

Department of Physics
University of Cape Town

September 2021

Plagiarism declaration

I know the meaning of plagiarism and declare that all of the work in the dissertation, save for that which is properly acknowledged, is my own.

Date: September 2021

Signed: Signed by candidate

Storm Johnson

Multi-photon decay mode spectroscopy of positronium

Storm Johnson

Supervisors: Dr. Tom Leadbeater and Dr. Pete Jones

Abstract

An approximation for the branching ratio of the four-photon decay of parapositronium ($BR_{4\gamma}$) was measured using a multi-gamma-ray spectrometer. For the first time in such measurements, the spectrometer consisted of an array of eight identical $LaBr_3$:Ce scintillator detectors, each of which combines good energy resolutions (5% and 10% at 511 keV for the signals from the eighth dynode and anode of the photomultiplier tube, respectively) with an excellent timing resolution ($\sim$ 300 ps). These energy resolutions were minimised through an optimal selection of the digital signal processing parameter settings. The detectors were situated in a planar geometry, where the source-to-detector distance of the detector system was selected such that the effect of peak pulse pile-up was minimised (to less than 3%), while maximising the full-energy peak detection efficiency at 511 keV (to 3%). For this work, locally-produced ^{22}Na radioactive sources were used as positron emitters, which enabled the formation of positronium and subsequent gamma decays. Energy calibration measurements were performed using a ^{152}Eu source, where the prominent energy peaks of (121.8, 244.7, 344.3, 778.9, 964.1, 1408.0) keV were used for calibration. For the $BR_{4\gamma}$ measurement, 5×10^{11} events were accumulated over a measurement period of 60 days, which resulted in low statistical uncertainties for the coincident counting between detector pairs (less than 1%). Through simplifying assumptions that neglected the background corrections and efficiency normalisations for each of the 2γ and 4γ decays, a first order approximation of $BR_{4\gamma}$ was determined as the ratio between measured 4γ events ($N_{4\gamma}$) and measured 2γ events ($N_{2\gamma}$), such that $BR_{4\gamma} \sim \frac{N_{4\gamma}}{N_{2\gamma}} = 4.8\ (19) \times 10^{-7}$. This measured value of $BR_{4\gamma}$ differs from previous measurements and accepted literature values by a factor of 3.

Acknowledgements

I would like to thank all those who assisted me with this research, and in particular, to my supervisors Dr. Pete Jones and Dr. Tom Leadbeater. Their guidance and consultation during these pandemic-ridden times were invaluable. They allowed me enough leeway to steer this research in the direction I wanted to go, while offering sound advice and constructive criticism to constantly improve. This research would not have been possible without them.

A special thanks goes to Mike van Heerden of the PEPT facility at iThemba LABS. Upon request, he kindly found the time to produce several ^{22}Na radioactive sources of various activities, each of which were used in various measurements of this research. His contribution is much appreciated.

I thank iThemba LABS for providing the equipment and facilities required to perform the necessary measurements and analyses for this research. Without these contributions, this research would not have been possible. I am also thankful for the opportunities provided by iThemba LABS (and in particular, the SAINTS program) to attend numerous workshops and conferences, which allowed me to develop my skills as a scientist, as well as present my research to the scientific community.

I thank ARMSCOR for providing the necessary funding for the completion of my degree. In addition, I thank iThemba LABS for their top-up funding which I received for the first year of my study.

I am grateful to the good students and staff at iThemba LABS for providing a friendly work environment, especially to Abraham Avaa, Munirat Bashir, Doris Kenfack, Lumkile Msebi, Maluba Vernon Chisapi, and Ferdie van Niekerk for always being willing to critically discuss aspects of this research, as well as providing their input where required.

Lastly, I am grateful to all of my friends and family. Their constant love and support provided the necessary motivation to complete this research.

Dedications

I dedicate this work to my mother for her love and support throughout this research. I also dedicate this work to my late grandmother, late grandfather, and late father for their love and guidance throughout my physical and emotional development.

Contents

List of Figures

List of Tables

1 Introduction

1.1 Background

Positrons (e^+) are the positively-charged anti-particles of electrons (e^-). Due to the prevalence of electrons in matter, free positrons are often not observed to exist for prolonged periods of time (since they quickly undergo annihilation). Following emission from a decay, a positron travelling through a medium will undergo a series of collisions with bound electrons, causing it to thermalise. Once sufficiently thermalised, the positron will undergo either one of two processes: direct annihilation with an electron of opposing spin, or it will form an exotic atom known as positronium (Ps). Ps is a quasi-stable system consisting of an electron and a positron. After a finite period of time, the two particles annihilate to produce an even or odd number of gamma-rays (depending on the relative spin states of each particle, as well as the governing energy, momentum, and charge conservation laws).

Similar to that of hydrogen, the ground state of Ps has two varieties: parapositronium (p-Ps), which is a singlet state with total spin $S = 0$, and orthopositronium (o-Ps), which is a triplet state with total spin $S = 1$.

The Ps state can be considered non-relativistically as the product of an orbital wave function and a spin vector given as,

$$\Psi_{n,l,m}(\mathbf{r})|S, S_z\rangle. \tag{1.1}$$

The orbital wave function in equation (1.1) is the wave function of the hydrogen atom (with the electron mass replaced by the reduced mass of the e^+e^- pair), where n, l, and m are the usual principal ($n \in \mathbb{Z} \geq 0$), orbital ($0 \leq l < n - 1$) and magnetic ($m \leq l$) quantum numbers, respectively. The spin vectors are linear combinations of products of those of the individual particles, of which there are four possible:

$$\begin{aligned}
|S = 1, S_z = 1\rangle &= |\uparrow\rangle|\uparrow\rangle \\
|S = 1, S_z = 0\rangle &= \frac{1}{\sqrt{2}}\left(|\uparrow\rangle|\downarrow\rangle + |\downarrow\rangle|\uparrow\rangle\right) \\
|S = 1, S_z = -1\rangle &= |\downarrow\rangle|\downarrow\rangle \\
|S = 0, S_z = 0\rangle &= \frac{1}{\sqrt{2}}\left(|\uparrow\rangle|\downarrow\rangle - |\downarrow\rangle|\uparrow\rangle\right)
\end{aligned} \tag{1.2}$$

The first three expressions describe the possible spin states of o-Ps (triplet), while the last expression describes the spin state of p-Ps (singlet). In the absence of external electric and magnetic fields, it is reasonable to expect that p-Ps and o-Ps be produced in the ratio 1:3, respectively. Indeed, this is observed for liquids [1]. Mogensen & Jacobsen [2] have also explored some of the cases in which this ratio is not observed.

The selection rule that governs the e^+e^- annihilation [3, 4] is of particular importance in the understanding of the decay modes of Ps. As a direct consequence from the selection rule and the energy, momentum, and charge conservation laws, it can be shown that p-Ps must decay into an even number of photons (two or more), while o-Ps must decay into an odd number (three or more). This is shown succinctly by Harpen [5].

While p-Ps can decay into any even number of photons, the probability of higher order decays rapidly decreases with the number of photons produced in the decay (the branching ratio for decays producing four or more gamma-rays is on the order of 10^{-6} or lower [6]). In the centre-of-mass frame, p-Ps therefore decays preferentially into two back-to-back 511 keV gamma-rays.

For the case of o-Ps, again the probability of higher order decays decreases with the number of photons produced. The leading order decay of o-Ps is the 3γ decay, with the other higher modes of decay having branching ratios of less than 10^{-6} [6].

As an illustration, Fig. 1.1 shows the decay schemes for both the leading order and next-to-leading order annihilations of p-Ps and o-Ps.

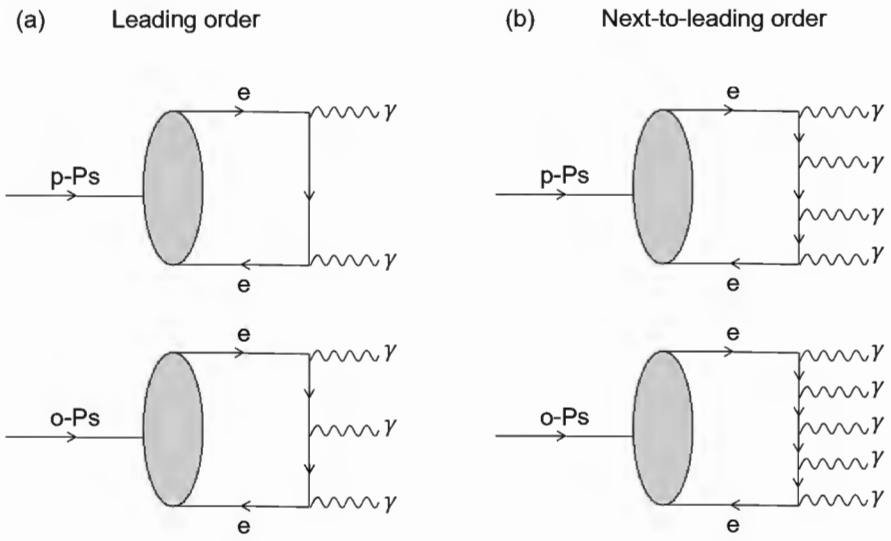

Fig. 1.1: Decay schemes for the (a) leading order, and (b) next-to-leading order annihilations of p-Ps and o-Ps, respectively. This image was adapted from Czarnecki & Karshenboim [6].

As a positron emitter, a ^{22}Na radioactive source provides a good way to study the decay modes of Ps. From the decay scheme of ^{22}Na in Fig. 1.2, it is seen that the majority of radiation produced from the decay of ^{22}Na leads to β^+ emission (90.3%). β^+ emission is important in the context of this investigation, as the emitted β^+ particles interact with electrons in surrounding material, which allow for the formation of Ps, and the subsequent decay into gamma-rays. This is further discussed in Section 2.

1.2 Aim and objectives

The ultimate aim of this study is to demonstrate the measurement feasibility of the four-photon branching ratio of p-Ps. This is accomplished using an array of eight identical 2×2" Lanthanum Bromine ($LaBr_3$:Ce) detectors (set-up in an ideal planar geometry as shown in Fig. 1.3) to study the gamma radiation produced from ^{22}Na radioactive sources of various activities. Listed below is a step-by-step breakdown of the main objectives which were imperative in achieving this aim. These include:

1. Evaluation of the digital signal processing (DSP) parameter settings (specifically, the decay constants and pulse shape parameters) which correspond to minimum energy resolutions. The minimum energy resolutions for this work were found to be 5% and 10% at 511 keV for the energy and timing signals, respectively.

2. Characterisation of the $LaBr_3$:Ce detectors in terms of detection efficiency, dead time, peak pulse pile-up, count rate capabilities and energy resolution of the photopeaks. Since each of the eight detectors are identical, these analyses were performed on measurements

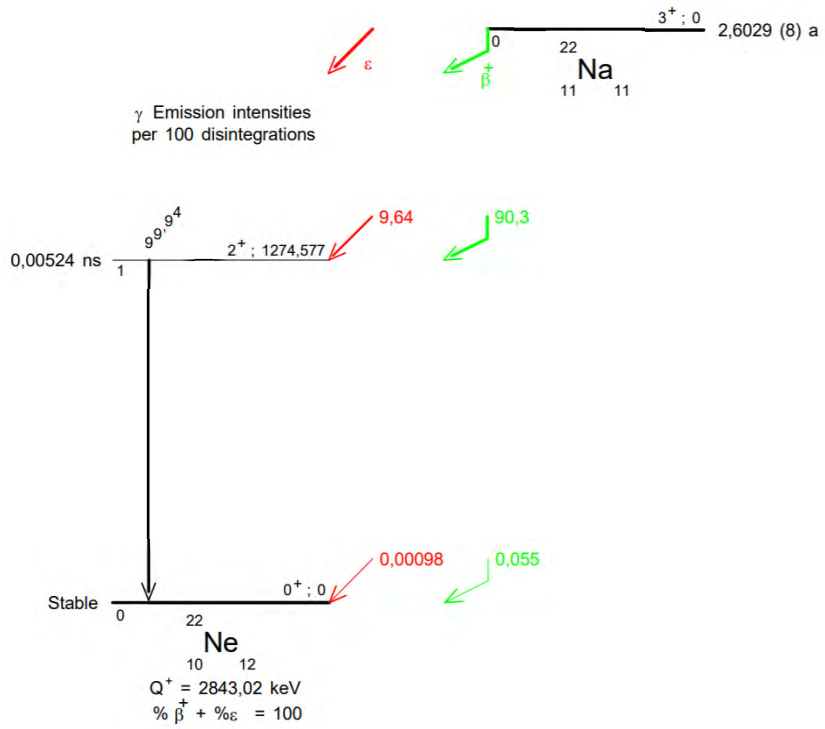

Fig. 1.2: Decay scheme for ^{22}Na, which shows the emission of β^+ particles (positrons) as the main mode of decay. The production of these positrons is what allows Ps to be formed, and subsequently decay into two (or more) gamma-rays. This image was adapted from Bé *et al.* [7]

acquired using a single detector (the findings of which were then assumed to apply for each of the eight detectors).

3. Evaluation of the optimal source-to-detector distance which maximises detection efficiency, while minimising the effect of peak pulse pile-up.

4. Assembly of a detector system using the eight $LaBr_3$:Ce detectors situated in an ideal planar geometry. The optimal source-to-detector distance obtained from step 3 informs the distance between the source relative to the face of each detector.

5. Performance of energy calibrations using the energy peaks of a ^{152}Eu radioactive source as reference. The prominent energy peaks of (121.8, 244.7, 344.3, 778.9, 964.1, 1408.0) keV were used for the calibration of each of the eight detectors.

6. Conduction of main measurement using several ^{22}Na sources of various activities. The specific measurement information for each run of this work are detailed in Table 3.1.

7. Development of a sorting code which reduces the acquired list-mode data. This is accomplished by the establishment of energy and time filter conditions, which organise the data into a binned distribution of detector multiplicities. This method of data reduction is detailed in Section 3.6, while the binning process is described in Section 5.1.

8. Performance of the 4γ branching ratio calculation to obtain an order of magnitude estimate. This estimate is compared to measurements obtained from similar previous experiments performed by Adachi *et al.* in 1990 [8], von Busch *et al.* [9] and Adachi *et al.* [10] in 1994, Yang *et al.* in 1996 [11], and Vetter & Freedman in 2002 [12].

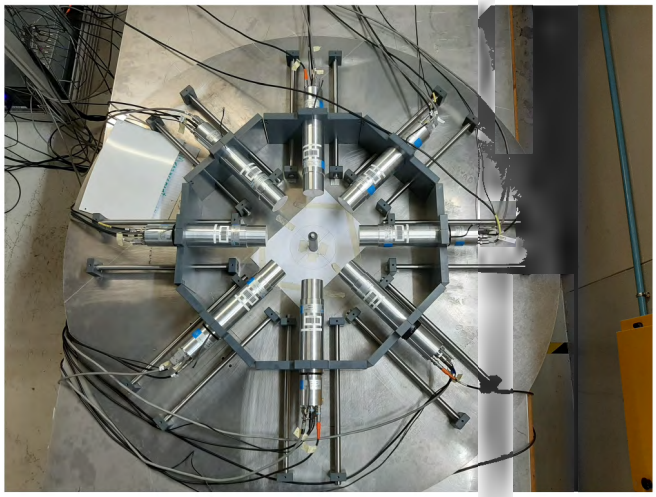

Fig. 1.3: An array of eight identical 2×2" $LaBr_3$:Ce detectors arranged in a planar geometry. The ^{22}Na source was placed in the centre of the array, which ensured an equal exposure of radiation distribution across the face of each detector.

1.3 Dissertation overview

The dissertation is structured as follows:

- Section 2 provides a review of the fundamental concepts and core theory behind this work. It reviews Ps formation and its subsequent decay into gamma-rays, as well as the mechanisms for gamma interactions with matter. The structure and response of an inorganic scintillator when exposed to gamma-ray radiation is also reviewed, along with key gamma-ray spectrometry concepts including energy resolution, detection efficiency, dead time, peak pulse pile-up effects, peak-to-total and peak-to-Compton ratios. Also discussed are the origins of the signals (energy and timing) that are generated from the $LaBr_3$:Ce detectors used in this work.

- Section 3 provides the specific details of the main measurement of this work, as well as the detector assembly, electronic configuration, and data acquisition system. Also discussed is the minimisation of energy resolutions of the energy, timing and charge-to-digital converter (QDC) signals, which provides the optimal DSP parameter settings that were used for the main measurement. Energy and timing calibrations are demonstrated, along with a discussion on the energy and timing filter conditions that were used for data reduction. The method used for background subtraction from energy spectra (using the ^{22}Na and ^{152}Eu spectra as examples) is also discussed.

- Section 4 provides characterisation for a single $LaBr_3$:Ce detector in terms of detection efficiencies, count rates, peak pulse pile-up effects, and dead time. The detection efficiencies from both measurement and theoretical calculation are compared as functions of energy and source-to-detector distance. In addition, the count rate capabilities and peak pulse pile-up effects of the detector are determined as a function of source-to-detector distance, and the effect of high count rates on the energy resolution of the 511 keV peak of ^{22}Na is also investigated. In combination, these measurements provide a way of determining a source-to-detector distance which minimises the effect of peak pile-up, while maximising detector count rate and detection efficiency.

- Section 5 shows the analyses of the list-mode data obtained from the main experiment of this work. Details of the generation of multiplicity plots from the acquired data are discussed, including a step-by-step breakdown of the sorting code used to analyse and filter

the data. Also discussed are the uncertainty calculations (both statistical and systematic) that were performed to obtain uncertainty estimations for the counts presented in the multiplicity spectra. An estimation of the four-photon branching ratio of p-Ps is also performed based on the equation from Vetter & Freedman [12]. This estimated value for the branching ratio is compared to the accepted value, as well as previous measurements from similar experiments [8–12].

- Section 6 concludes with a summary of the key results and calculations performed. Also provided are a few recommendations for improvement of this work's measurement, as well as considerations for possible future work.

2 Theory

This section reviews several theoretical concepts which are relevant to this dissertation. The formation and subsequent decay modes of Ps are discussed. Since this work involves the measurement of gamma-rays through gamma-ray spectroscopy, it would thus also prove useful to revisit some of the more fundamental concepts involved with this type of measurement. It is important to understand how gamma-rays interact with material, and how materials (in particular, scintillators) behave when exposed to gamma-ray radiation. Gamma-ray spectrometry concepts such as energy resolution, detection efficiency, dead time, peak pulse pile-up effects, peak-to-total and peak-to-Compton ratios are also reviewed.

2.1 Formation of positronium

When studying rare annihilation events, such as the subject of this work, positrons are typically produced through radioactive isotopes. Because of their relatively long half-lives, the most commonly-used examples of such isotopes include ^{22}Na (used in a similar experiment by von Busch *et al.* [9]) and ^{68}Ge/^{68}Ga (used in similar experiments by Adachi *et al.* [8, 10], Yang *et al.* [11], and Vetter & Freedman [12]). The development of variable-energy (typically 10 eV to 100 keV) positron beams has provided an alternative method for producing positrons in positron annihilation spectroscopy studies [13].

Following the production of positrons, there is a thermalization process which occurs as the positrons travel through a medium. The positrons rapidly lose their kinetic energy through a series of collisions with bound electrons of the medium until they each possess energies that are a fraction of an eV [14]. This thermalization process is typically completed over a few picoseconds [15]. A thermalized positron will then either undergo direct annihilation with an electron of opposing spin, or it will form Ps with a host electron in the medium. The probability of a positron forming Ps is dependent on the medium through which it travels. Castellaz *et al.* [1] showed that for positrons travelling through various liquids, the Ps yield can range from 38% (water) to as high as 70% (organic solvents).

As mentioned previously, Ps comes in two varieties, namely p-Ps and o-Ps. In a vacuum, the lifetime of p-Ps is 123 ps, while the lifetime of o-Ps is 142 ns [16]. The expected ratio of forming p-Ps to o-Ps is 1:3, since p-Ps is a singlet state and o-Ps is a triplet state (see equation (1.2)). However, as a result of the comparatively longer lifetime of o-Ps, it is often observed that the positron of the o-Ps annihilates with an electron from the surrounding medium of opposing spin before the o-Ps annihilation process is completed. This "pick-off" process results in the emission of two gamma-rays, and it may explain why the ratio 1:3 is not observed in some cases [17]. These "pick-off" effects were explored by Kobayashi *et al.* [16].

2.2 Decays of parapositronium

Using QED theory, Czarnecki [6] calculates the decay rate for the ground state of p-Ps in terms of a series of $\alpha = e^2/4\pi \approx 1/137$. The two-photon decay rate is given by,

$$\begin{aligned}\Gamma(\text{p-Ps} \to \gamma\gamma) &= \frac{m_e\alpha^5}{2}\left[1 - \left(5 - \frac{\pi^2}{4}\right)\frac{\alpha}{\pi} + 2\alpha^2 \ln\frac{1}{\alpha} + 1.75(30)\left(\frac{\alpha}{\pi}\right)^2 - \frac{3\alpha^3}{2\pi}\ln^2\frac{1}{\alpha} + \mathcal{O}\left(\alpha^3 \ln\frac{1}{\alpha}\right)\right] \\ &= 7989.50(2)\ \mu s^{-1}.\end{aligned}$$

Czarnecki notes that the four-photon branching ratio is then given by,

$$\text{BR}_{4\gamma,theory} = \frac{\Gamma(\text{p-Ps} \to \gamma\gamma)}{\Gamma(\text{p-Ps} \to 4\gamma)} = 0.277\ (1)\left(\frac{\alpha}{\pi}\right)^2 = 1.4388\ (21) \times 10^{-6}, \tag{2.1}$$

with the final value obtained from Vetter [18]. This theoretical branching ratio (2.1) is quite significant, as it will later be revisited and compared to the measurements of this work.

2.3 Gamma-ray interactions with matter

A gamma-ray is a form of short-wavelength, high-frequency electromagnetic radiation that is emitted from the radioactive decay of atomic nuclei. These decays include alpha (α) and beta (β^+ and β^-) particle emission, as well as electron capture.

Although there are several ways in which gamma-rays are known to interact with matter, predominantly there are three major interaction mechanisms which significantly influence radiation measurement at relatively low energies, namely photoelectric absorption, Compton scattering and pair production. Each of these processes result in either a complete or partial transfer of the gamma-ray energy to an electron.

This section serves to expand on each of these fundamental processes, which will then provide the basis for understanding how gamma-rays are measured using detectors.

2.3.1 Photoelectric absorption

The photoelectric absorption process occurs when an incident gamma-ray interacts with an atom possessing a bound orbital electron. During this interaction, the energy of the incident photon is fully transferred to the atom, which changes its atomic energy levels, and results in the electron being ejected from one of the atomic shells (typically the K shell [19]). This process is schematically shown in Fig. 2.1.

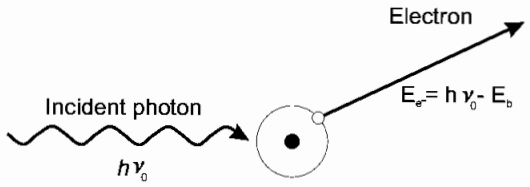

Fig. 2.1: Sketch of the photoelectric absorption process. The incident gamma-ray possesses an initial energy of $h\nu_0$. After interaction between the photon and atom, the bound electron is ejected from the orbital shell of the atom with an energy given by equation (2.2). This image was adapted from Roldan [20].

The energy of the ejected electron is given by [19],

$$E_{e^-} = h\nu_0 - E_b, \tag{2.2}$$

where $h\nu_0$ is the energy of the incident gamma-ray and E_b is the binding energy of the electron to its orbital shell.

Photoelectric absorption is the main form of interaction for gamma-ray energies ranging from 1 keV to 0.5 MeV [19].

2.3.2 Compton scattering

The Compton scattering process occurs between an incident gamma-ray and an electron. This electron is typically loosely-bound to the orbital shell of an atom. Fig. 2.2 shows a schematic of this process, where an incident gamma-ray of energy $h\nu$ scatters off the electron at an angle θ. The scattered photon loses energy in this interaction, while the recoil electron gains this lost energy as kinetic energy.

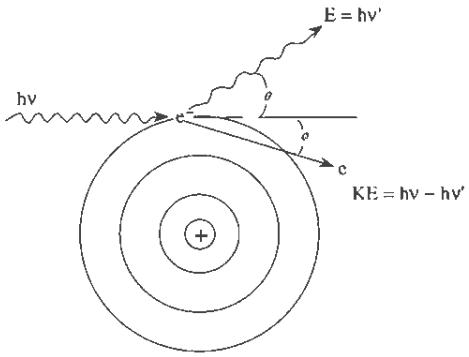

Fig. 2.2: Sketch of the Compton scattering process. An incident gamma-ray of energy $h\nu$ scatters off a loosely-bound electron at an angle of θ. The recoil electron scatters at an angle of ϕ, and has a kinetic energy given as $h\nu - h\nu'$. The scattered photon has an energy given by equation (2.3). This image was adapted from Martin & Wen [21].

The energy of the scattered photon can be derived from simultaneous equations of the conservation of energy and momentum. Using the symbols defined in Fig. 2.2, the energy of the scattered photon is given by [19, 21–23],

$$h\nu' = \frac{h\nu}{1 + \frac{h\nu}{m_0 c^2}(1 - \cos\theta)}, \tag{2.3}$$

where $m_0 c^2$ is the rest-mass energy of the electron. From equation (2.3), it is clear $h\nu'$ is dependent on the scattered angle θ. When considering the limiting cases of $\theta = 0$ and $\theta = \pi$, it is seen that $h\nu'$ ranges from zero to $h\nu$. This indicates that the incident photon energy that is transferred to the electron can range from very little to almost all of it (since it would be impossible for the photon to impart all of its energy in a Compton scatter).

For incident gamma-ray energies ranging from 0.5 MeV to 10 MeV, Compton scattering becomes the main mode of interaction [19]. This energy range is typical when dealing with radioisotope sources, which makes Compton scattering of particular interest for this research.

2.3.3 Pair production

Although not particularly relevant for the context of this work, the pair production interaction is included for completeness.

Pair production is a process in which a gamma-ray interacts with the nucleus of an atom, which causes the photon to produce an electron-positron pair. This process is only energetically possible if the incident photon has an energy of at least 1.022 MeV (the rest-mass of an electron-positron pair). The produced positron will eventually thermalise in the absorbing material, and undergo annihilation with an electron. This subsequently produces two annihilation photons as secondary byproducts. This process is shown in Fig. 2.3.

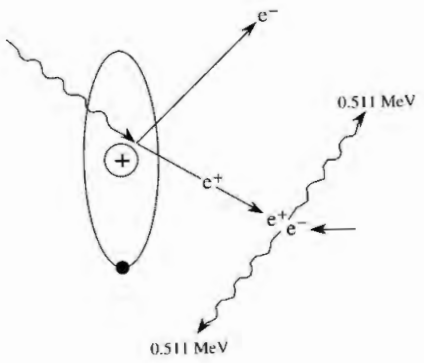

Fig. 2.3: Diagram of the pair production process. The incident photon (possessing an energy of at least 1.022 MeV) interacts in the Coulomb field of the atomic nucleus, which produces an electron-positron pair. The positron subsequently undergoes annihilation, which produces two 511 keV photons as secondary byproducts. This image was adapted from Martin & Wen [21].

If pair production occurs inside the detection material, then the kinetic energy of the e^+e^- pair will be measured, in addition to the secondary annihilation photons (provided they remain inside the detection material). If pair production occurs outside of the detection material (in the surrounding shielding, for example), then the kinetic energy of the e^+e^- pair will not be recorded. However, either of the secondary annihilation photons may still be detected, provided they travel through the detection material.

In the context of radiation detection, the presence of this interaction can be inferred by observing the energy spectrum. A single-escape peak corresponds to the detection of one of the annihilation photons, while the other escapes the detection material undetected. In contrast, a double-escape peak corresponds to when both annihilation photons escape the material undetected.

It should be noted that despite this interaction being possible for an incident photon energy of 1.022 MeV, it only becomes significantly probable at energies greater than 10 MeV [19].

2.4 Detection principles of scintillators

Scintillators refer to materials that produce prompt light when exposed to ionising photons. These photons transfer their kinetic energy to the scintillation material through the previously-discussed mechanisms of photoelectric absorption, Compton scattering and pair production, which causes electron excitation and ionisation. The subsequent de-excitation of these electrons causes the production of light.

Broadly, there are two different types of scintillators, namely organic and inorganic. Organic scintillators are typically used for the measurement of fast neutron and beta particles, while inorganic scintillators for gamma-ray measurements. Based on the relevance and context to this study, this section will focus on inorganic scintillators and its scintillation mechanism.

2.4.1 Energy band structure in inorganic crystal scintillators

The scintillation mechanism for crystal scintillators generally depends on the structure of the crystal lattice itself. In the case of inorganic scintillators, there are two types of crystal structures, namely pure crystal, and activated crystal.

In a pure crystal lattice, electrons are confined to certain energy bands. Fig. 2.4 shows this energy band structure defined by the upper (or conduction) band and lower (or valence) band. The valence band represents those electrons which are essentially bound to the crystal lattice, while the conduction band represents the electrons that possess the necessary energy to move throughout the crystal lattice medium. The region in between the conduction and valence bands is known as the energy band gap (or forbidden gap). This band gap is a region of the crystal lattice in which there are no energy states for the electrons to occupy.

When ionising photons travel through the crystal lattice of the scintillation material, their kinetic energy is transferred to the surrounding electrons through the mechanisms of photoelectric absorption, Compton scattering and pair production. After a sufficient amount of energy has been transferred, electrons in the valence band are able to elevate to the conduction band, which creates electron-hole pairs. If the electrons return to the holes created in the valence bands, this results in the emission of scintillation photons. As it turns out, this process is rather inefficient, because the absorption and emission spectra for pure crystals are seen to typically overlap, and so the emitted photons tend to be resonantly reabsorbed. As a result, very few photons are released per decay, and the photons that are emitted often possess too high an energy to be suitably detected.

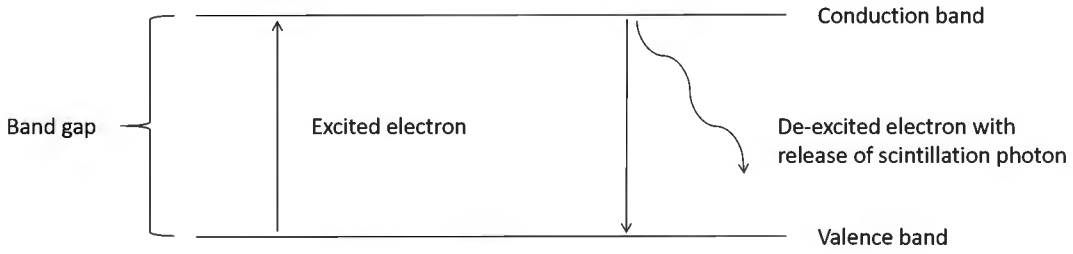

Fig. 2.4: Energy band structure of an inorganic pure crystal scintillator. The band gap is defined by the positioning of the conduction band (upper) and valence band (lower). In the presence of ionising photons, electrons can elevate from the valence band to the conduction band after energy absorption. The process of these excited electrons de-exciting back to the valence band causes the release of a scintillation photon.

In order to improve the probability that scintillation photons possessing suitable energies are emitted, small traces of impurities are typically added to inorganic scintillators. These impurities are known as activators. These activators create energy states at certain locations in the crystal that are within the band gap. Fig. 2.5 shows how the addition of activators modify the energy band structure of the crystal lattice. In contrast to the pure crystal structure, there are now special energy sites which are created in previously inaccessible regions (i.e. in the band gap). Electrons in the conduction band are now able to thermalise through the various energy states created by the activator, until it reaches a configuration which permits a transition to the ground state. The electrons will then de-excite to the ground state with a high probability of photon emission. It is also worth noting that these activator energy sites have the effect of increasing the wavelength of photon emissions such that the energy lies within the band gap. This results in lower energy photon emissions, and inhibits re-absorption.

2.4.2 Properties and structure of an inorganic cylindrical scintillator and the photomultiplier tube (PMT)

In practice, there are several favourable properties that are sought after in scintillators. While most of these characteristics apply for general scintillators, they are particularly relevant for

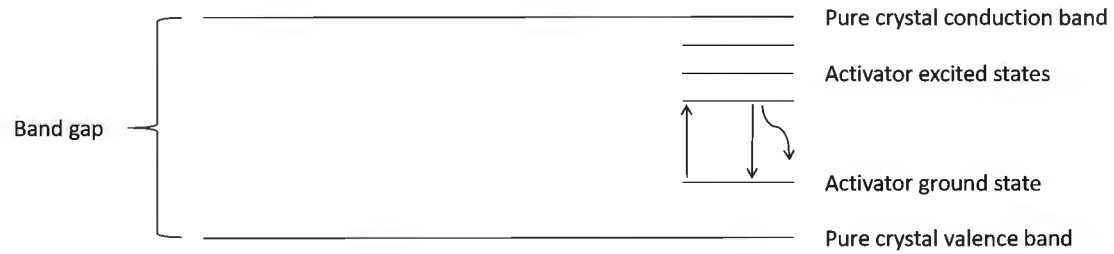

Fig. 2.5: Energy band structure of an inorganic activated crystalline scintillator. The activator introduced into the crystal scintillator creates energy states in between the established band gap of the pure crystal. Electrons may now excite and de-excite to these additional energy states.

the practical use of inorganic scintillators. Some of the most notable include [19]:

- the physical dimensions of the scintillator should be suitably large for practical measurements, as well as cost-effective to produce
- the ionising radiation should be converted to light output with a high scintillation efficiency
- the light yield should be proportional to the radiation over a wide dynamic range
- the emission wavelength and light yield should be appropriately matched to the photomultiplier tube (PMT)
- the induced luminescence should have fast rise and decay times, which is important for good timing resolution in time-of-flight measurements.

Derenzo *et al.* [24] provide a detailed discussion on some of these important characteristics for an ideal scintillator.

Fig. 2.6 shows a typical schematic of an inorganic cylindrical scintillator detector. The scintillator is seen coupled to a PMT, which serves the purpose of converting the extremely weak light output from scintillation pulses into corresponding electrical signals. Comprising the PMT, there is a photosensitive layer called the photocathode (or simply, cathode), which is coupled to an electron multiplier structure (the focusing electrode and dynodes). The cathode converts the scintillation pulses into low-energy electrons. These electrons are typically too few to constitute a practical electrical signal, which is why the electron multiplier structure serves as an efficient collector of these electrons while acting as an amplifier which greatly increases their number. This amplification process through the dynodes typically produces between $10^7 - 10^{10}$ electrons, which is sufficient to constitute an electrical signal. These electrons are collected at the anode of the PMT.

2.5 Gamma-ray spectrometry

Gamma-ray spectrometry refers to the quantitative study of the energy spectra produced from gamma radiation. This section provides a review of some of the key concepts and definitions involving gamma-ray spectrometry, which will prove relevant for this study. These include energy resolution, detection efficiency, dead time of the detector, peak pile-up effects, peak-to-total area and peak-to-Compton ratios.

2.5.1 Energy resolution

The intrinsic energy resolution (R) is a quantity that is used to quantify a detector system's ability to distinguish photons of different energies for spectroscopy measurements. A formal

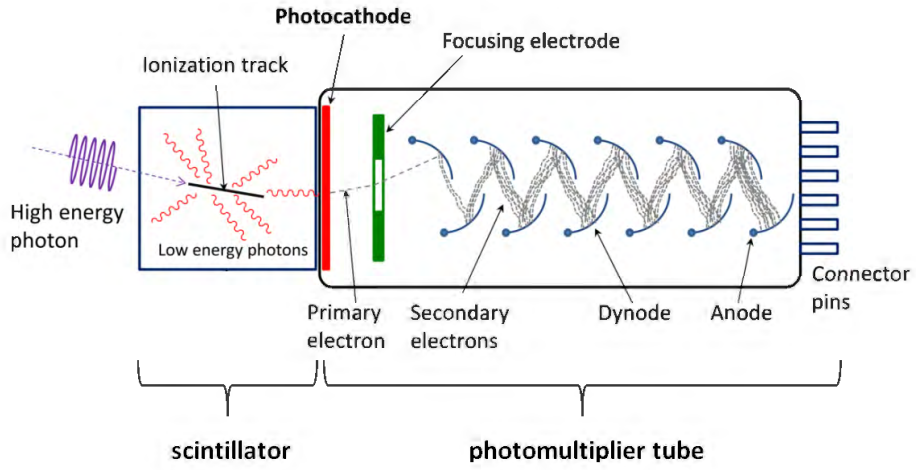

Fig. 2.6: Schematic of the typical structure of a cylindrical scintillator detector. The incident radiation interacts inside the scintillation material, which release low energy photons, which subsequently are converted to photoelectrons. These photoelectrons undergo a process of electron multiplication through the PMT, which then forms a suitable electric signal. This image was adapted from Wikimedia Commons [25], distributed under a CC BY-SA 3.0 license.

definition is shown with the aid of Fig. 2.7. It shows a typical mono-energetic photopeak recorded with a detector, which is fitted with a Gaussian function. This photopeak is defined by several quantities, including a photopeak amplitude $\mathcal{A}$ and a photopeak centroid E_γ. The energy distribution of the photopeak is described by the full-width-at-half-maximum (FWHM), which is defined as the width of the distribution at half of the photopeak amplitude ($\frac{\mathcal{A}}{2}$). This definition assumes that the background on which the photopeak is superimposed is negligible (or subtracted away). For a Gaussian peak, the FWHM can be related to the peak's standard deviation σ as FWHM $= 2.35\sigma$ [19]. The energy resolution is then defined by,

$$R = \frac{2.35\sigma}{E_\gamma}. \tag{2.4}$$

It should be noted that R is a dimensionless quantity and is functional with energy, so it is conventionally presented as a percentage at a specific energy. Also noteworthy is that lower energy resolutions are typically what are desired when using detector systems. Lower energy resolutions correspond to smaller energy distributions of the photopeak, and thus, better resolving power. Clearly then, an ideal energy resolution would be equivalent to zero i.e. the FWHM will become infinitesimally small such that the response function in Fig. 2.7 becomes equivalent to a Delta function. However, it is impossible for a detector to possess perfect energy resolution for several reasons. These include possible drift of the operating characteristics of the detector during measurement, random background noise from the detector and measurement instrumentation itself, and statistical noise that is an inherent part of measuring radioactive processes.

While the energy resolution cannot be identically zero, it certainly can be minimised to a certain extent. This is done through optimisation of the DSP parameter settings, which can have measurable effects on energy resolutions. This process is demonstrated in Section 3.3.

2.5.2 Detection efficiency

When detecting uncharged radiation (such as gamma-rays), it is often found that the detection efficiency of the detector is much less than 100%. This is due to the fact that uncharged

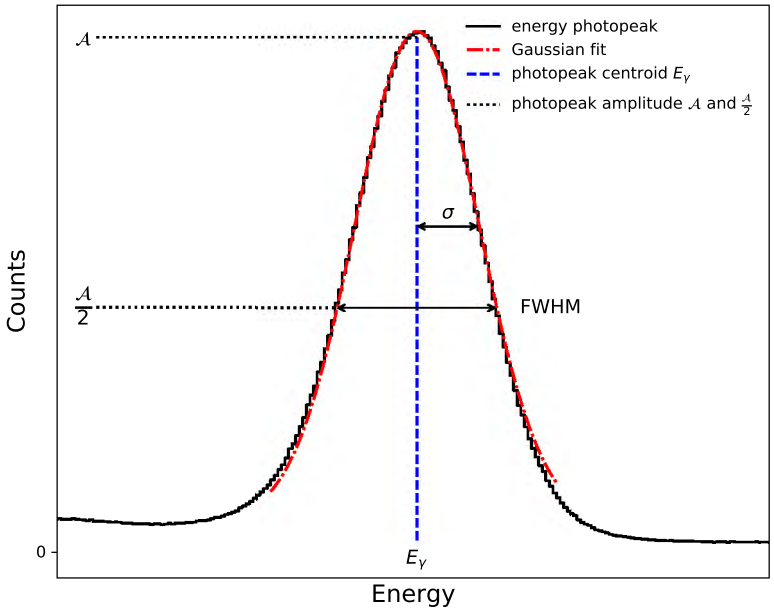

Fig. 2.7: A typical mono-energetic photopeak of amplitude $\mathcal{A}$ is centred around energy E_γ. The photopeak is modelled with a Gaussian fit. The distribution of the Gaussian peak is described through the FWHM and σ, which are both indicated.

radiation typically has a much lower cross section than that of charged radiation (such as α and β particles), which is because the uncharged radiation does not interact via the long range Coulomb force. This results in uncharged radiation having a low probability of interaction inside of a detector.

Knoll [19] notes the four main types of efficiencies, namely absolute efficiency (E_{abs}), intrinsic efficiency (E_{int}), full-energy peak (FEP) efficiency (E_{FEP}), and intrinsic FEP efficiency ($E_{FEP,int}$). These are respectively defined by the relations,

$$E_{abs} = \frac{\text{Number of pulses recorded}}{\text{Number of radiation quanta emitted by the source}}, \tag{2.5}$$

$$E_{int} = \frac{\text{Number of pulses recorded}}{\text{Number of radiation quanta incident on detector}}, \tag{2.6}$$

$$E_{FEP} = \frac{\text{Number of pulses recorded in single photopeak}}{\text{Number of radiation quanta emitted by the source at photopeak energy}}, \tag{2.7}$$

and,

$$E_{FEP,int} = \frac{\text{Number of pulses recorded in single photopeak}}{\text{Number of radiation quanta incident on detector at photopeak energy}}. \tag{2.8}$$

E_{abs} and E_{int} are related to each other using the equation [19],

$$E_{int} = E_{abs}\frac{4\pi}{\Omega}, \tag{2.9}$$

where Ω is the solid angle defined between the detector and radioactive source.

Intrinsic efficiencies tend to be of more practical use, because they depend primarily on factors such as the detector material and composition, the incident radiation energy, and the physical thickness of the detector. Although, Ogundare, Oniya & Balogun [26] have shown that there is also a slight distance dependence, or more specifically, a dependence on the ratio $\frac{d}{r}$, where d represents the source-to-detector distance and r represents the radius of the detector.

From practical gamma-ray spectroscopy measurements, equation (2.7) is calculated using [27],

$$E_{FEP}(E_\gamma) = \frac{N_p}{A_c \times t \times I_\gamma(E_\gamma)}, \tag{2.10}$$

where E_γ is the specific energy of the gamma-ray emitted from the radioactive source, N_p is the total number of counts in a photopeak due to gamma-rays of energy E_γ, A_c is the current activity of the radioactive source, t is the total time taken to perform the measurement and $I_\gamma(E_\gamma)$ is the gamma-ray intensity per decay at energy E_γ.

Similarly to (2.9),

$$E_{FEP,int} = E_{FEP}\frac{4\pi}{\Omega}. \tag{2.11}$$

For the remainder of this work, E_{FEP} (2.10) and $E_{FEP,int}$ (2.11) are the only efficiencies that will be considered (since they are the most commonly-used in literature).

2.5.3 Dead time of a detector system

The dead time of a detector system refers to the amount of time that the system is unable to record measurements due to the processing of incoming measurements of (usually) high count rates. Because of the random nature of the radioactive decay process, there is always some probability that events will go undetected due to them having occurred too soon after preceding events. These undetected events (or dead time losses) could potentially be significant, and therefore would need to be corrected for when performing any sort of counting measurements with particularly high count rates.

Typically when discussing dead time, there are two general models that are considered - namely paralyzable and nonparalyzable dead time. For the nonparalyzable dead time model, a detected event will cause the system to have a finite period of dead time (τ). As a consequence, any subsequent events which occur during that period τ will be go undetected. Once the time τ has elapsed, the system will then be able to detect the next incoming event (upon which would commence another dead time period). This interaction can be modelled using the equation [19],

$$n = \frac{m}{1 - m\tau}, \tag{2.12}$$

where n represents the true interaction rate of the steady-state radioactive source being measured, and m represents the measured count rate. Both n and m are assumed to be averaged over a sufficiently long period of time.

For the case of paralyzable dead time, each subsequent detection of an event within a dead time period τ extends the length of that period by τ. As a result, any event that occurs during that extended period of dead time will also be lost. Theoretically, this model predicts that a sufficiently high count rate could extend the dead time indefinitely. For a detector system with paralyzable dead time to remain functional, there has to be a sufficient 'cooling off' period in which there are no incoming events for a minimum period of τ. Paralyzable dead time can be modelled using [19],

$$m = n\exp^{-n\tau}. \tag{2.13}$$

It should be noted that in the case of low count rates ($n << \frac{1}{\tau}$), equations (2.12) and (2.13) become identical (as expected). This implies that lower count rates tend to minimise the dead time of the detector system.

2.5.4 Peak-to-total (PTR) and peak-to-Compton (PTC) ratios

The peak-to-total ratio (PTR) is a quantity that relates the net counts of an energy photopeak (C_p) to the total counts of the spectrum (C_s). It provides a useful measure of the relative amount of detected gamma-rays which have undergone photoelectric absorption. The relationship is given by [28, 29],

$$\text{PTR} = \frac{C_p}{C_s}. \tag{2.14}$$

Another useful quantity is the peak-to-Compton ratio (PCR). This is defined as the ratio between the height of the photopeak (H_p) and the average height of the Compton continuum (H_c). This provides a comparison between the relative number of gamma-rays which have undergone photoelectric absorption to the gamma-rays which have undergone Compton scattering. So, the relationship is given by [29, 30],

$$\text{PCR} = \frac{H_p}{H_c}. \tag{2.15}$$

Both PTR and PCR are both useful quantities which help evaluate the performance of a spectrometer.

2.6 $LaBr_3$:Ce detector

The $LaBr_3$:Ce detector is an example of a detector which uses an inorganic scintillator. These detectors are typically associated with performing measurements with excellent energy resolutions, fast emission and possessing high count rate capabilities [31–34]. The detectors used in this work were manufactured by Saint-Gobain, and each consists of a 2×2" $LaBr_3$:Ce scintillation crystal lattice which is attached to a Hamamatsu R2083 PMT. This section will detail the key differences between the types of signals recorded by this type of detector during the measurement process.

2.6.1 Energy and timing signals

There are two signals which are generated by the detectors used in this work, namely the *slow* energy and *fast* timing signals. The slow signal arises from the positive pulses generated at the eighth dynode of the PMT [35, 36]. These dynode pulses are firstly pre-amplified, and then subsequently amplified to produce the energy signals. The fast signal arises from the negative pulses generated at the anode of the PMT [35, 36]. The anode pulses from two different detectors are fed into the Constant Fraction Discriminator (CFD), which generates two negative output pulses. These CFD pulses are sent to the time-to-amplitude converter (TAC), where one of the CFD pulses is used as a start signal to TAC, while the other is used as the stop signal. The TAC is then able to provide amplitude pulses whose height corresponds to the time difference between the start and the stop signals. Both the TAC amplitude signals and post-amplification energy signals are processed through the analogue-to-digital converter (ADC), which digitizes the signals.

Fig. 2.8 shows a typical (a) slow, and (b) fast signal trace measured using a $LaBr_3$:Ce detector. There are a couple of key differences which can be identified. Firstly, it is seen that the signals are processed with opposite polarities i.e. the slow and fast signal traces correspond to a positive and negative amplitude, respectively. Another key feature is the rate at which each signal trace dissipates. It is seen that when the slow signal is detected, the signal decays

gradually over several microseconds. However, when the fast signal is detected, it decays at a much higher rate compared to the slow signal.

By assuming an exponential signal decay given as $\sim e^{-t/\tau}$ (where τ is the decay constant), it is shown in Section 3.3 that the slow signal corresponds to $\tau \sim 30$ μs, while the fast signal corresponds to $\tau \sim 10$ ns. This shows that the fast signal is better suited to perform timing measurements, since it processes the measurement information at a higher rate than the slow signal.

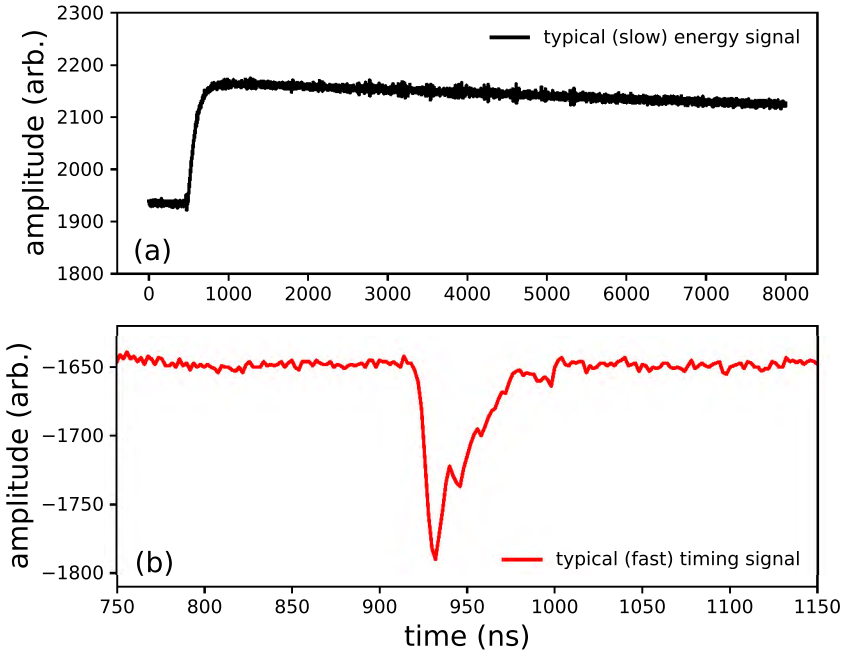

Fig. 2.8: Typical traces for (a) slow, and (b) fast signals. The slow signal is characterised by a slow signal decay ($\tau \sim 30$ μs), while the fast signal by a quicker decay ($\tau \sim 10$ ns).

Fig. 2.9 shows the typical energy spectra measured from both the slow and fast signals using a 9 μCi ^{22}Na source. The source was placed at a distance of 6 cm coaxially from the face of one of the 2×2" $LaBr_3$:Ce detectors used for this investigation (see Section 3.1 for detector specifications), and operated with a high voltage of -1100 V. The prominent 511 keV and 1275 keV peaks are evident in both spectra. Comparing the σ values for the 511 keV peaks, it is seen that the slow signal produces a better energy resolution with $\sigma = 10.3$ (16) keV, while the fast signal produces $\sigma = 22.6$ (24) keV. This demonstrates that the slow signal is better suited to perform energy measurements with a higher degree of precision, while the fast signal is better suited to perform timing measurements.

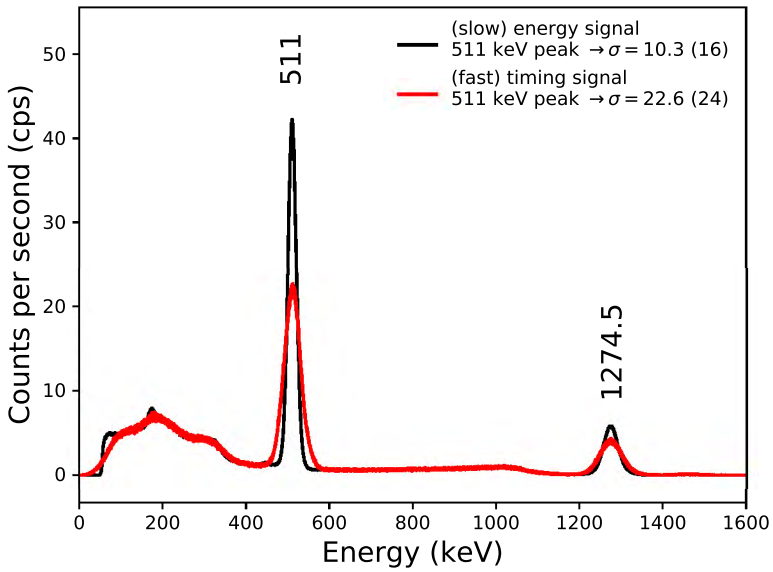

Fig. 2.9: Energy spectra measured from the slow (black), and fast (red) signals. A 9 μCi ^{22}Na source was used for measurement, and the prominent 511 keV and 1275 keV energy peaks are indicated. The 511 keV peak of the slow signal was determined to have better energy resolution with $\sigma = 10.3\ (16)$ keV, while the 511 keV peak of the fast signal has $\sigma = 22.6\ (24)$ keV.

3 Experimental methods and set-up

This section details the set-up of the detector system in terms of geometry, electronics and data acquisition settings that were used for these measurements. Summaries of the methods used in this work for energy resolution minimisation, calibration (energy and timing), data reduction, and background subtraction are also included.

All experimental measurements presented in this work were performed at the iThemba Laboratory for Accelerator Based Sciences (LABS), Cape Town, South Africa. All experimental equipment and facilities required to perform this investigation were provided by iThemba LABS, and in addition, all ^{22}Na sources used in these measurements were manufactured and provided by iThemba LABS[1].

Details of all relevant runs in the measurement series, measurement dates and activity strengths of the ^{22}Na source used for each measurement are provided in Table 3.1.

[1]iThemba LABS is the sole producer of ^{22}Na radioactive sources in the world!

Table 3.1: List of all measurements that were performed. Each measurement was performed in the AFRODITE vault at iThemba LABS using a ^{22}Na source placed at the centre of an array of eight $LaBr_3$:Ce detectors (see Fig. 3.1).

Measurement series run number	**Start date**	**Stop date**	**Measurement period (seconds)**	**Activity of source (μCi)**	**Events recorded ($\times 10^9$)**	**Notes**
R01	11/09/2020	15/09/2020	355091	7.3 (11)	7.07757 (8)	
R02	24/09/2020	25/09/2020	69990	124 (19)	38.3967 (2)	
R03	29/09/2020	1/10/2020	187312	124 (19)	29.3669 (2)	Trigger threshold of slow signal increased to maximum input (10000) in order to improve measurement stability
R04	1/10/2020	14/10/2020	1189215	124 (19)	172.6599 (4)	Slow signal trigger threshold maintained at input of 10000
R05	23/10/2020	6/11/2020	1154911	124 (19)	180.1260 (4)	Slow signal trigger threshold maintained at input of 10000

3.1 Detector assembly

Prior to performing the main measurements presented in this work, various detector system geometries were considered to determine the ideal set-up for the detector assembly. A detailed discussion is provided in Section 4.

Measurements of the gamma radiation emitted from ^{22}Na radioactive sources of various activities were performed with the multi-gamma-ray spectrometer. The spectrometer (see Fig. 3.1) consisted of an array of eight $LaBr_3$:Ce (5%) detectors (labelled as D1-D8), which were arranged in a planar geometry. These detectors were manufactured by Saint-Gobain, and each consists of a 2×2" $LaBr_3$:Ce scintillation crystal lattice which is attached to a Hamamatsu R2083 PMT. A ^{22}Na source was placed symmetrically at the centre of the detector array, such that it was an equidistant 12 cm from the face of each detector. The source was placed on a plastic stand, which ensured that it was situated in the same plane as the centre of each detector. Based on the cylindrical geometry of each detector, and the equidistant source-to-detector distance, the solid angle subtended between the source and each detector was determined to be 1.0838 (1)% of 4π steradians. Due to the symmetry of the set-up and isotropic nature of the source, the accumulative solid angle for the eight-detector system is 8.671 (3)% of 4π steradians.

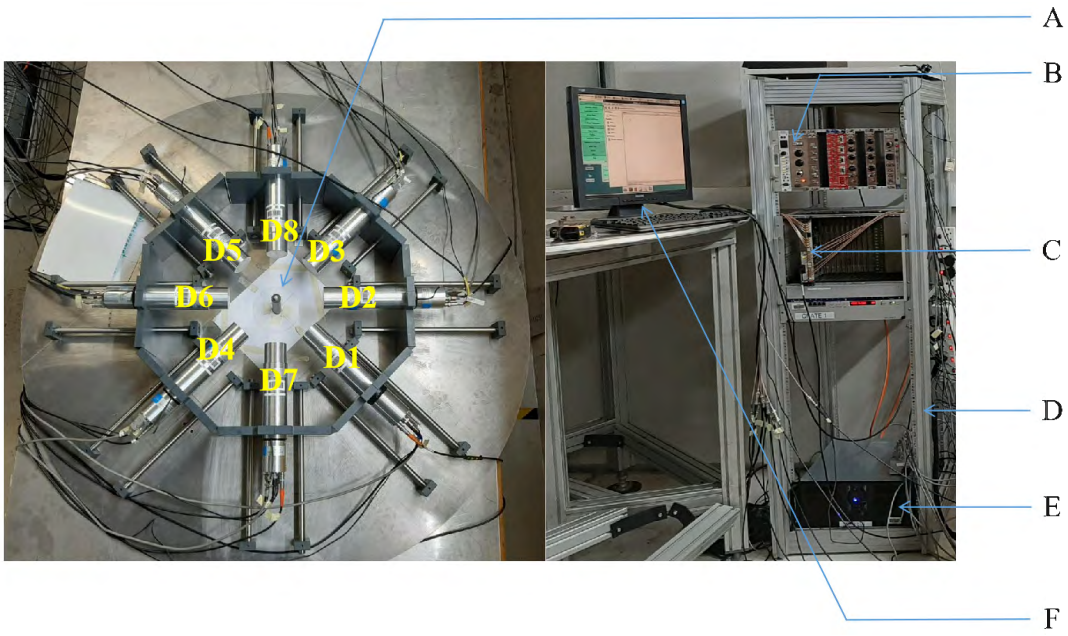

Fig. 3.1: The detector system consists of eight $LaBr_3$:Ce detectors (D1-D8), which are situated in a planar geometry. The ^{22}Na source is placed on a plastic stand such that the source lies in the same plane as the centre of each detector. The source is placed equidistantly in the centre of the array of detectors with a source-to-detector distance of 12 cm. The associated electronics of the detector system are also shown. (A = ^{22}Na source on plastic stand, B = High voltage supply, C = Pixie-16, D = Crate and NIM bin, E = CPU and F = PC display).

3.2 Electronics and data acquisition system

Fig. 3.2 shows a schematic of how each $LaBr_3$:Ce detector was connected to the relevant electronics. As seen in Fig. 3.1, the electronics (including the high voltage (HV) supply, the XIA Pixie-16 module and the CPU) were all housed in a crate and NIM bin. Each detector was powered by an HV power supply, and each of the photomultiplier tube (PMT) anodes were integrated with a model 474 ORTEC pre-amplifier to provide the signals. Table 3.2 shows a list of

the operating voltage and the voltage supply model used for each of the detectors (D1-D8). The operating HV settings were selected in order to gain-match the energy spectra recorded from each detector i.e. ensuring the various energy peaks from each energy spectra corresponded to similar channel numbers. The data was then re-binned post-acquisition through energy calibration (see Section 3.4).

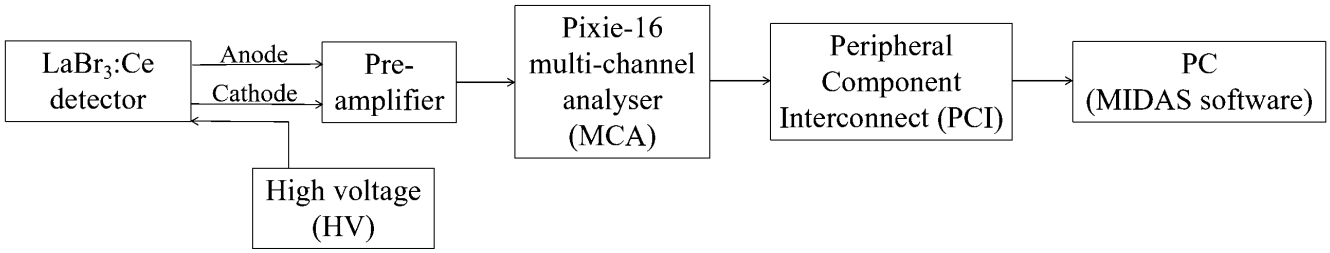

Fig. 3.2: Each $LaBr_3$:Ce detector is powered by an HV power supply. The signals from the PMT's eighth dynode (slow) and anode (fast) are processed through the pre-amplifier, and the output signals are then digitised and processed through at 500 MHz using a 16-channel digital Pixie signal processor. The digitised data is then transmitted to the PCI bridge, from which the MIDAS software is able to access the data.

Table 3.2: Detectors D1-D6 were operated using a CAEN S.p.A. NHS 62 20n power supply, while detectors D7 and D8 were operated using an ORTEC 456. The HV settings were selected such that the energy spectra produced from each detector were 'gain-matched'.

Detector	**HV power supply model**	**Operating HV setting (V)**
D1	CAEN S.p.A. NHS 62 20n	−1100
D2	CAEN S.p.A. NHS 62 20n	−1130
D3	CAEN S.p.A. NHS 62 20n	−1100
D4	CAEN S.p.A. NHS 62 20n	−1250
D5	CAEN S.p.A. NHS 62 20n	−1150
D6	CAEN S.p.A. NHS 62 20n	−1200
D7	ORTEC 456	−1100
D8	ORTEC 456	−1100

The generation and characteristics of the signals generated at the eighth dynode (*slow signal*) and anode (*fast signal*) of the PMT were discussed in Section 2.6.1. These slow and fast signals were transmitted to the XIA Pixie-16 module using RG58 cables and RG175/lemo connectors, respectively. The XIA Pixie-16 module is a 16-channel digital signal processor which samples the data at 500 MHz [37]. Each of the 16 channels of the Pixie-16 module can be operated independently for data acquisition. Each channel is gated using a Channel Gate Input which ranges from 0-15. Each of the slow signals of detectors D1-D8 respectively, were connected to channels 0-7. Each of the fast signals of detectors D1-D8 respectively, were connected to channels 8-15. Table 3.3 shows the DSP parameter settings for both the slow and fast signals, and their respective channels. These settings for both the slow and fast signals produced from each detector were selected such that the measured energy resolutions were minimised to $\sim 5\%$ and $\sim 10\%$ at 511 keV, respectively.

The software used for the data acquisition was the Multi Instance Data Acquisition System (or MIDAS) [38, 39]. MIDAS was able to access all of the recorded data from the hardware electronics through a single Peripheral Component Interconnect (PCI) bridge (PXI-8360). The data was recorded in list-mode and written to network storage for offline analyses. The mea-

Table 3.3: DSP parameter settings for both the eighth dynode (slow) and anode (fast) signals. The slow signals for each detector D1-D8 were connected to channels 0-7, respectively, of the Pixie-16 module, while the fast signals were connected to channels 8-15, respectively.

Parameter/ Action	**Slow signal (Channel Gate Inputs 0-7)**	**Fast signal (Channel Gate Inputs 8-15)**
Trigger type	Local	Local
Good channel	Enable	Enable
Trigger polarity	Positive	Negative
Histogram energies	Enable	Disable
CFD trigger mode	Enable	Enable
Global trigger validation	Disable	Disable
Energy sums	Enable	Enable
Channel trigger validation	Enable	Enable
Input relay	Enable	Enable
Pileup rejection	Disable	Disable
Trigger threshold	1000	350
Fast rise time (μs)	0.1	0.02
Fast flat top (μs)	0.1	0.01
Energy rise time (μs)	0.3	0.1
Energy flat top (μs)	1.3	0.1
Peak sample (μs)	1.52	0.12
Peak separation (μs)	1.0	1.0
Decay constant (μs)	36.39	0.01
CFD delay	0.01	0.01
CFD scale	1	1
CFD threshold	50	50

surement had an accumulative run time of 5.16×10^6 s, which is comparable to the run times of similar experiments performed by Yang *et al.* (2.02×10^7 s [11]) and Vetter & Freedman ($9.45\ (1) \times 10^5$ s [12]). There were approximately 4.85×10^{11} total events ($\sim$ 12.5 TB of data) recorded at an average acquisition rate of 2.4 MB/s.

List-mode data structure

Recording measurements through the use of list-mode allows for data collection on an event-by-event basis, recording energies, timestamps, pulse shape analysis values, and waveforms. A detailed breakdown of the list-mode data structure is provided in the XIA Pixie-16 user's manual [37]. This has been summarised below with the aid of Fig. 3.3, which illustrates the data structure of an event n recorded in list-mode.

As demonstrated in Fig. 3.3, the data of the output buffer is organized into three sections. This includes one buffer header, an event header for each event, and a channel header which is accompanied by possible waveform data for each active channel included in the event. All of the header information is comprised of 32-bit data words, while the waveform data consists of two samples of 16-bit trace data combined into one 32-bit word. The buffer header consists of 6 words, which includes stored information on the number of words in the buffer, module number, run type, and start time of the run. Following from the buffer header, each event is then recorded in sequence of its detected arrival time. The event header is comprised of 3 words, which contain information about the hit pattern (i.e. which channels were read out for each event) and the arrival time for each event. Following from this is the channel header,

which organises and records the data from each channel for a particular event. It consists of 9 words, which contain information about the number of 32-bit words for that particular channel, the fast trigger time, energy, and pulse shape analysis values. Each channel header would be followed by any waveform data which was recorded for that particular channel. Each 32-bit word in the waveform data consists of two samples of 16-bit trace data.

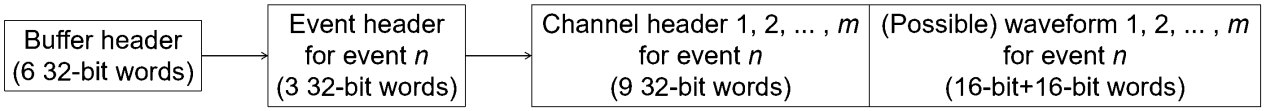

Fig. 3.3: List mode data structure for a recorded event n. In this illustration, it is assumed that event n provided data to m channels, as indicated.

3.3 Minimisation of energy resolutions

Since this investigation concerns the measurement of a rare branching ratio of Ps, this suggests that high count rates and good energy resolutions are required for suitable measurements to be performed. This section presents the methods used in determining the optimised DSP parameter settings that produced minimum energy resolutions for both the slow and fast signals. The results of this section have been presented in Table 3.3. The parameters that are considered include the decay constant, the pulse shape filtering and charge-to-digital converter (QDC) settings.

3.3.1 Slow signal

The slow signal is characterised by a longer decay constant $\tau \sim 30$ μs. Fig. 3.4 shows a typical slow signal trace over 8000 ns that is detected using a ^{22}Na source. The trace is characterised by an exponential decay, a constant offset that is greater than zero and a signal amplitude $\mathcal{A}$ (each of which is indicated).

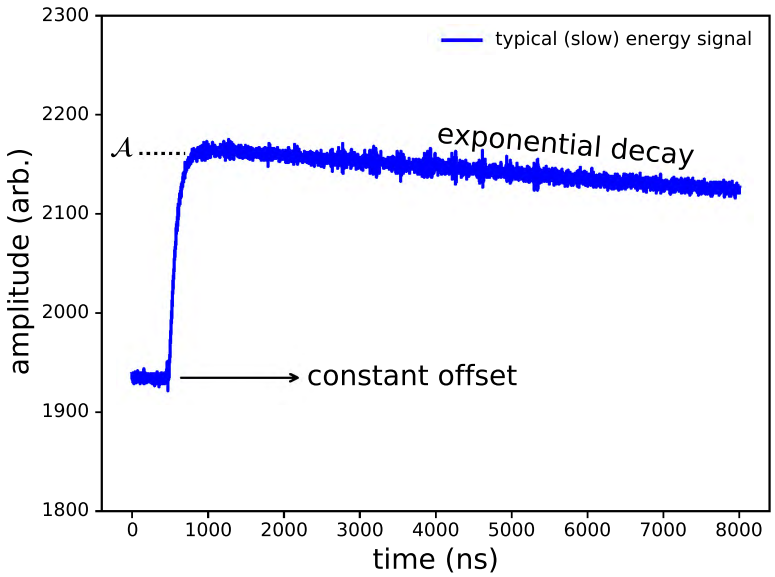

Fig. 3.4: A typical slow signal trace collected over 8000 ns. The trace is characterised by a (slow) exponential decay, signal amplitude $\mathcal{A}$, and a positive constant offset.

3.3.1.1 Decay constant τ

Over 95 000 traces were collected over the range 8000 ns. These traces have an exponential decay $\sim e^{-t/\tau}$, where τ is the decay constant. Fitting an exponential to each of these traces, a τ value can be obtained.

Fig. 3.5 shows the process of fitting the exponential $\mathcal{A}e^{-t/\tau}$, where $\mathcal{A}$ and τ are the fit parameters for the amplitude and decay constant, respectively. The first step of the process is shown in Fig. 3.5 (a), where the signal trace is recorded from the detector. Fig. 3.5 (b) shows the fit of a constant function to the base of the trace to determine the value of the constant offset. This value is subtracted from the trace in Fig. 3.5 (a) to produce the trace in Fig. 3.5 (c). Fitting the exponential to the trace in Fig. 3.5 (c) produces values for $\mathcal{A}$ and τ.

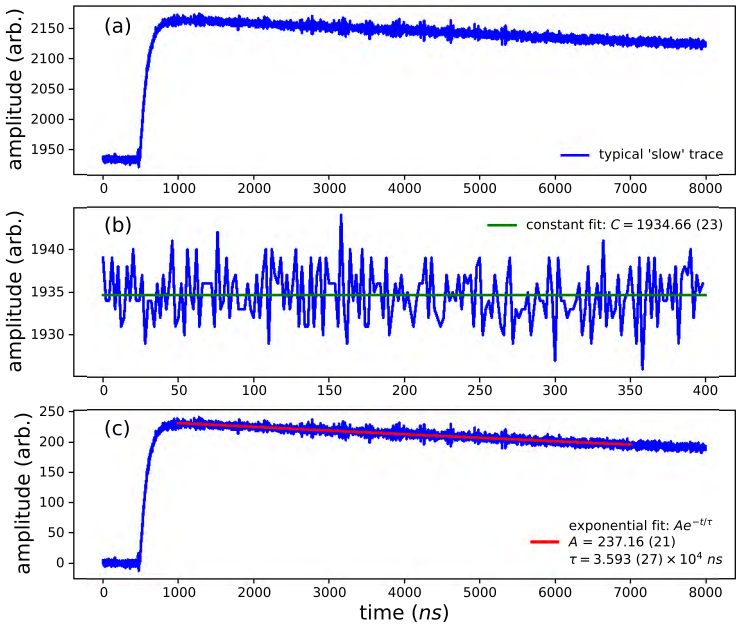

Fig. 3.5: Each step of the fitting process to determine the decay constant τ for the slow signal. (a) shows a typical slow trace, (b) shows the fit of a constant function to determine the value of the constant offset and (c) shows the exponential fit to the trace after subtraction of the constant offset.

The fitting process in Fig. 3.5 was done for each one of the recorded 95 000 traces, which produced as many τ values. Binning these τ values into intervals of 10 ns, Fig. 3.6 is produced. By taking note of the most frequently occurring τ value for the slow signal (τ_s), this provides the τ setting that will produce a minimum energy resolution. From Fig. 3.6, τ_s is found to be,

$$\tau_s = 36.385\ (29)\ \mu s. \tag{3.1}$$

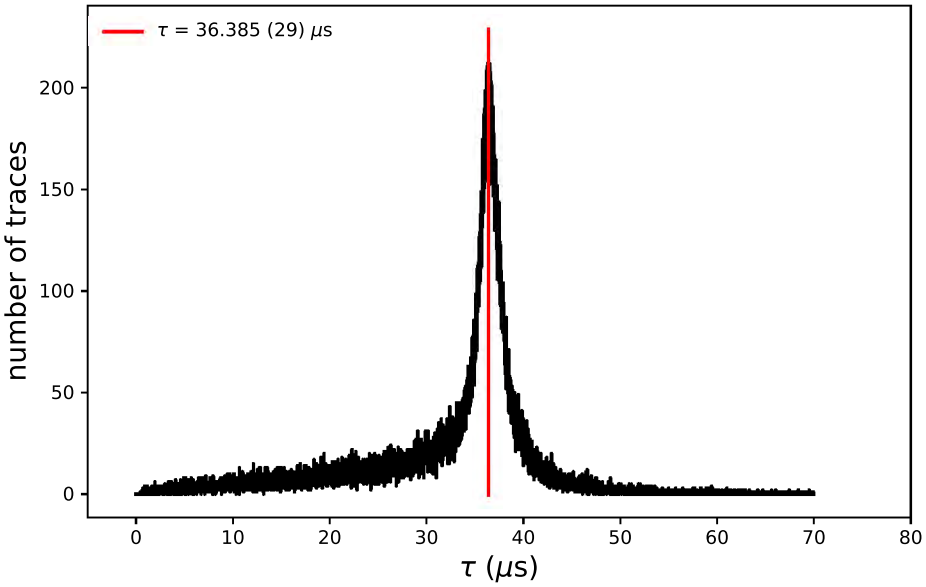

Fig. 3.6: The decay constant τ binned into an interval of 10 ns using over 95 000 slow trace signals. The most frequently occurring τ value was found to be 36.385 (29) μs, which corresponds to a minimum energy resolution.

3.3.1.2 Energy filter rise time and flat top

Both the slow and fast signals that get detected from the $LaBr_3$:Ce detectors undergo trapezoidal filtering. Therefore, the output signal that is produced after filtering is in the shape of a trapezoid, with a characteristic energy filtering rise time (L) and flat top (G). These values are typically set in the data acquisition software (MIDAS, in this case) before measurement begins. Fig. 3.7 shows the slow signal before and after a trapezoidal filtering.

It turns out that the settings of L and G have a measurable effect on the energy resolution of the gamma-ray peaks. It is therefore possible to determine the settings for L and G that produce a minimum energy resolution. For this section, measurements will focus on the minimisation of the resolution of the 1332.5 keV peak of the ^{60}Co energy spectra.

Fig. 3.8 shows the energy resolution of the 1332.5 keV photopeak of a ^{60}Co source as a function of L and G. It is seen that a minimal resolution of 2.917 (31)% is produced by setting the rise time L = 0.3 μs and flat top G = 1.3 μs.

3.3.2 Fast signal

The fast signal is characterised by a shorter decay constant $\tau \sim 10$ ns, which is about 1000 times smaller than the τ value for the slow signal. Fig. 3.9 shows a typical fast signal trace that is detected from a ^{22}Na source. Similar to the slow signal, the fast trace is also characterised by an exponential decay, albeit much shorter. It also exhibits the parameters of a (negative) constant offset and a signal amplitude $\mathcal{A}$ (each of which is indicated in Fig. 3.9).

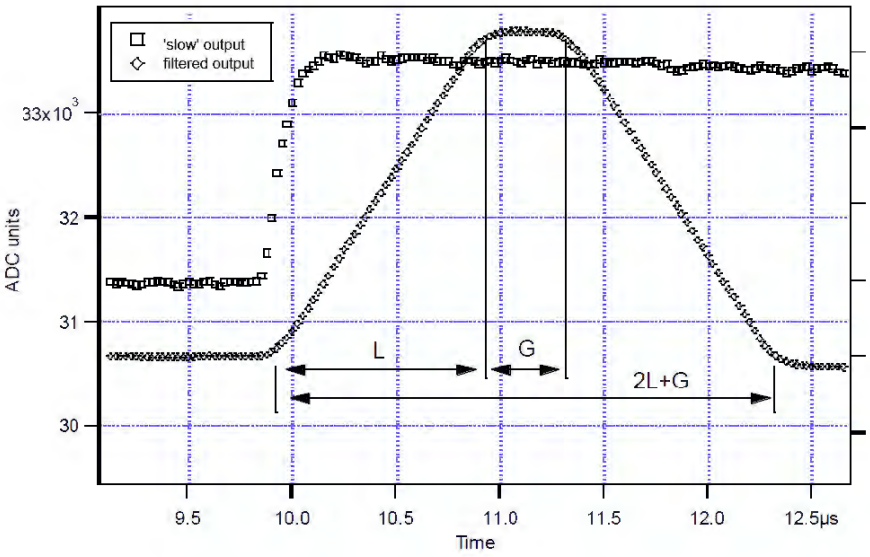

Fig. 3.7: The slow signal plotted with its filtered output from a trapezoidal filtering. The energy filtering rise time (L) and flat top (G) are indicated. This image was adapted from the XIA Pixie-16 user's manual [37].

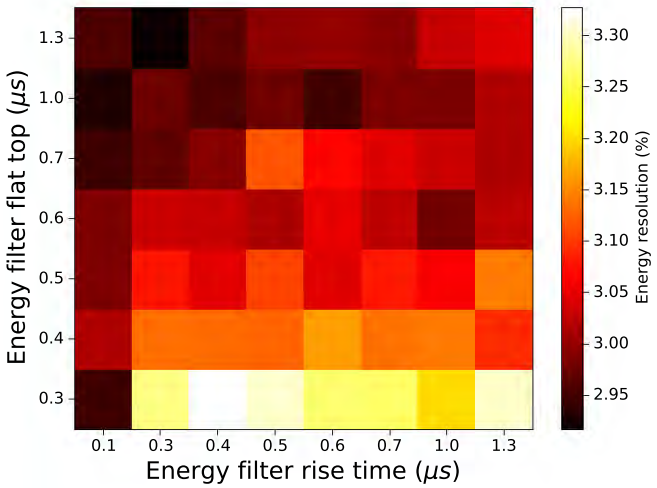

Fig. 3.8: Energy filter rise time and flat top settings along with their corresponding energy resolutions for the slow signal. The minimised energy resolution for the 1332.5 keV photopeak of a ^{60}Co source is found with a rise time of 0.3 μs and flat top of 1.3 μs.

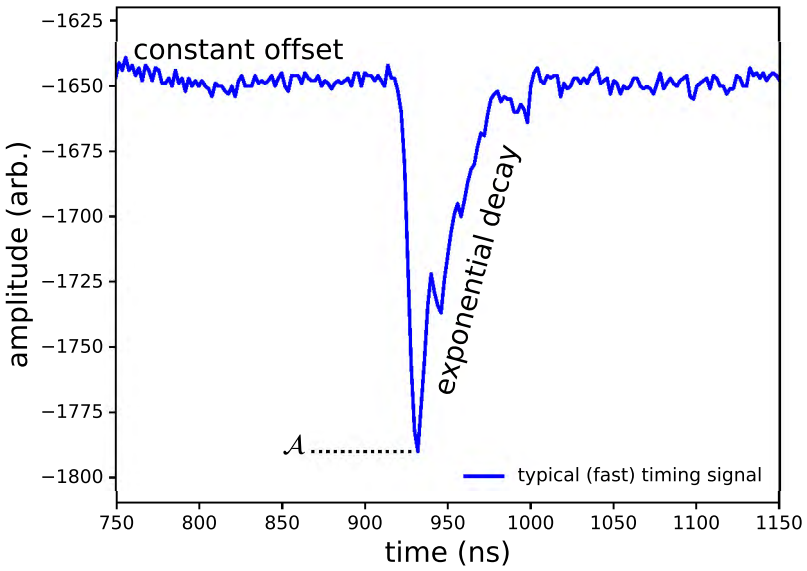

Fig. 3.9: A typical fast signal trace which is characterised by a (fast) exponential decay, signal amplitude $\mathcal{A}$, and a negative constant offset.

3.3.2.1 Decay constant τ

An important difference to note between the fast and the slow signals is that the fast signal is negative in polarity. So before an exponential can be fitted to the trace as before, it must first be inverted. The first step is shown in Fig. 3.10 (a), where the fast trace is recorded from the detector. A constant function is then fitted to the constant portion of the trace (Fig. 3.10 (b)), which determines a value for the constant offset. This value is subtracted from the trace, and then the resulting signal is inverted to produce the trace seen in Fig. 3.10 (c). The exponential is then fitted to the trace, which determined values for $\mathcal{A}$ and τ.

As with the slow signal, each of the obtained τ values are binned as shown in Fig. 3.11. The interval of these bins is set to 1 ns. The most frequently occurring τ value for the fast signal (τ_f) is found to be,

$$\tau_f = 10.5\ (29)\ ns. \tag{3.2}$$

3.3.2.2 Energy filter rise time and flat top

As mentioned in the previous section, both the slow and fast signals undergo trapezoidal filtering, and therefore the energy filter rise time (L) and flat top (G) that produces minimum energy resolutions can be determined. The measurements in this section focuses on the minimisation of the resolution of the 511 keV peak of the ^{22}Na energy spectra.

Fig. 3.12 shows the energy resolution of the 511 keV peak as a function of L and G. It is seen that a minimal resolution of 10.9 (11)% is produced when both L and G are set to 0.1 μs.

3.3.3 Charge-to-digital converter (QDC)

The charge-to-digital converter (or QDC) is a method of integration that integrates the fast signal over time to determine the total charge produced in the detector from incident radiation.

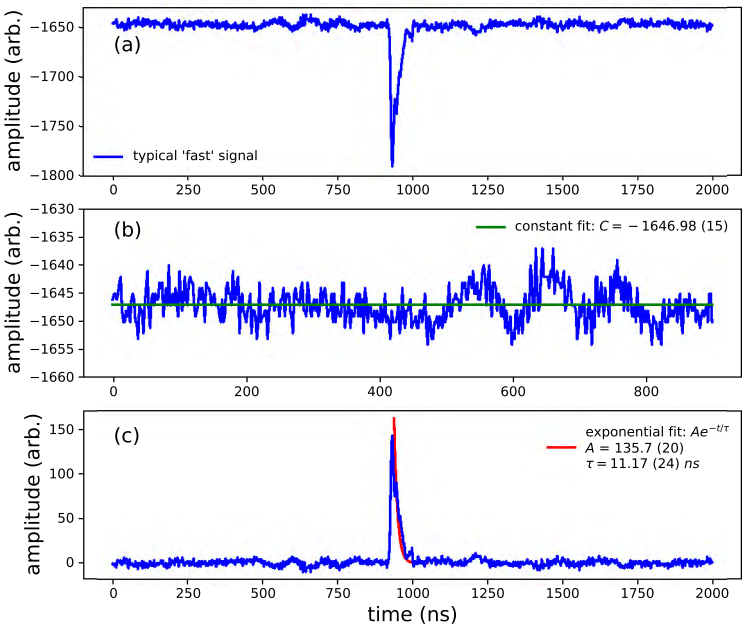

Fig. 3.10: Each step of the fitting process to determine the decay constant τ for the fast signal. (a) shows a typical fast trace, (b) shows the fit of a constant function to determine the value of the constant offset and (c) shows the exponential fit to the trace after subtraction of the constant offset and then inversion of the signal.

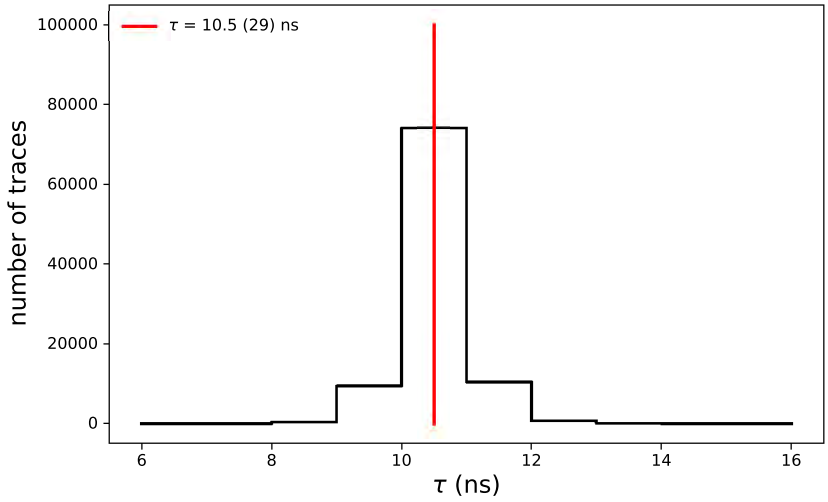

Fig. 3.11: The decay constant τ binned into an interval of 1 ns using over 95 000 fast trace signals. The most frequently occurring τ value was found to be 10.5 (29) ns, which corresponds to a minimum energy resolution.

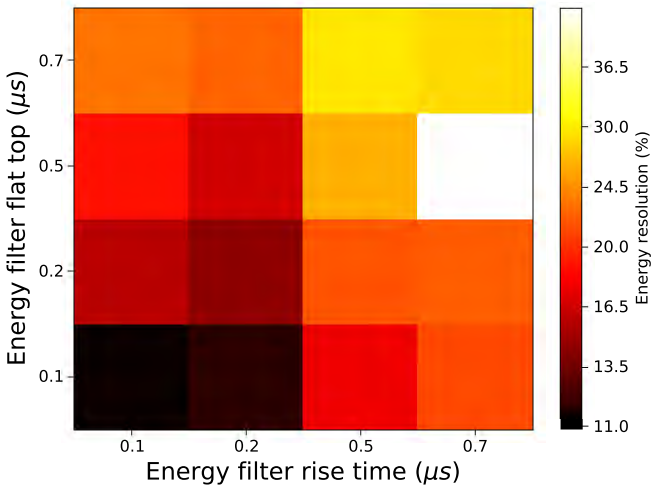

Fig. 3.12: Energy filter rise time and flat top settings along with their corresponding energy resolutions for the fast signal. The minimised energy resolution of the 511 keV peak of a ^{22}Na source is found with a rise time and flat top both set to 0.1 μs.

In order for this integration to be performed, limits for the integration (or a gate) must be provided. This is done by the user before the measurement is performed. Fig. 3.13 illustrates the various gate lengths that were used to integrate the fast signal.

It turns out that the selection of the gate has an effect on the resolution measured for the energy spectra of the ^{22}Na source. This is shown in Table 3.4, where various gate length settings were selected.

It is clear from Table 3.4 that longer gate lengths have an adverse effect on the energy resolution that is measured. This is due to the fact that longer gate lengths incorporate more signal noise into the integration, which manifests itself by producing energy spectra with poorer resolution. However, by making the gate lengths less than 100 ns, it is then found that the whole signal amplitude is not incorporated into the integration, which results in information being lost.

The ideal gate length setting is then empirically determined to be 100 ns, which produces a minimum energy resolution of 12.4 (13)%.

Table 3.4: Various gate length settings with their corresponding energy resolution measurements of the 511 keV peak of ^{22}Na. Increasing gate lengths produce progressively worse resolutions.

Gate length (ns)	**Energy resolution of 511 keV peak (%)**
100	12.4 (13)
150	12.9 (18)
200	13.3 (18)
250	14.6 (21)
300	15.2 (33)

3.3.4 Energy spectra of ^{22}Na using the optimised slow, fast and QDC signals

The last few sections (Section 3.3.1, Section 3.3.2 and Section 3.3.3) have demonstrated the methods used to obtain minimum energy resolutions for the slow, fast and QDC signals, re-

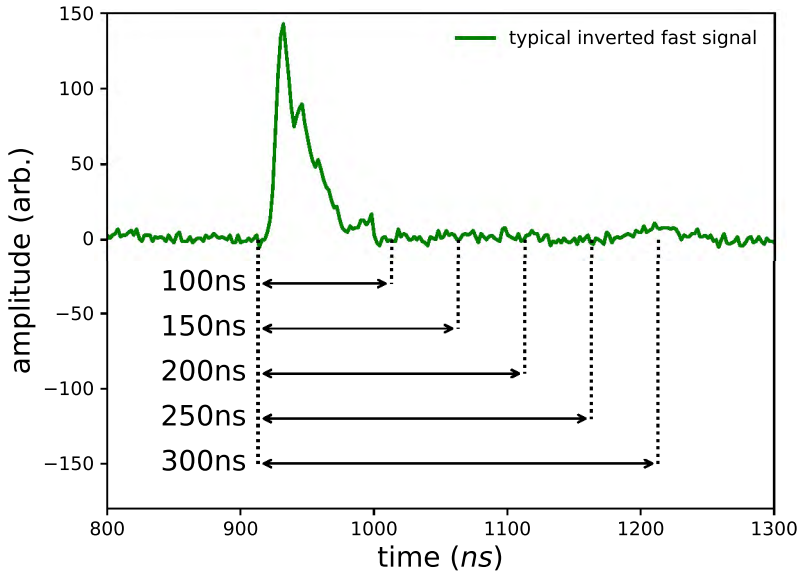

Fig. 3.13: A typical fast signal trace with various integration intervals (or gates). The total charge produced from a particular signal is determined by the integration of the pulse over the gate. The length of the gates have a measurable effect on the resolutions in the energy spectra, which is shown in Table 3.4.

spectively. Table 3.5 provides a summary of the key results obtained in those sections. These 'optimised' settings were used as input settings for the main measurement of this work (shown in Table 3.3).

Table 3.5: The values for the DSP settings (namely, decay constants, pulse shape parameters and gate length) that correspond to minimum energy resolutions for the slow, fast and QDC signals.

Signal	**Decay constant τ (μs)**	**Energy rise time (μs)**	**Energy flat top (μs)**	**Gate length (ns)**
slow	36.39	0.3	1.3	–
fast	0.01	0.1	0.1	–
QDC	–	–	–	100

In order to compare the respective minimised energy resolutions from each of these signals, Fig. 3.14 shows the energy spectra measured from these slow, fast and QDC signals. Fig. 3.14 is resultant from the same measurement that produced Fig. 2.9 (see Section 2.6.1), with the primary difference being the inclusion of the energy spectrum from the QDC signal. As before, the σ values for the 511 keV peaks are shown, and it is seen that the energy resolution of the slow signal ($\sigma = 10.3$ (16) keV) is significantly superior to both those of the fast signal ($\sigma = 22.6$ (24) keV) and QDC signal ($\sigma = 21.3$ (27) keV).

3.4 Energy calibration

Before conducting the measurements for this work, each of the eight $LaBr_3$:Ce detectors (D1-D8) were energy calibrated. Energy calibration is a process which involves measuring various radioactive sources with known gamma-ray emission energies, and correlating each of those energy photopeaks to a particular channel in the spectrum. The energy peaks of ^{152}Eu (121.8, 244.7, 344.3, 778.9, 964.1, 1408.0) keV were used to calibrate each energy spectrum. All analysis and

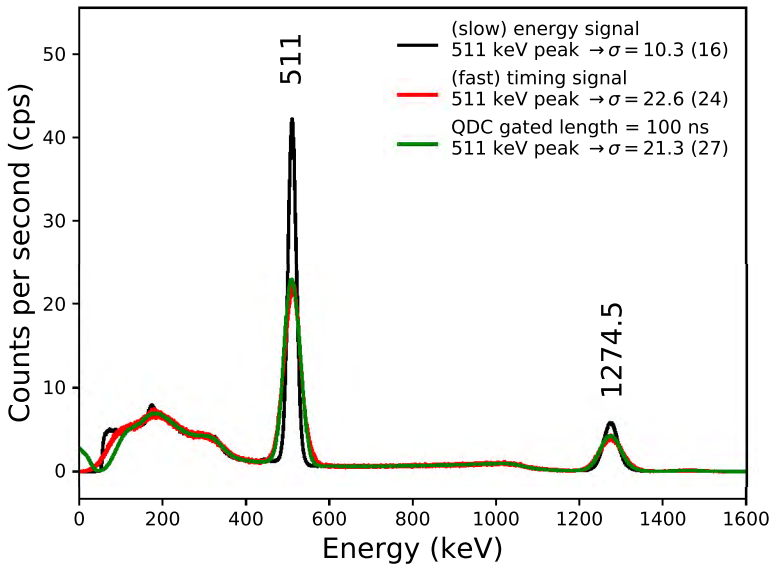

Fig. 3.14: Energy spectra measured from the slow (black), fast (red) and QDC (green) signals which correspond to minimum energy resolutions. A ^{22}Na radioactive source with an activity of 9 μCi was used, with the prominent 511 keV and 1275 keV energy peaks indicated. The 511 keV peak of the slow signal was determined to have the best energy resolution with $\sigma = 10.3$ (16) keV, while the 511 keV peak of the fast and QDC signals were found to be $\sigma = 22.6$ (24) keV and $\sigma = 21.3$ (27) keV, respectively.

energy calibration of spectra in this section are produced from the fast signal. This is because the final measurements of this work are performed using the fast signal (due to its favourable timing characteristics as previously discussed). The slow signal, while providing better energy information, is not of any particular interest when performing timing measurements, and its calibration is therefore neglected.

Below is summarised each step of the energy calibration process that was performed for a particular spectrum:

- Each of the energy photopeaks in the spectrum was fitted with a Gaussian function in order to obtain a channel mean (centroid) for each peak. The fitting was done using Python software (version Python 3.7.3), in particular, the Gaussian fit model available in the LMFIT package [40]. This process is demonstrated in Fig. 3.15 using the 344 keV photopeak of the ^{152}Eu source as an example.

- The known gamma-ray emission energies of each peak was plotted against the corresponding channel mean values (centroids) that were obtained from the Gaussian fittings.

- The function formed between the energy peaks and channel centroids is typically observed to be linear or quadratic [23]. For this work, a quadratic function was fitted to the data to obtain the energy calibration fit parameters. This fitting was done using ROOT software (version ROOT 6.14/06) [41], with the process demonstrated in Fig. 3.16. A discussion on why quadratic functions were used for these fittings is provided in the following section.

- These steps were repeated for each of detector D1-D8, which produced fit parameters for the energy calibration of each detector.

To illustrate the importance of energy calibration, Fig. 3.17 shows the energy spectra of ^{152}Eu measured using detectors D1-D4 (a) before energy calibration, and (b) after energy calibration. It is clear that energy calibration is effective in lining up each of the peaks to their respective energy values (or 'gain-matching'). This is particularly useful when comparing and analysing the data from different detectors.

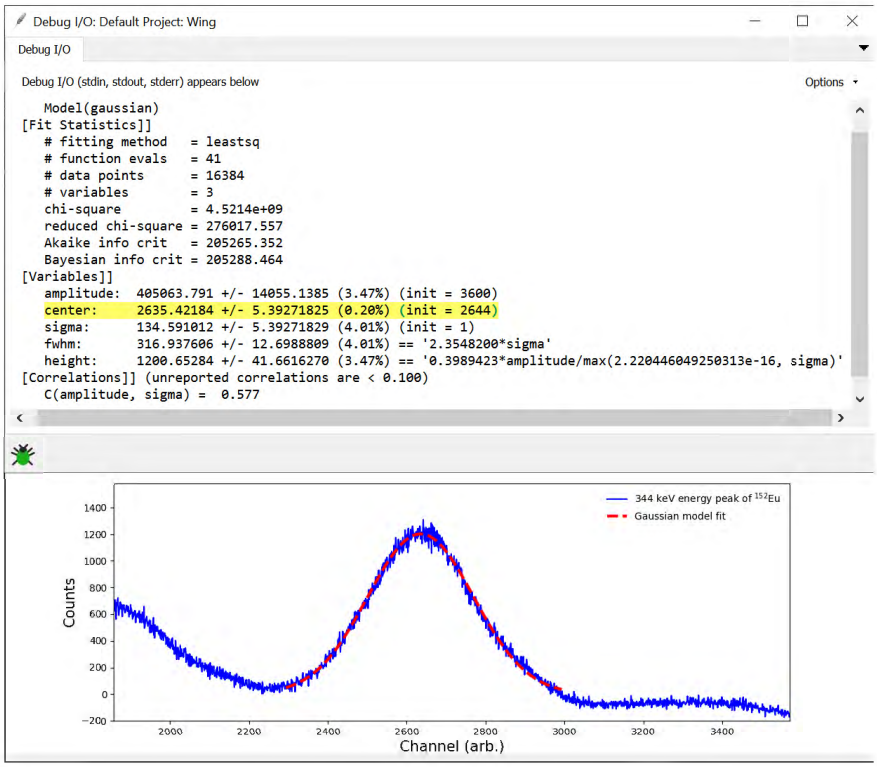

Fig. 3.15: Example of a Gaussian fit using Python software to determine the channel mean (i.e. the centroid of the Gaussian). The energy peak is of the 344 keV gamma-ray emission of ^{152}Eu. The upper panel shows the parameter details of the resulting fit (with the centroid highlighted). The lower panel shows the resulting Gaussian fit over the 344 keV peak.

The energy calibration fit parameters for the fast signal of each of the detectors (D1-D8) are tabulated in Table 3.6. It is noted that the contribution from the quadratic terms of each fit is of order $\sim 10^{-8}$, and that the uncertainties range from 50% to over 100%. It was found that the inclusion of these quadratic terms in each fit resulted in a significant improvement in terms of the fit quality. This is discussed in further detail in the following section. Also presented in the table are the χ^2 and confidence interval parameters, which provide an indication of the quality of fit for each set of fit parameters. These confidence intervals were calculated using the *TMath::Prob* function in ROOT [42].

The fit parameters presented in Table 3.6 are given for a general quadratic function,

$$E(x) = ax^2 + bx + c, \tag{3.3}$$

where E and x represent the energy and channel centroids, respectively, and a, b and c represent the parameters of the fit.

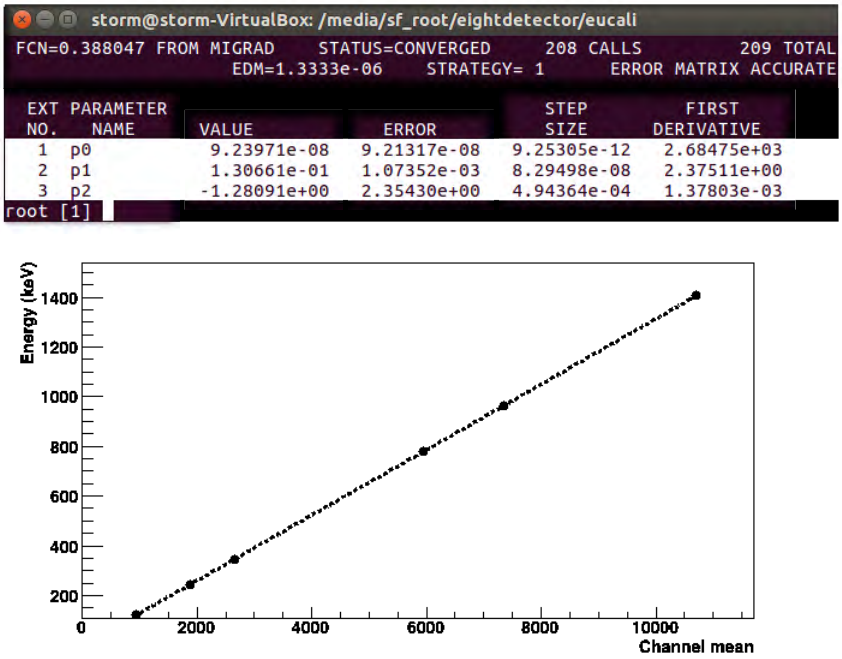

Fig. 3.16: Example of a quadratic function fit over the energy-centroid data using ROOT software. The data is taken using detector D1, with the upper panel displaying the fit parameters (p0, p1 and p2) for the energy calibration, and the lower panel displaying the resulting quadratic function fit to the data.

Table 3.6: Fit parameters for the energy calibration of the fast signal of each detector (D1-D8). These parameters are given for a general quadratic function defined as equation (3.3). Calibrations were performed using the known gamma-ray emission energies of a ^{152}Eu source. Also shown are the χ^2 and confidence intervals, which demonstrates the quality of each of the corresponding fits.

	Fit parameters for energy calibration			**Quality of fit**	
Detector	a $(\times 10^{-8})$	b $(\times 10^{-1})$	c	χ^2	**Confidence interval (%)**
D1	9.2 ± 9.2	1.307 ± 0.011	-1.3 ± 2.4	0.39	94.27
D2	5.2 ± 8.3	1.267 ± 0.010	-5.2 ± 2.3	0.41	93.72
D3	21.1 ± 9.8	1.321 ± 0.011	1.7 ± 2.4	0.27	96.65
D4	7.0 ± 4.3	1.0080 ± 0.0064	-0.2 ± 1.8	0.041	99.78
D5	12.0 ± 8.9	1.289 ± 0.011	-1.3 ± 2.3	0.015	99.95
D6	12.9 ± 5.8	1.1135 ± 0.0079	0.4 ± 2.0	0.16	98.44
D7	11.7 ± 6.6	1.1608 ± 0.0086	0.8 ± 2.1	0.053	99.68
D8	15 ± 10	1.358 ± 0.012	-0.02 ± 2.4	0.12	98.99

Fitting with linear and quadratic functions

As mentioned previously, the function formed between the energy peaks and channel centroids is usually linear or quadratic. So, a linear or quadratic function can then be fitted to the data to obtain the fit parameters for energy calibration. As an example, Fig. 3.18 shows the energy calibration for detector D1 using polynomials of the first (linear) and second degree (quadratic) for the fitting process. Also shown are the residuals for each fit. The residual standard deviations of the linear and quadratic fits were found to be 1.04 keV and 0.53 keV, respectively. These values suggest that the quadratic fit provides the better energy calibration, since the calibrated energy values are closer to their known energy values.

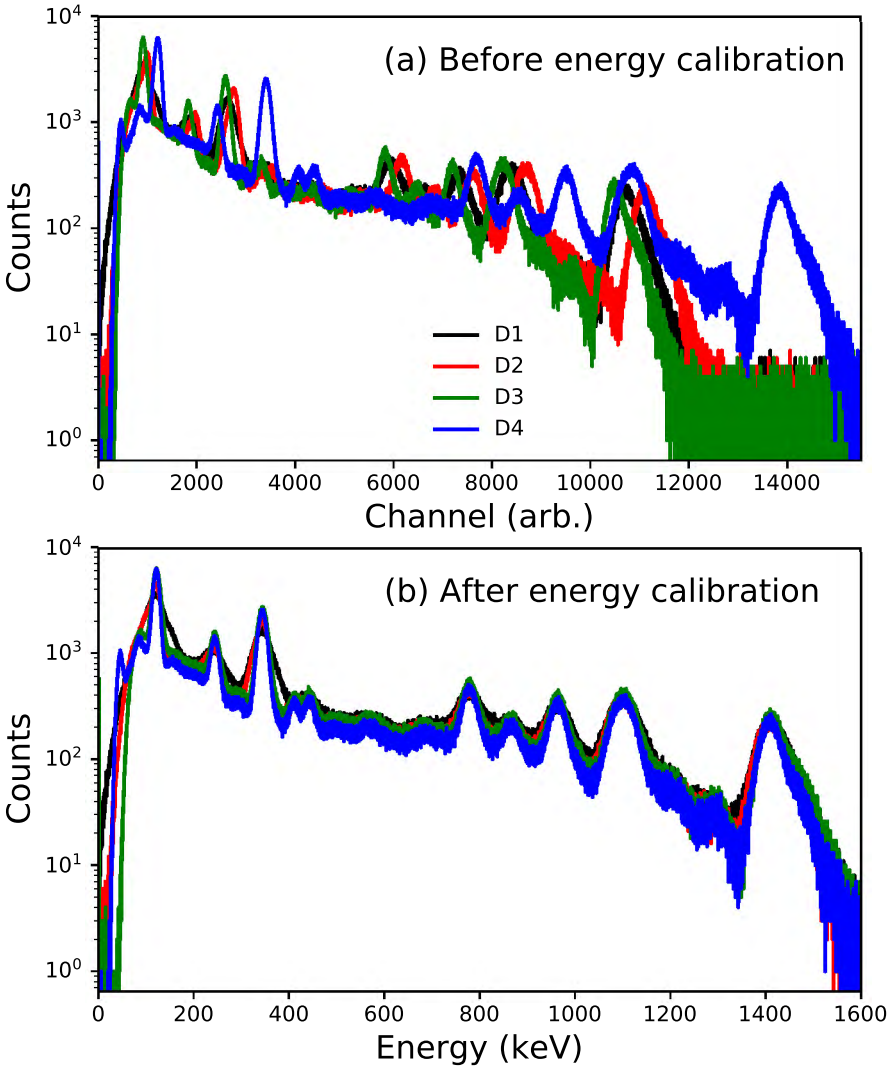

Fig. 3.17: Energy spectra of ^{152}Eu plus background radiation measured using detectors D1-D4. (a) shows the spectra before energy calibration, while (b) shows them after energy calibration.

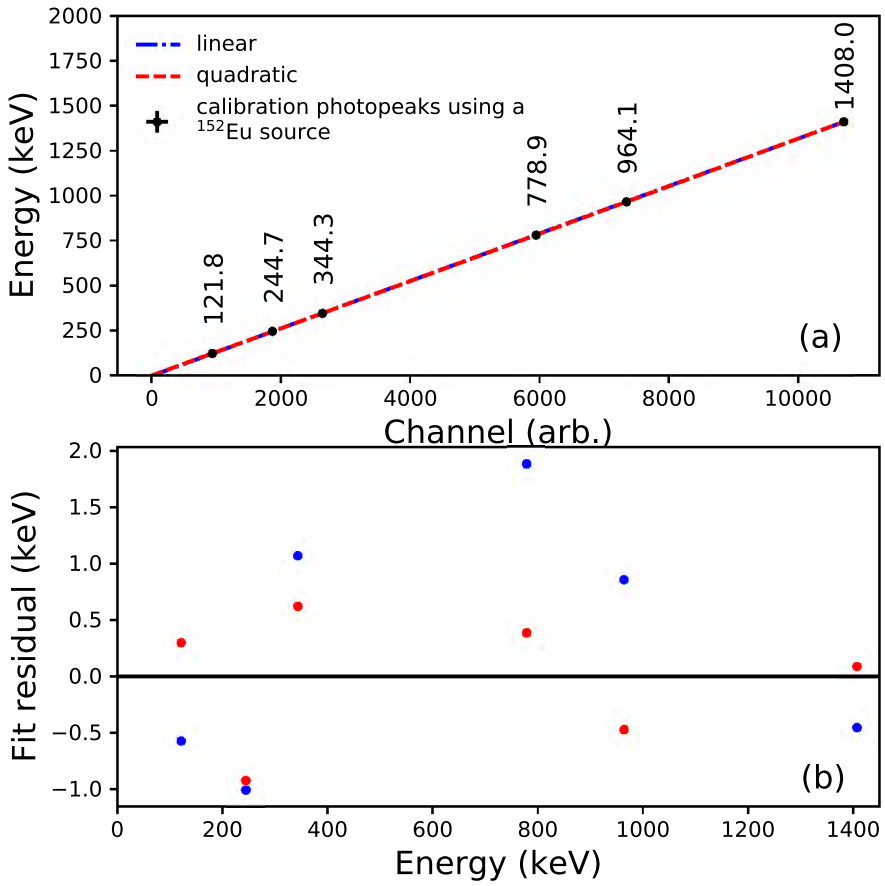

Fig. 3.18: (a) shows the energy calibration curve of detector D1 using the photopeaks of ^{152}Eu (121.8, 244.7, 344.3, 778.9, 964.1, 1408.0) keV for calibration (which are indicated). The data has been fitted using both linear (blue) and quadratic (red) functions. (b) shows the fit residuals of the linear and quadratic fits plotted against the energies of the calibration photopeaks. The residual standard deviations of the linear and quadratic fits were found to be 1.04 keV and 0.53 keV, respectively.

To further illustrate the point, Table 3.7 compares the quality fit parameters (including χ^2, degrees of freedom and confidence intervals) of the linear and quadratic fits for each detector (D1-D8). The poor confidence intervals shown for the linear fit (particularly for detectors D3, D4, D6, and D7) suggest that a linear fit is unsuitable for the energy calibrations required for this work. In contrast, the quadratic fit clearly provides a significant improvement to in terms of the confidence intervals of the fit parameters (an improvement of up to 70%). For these reasons, quadratic fits were used to perform energy calibrations.

Table 3.7: The quality fit parameters of χ^2, degrees of freedom and confidence intervals of each detector (D1-D8) are shown for linear and quadratic fits to the data. The linear fit has 4 degrees of freedom, since the fit considers 6 calibration energy photopeaks with 2 fit parameters (6-2=4), while the quadratic fit has 3 degrees of freedom using the similar reasoning.

Detector	**Type of fit**	**Degrees of freedom**	χ^2	**Confidence interval (%)**
D1	Linear	4	1.4	84.49
	Quadratic	3	0.39	94.27
D2	Linear	4	0.82	93.59
	Quadratic	3	0.41	93.72
D3	Linear	4	4.9	29.51
	Quadratic	3	0.27	96.65
D4	Linear	4	2.8	59.41
	Quadratic	3	0.041	99.78
D5	Linear	4	1.8	76.70
	Quadratic	3	0.015	99.95
D6	Linear	4	5.1	27.85
	Quadratic	3	0.16	98.44
D7	Linear	4	3.3	51.51
	Quadratic	3	0.053	99.68
D8	Linear	4	2.2	69.53
	Quadratic	3	0.12	98.99

3.5 Time difference spectra and timing calibration

As previously discussed, the measured data was recorded in list-mode (i.e. each measured gamma-ray event was assigned a corresponding time-stamp). This timing information was used to produce time difference spectra. These spectra are generated by determining the time differences between the gamma-ray events in any pair of $LaBr_3$:Ce detectors. For instance, if an event is recorded in detector D1 at a time of 3 ns, while another event is recorded in detector D2 at 5 ns, the time difference between these two events will be recorded as 2 ns. This becomes particularly useful for determining whether gamma-ray events have been detected in coincidence.

The spectra were calibrated by adding or subtracting (as necessary) from each time difference peak centroid such that each centroid would align to some constant offset. Fig. 3.19 shows the time difference spectra for each detector pair that is situated at 180° relative to each other, both before and after calibration. For this case, the constant offset of the peak centroids was chosen to be 0 ns.

3.6 Data reduction

Due to the large amount of data acquired during the measurement process, a filtering method was a necessary implementation. The object of the data reduction is to identify the events

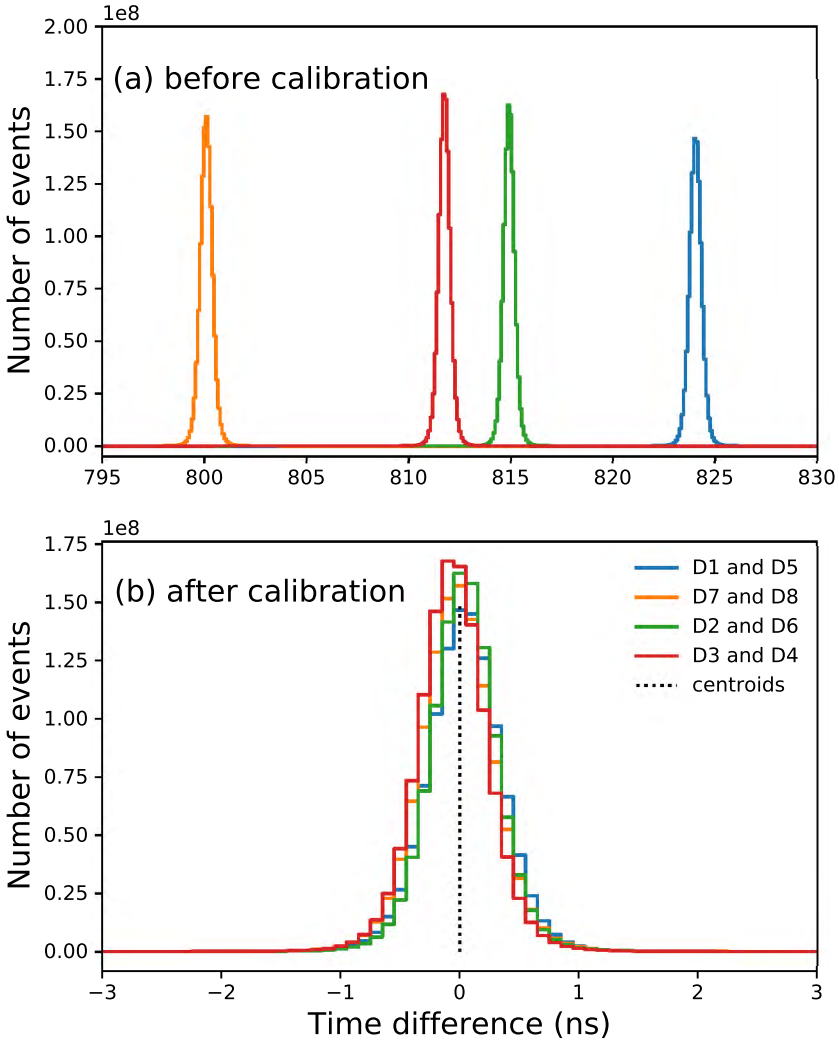

Fig. 3.19: Time differences between detectors D1 and D5 (blue), D2 and D6 (green), D3 and D4 (red), D7 and D8 (orange). Each of these pair of detectors are situated at 180° relative to each other. These time differences are shown (a) before, and (b) after calibration.

corresponding to both two- and four-photon decays, and separate each from the background events (i.e. the rest of the data). The sorting code for the data defines the energy (E_c) and time (T_c) windows that were used to filter between various detected interactions. These windows act as logical filters which allow for the data to be categorised with specific energy and timing requirements defined by their respective windows. Specifically, the two filtering conditions that all potential Ps annihilation events must pass include:

- the sum energy of the detected photons in the event must sum to 1022 keV (so that events correspond to the real mass of the annihilating e^+e^- pair). The sum energy window E_c is set such that $|\sum_{i=1}^{n} E_i - 1022 \text{ keV}| < E_c = 80$ keV.
- the detected photons must be detected in coincidence within a time window $T_c = 2$ ns i.e. the arrival times of each photon must occur within 2 ns.

Given that the full-width-at-half-maximum of the energy and time distributions vary for each detector in the detector array, the width values for E_c and T_c were selected such that the number of accepted 4γ events are maximised, while minimising background events from accidental interactions. These widths correspond to approximately 7σ of their respective peaks with a confidence level limit greater than 99%.

Fig. 3.20 illustrates the defined range of E_c and T_c relative to their typical peaks. It is seen that the entirety of each respective peak has been encapsulated within their respective window, while also ensuring that most unwanted background events were neglected over the ranges.

3.7 Background subtraction of energy spectra

For any measurement conducted with a radioactive source, the resulting energy spectra will show the accumulative radiation from both the source and the inherent background. In order to ensure that the measured spectra is solely due to the radiation of the source, there are several different methods of background subtraction which can be implemented. This section details and demonstrates the method of background subtraction implemented for this work using the energy spectra produced from ^{22}Na and ^{152}Eu samples. Some of the key features of each spectrum are also discussed.

3.7.1 Energy spectrum of ^{22}Na

Fig. 3.21 shows the calibrated energy spectrum of ^{22}Na before and after a background subtraction. The background subtraction involves a channel-by-channel subtraction of the counts per second produced by the background from the counts per second produced by the source. This method of background subtraction is only valid under the assumptions that both the radiation from the source and background radiation remain constant over their respective measurement periods. Practical considerations such as voltage drift is assumed to be negligible over these relatively short measurement periods. The prominent peaks of 511 keV and 1275 keV are indicated, and they are due to the various decays detailed in Fig. 1.2. The well-known 1460 keV peak is due to the background radiation of the ^{40}K decay. It is seen that the background subtraction effectively eliminates this peak from the spectrum.

3.7.2 Energy spectrum of ^{152}Eu

Fig. 3.22 shows the calibrated energy spectrum of ^{152}Eu before and after background subtraction. The same method of background subtraction was used as previously discussed. There are several peaks that are indicated due to the gamma emissions of ^{152}Eu. Interestingly there are

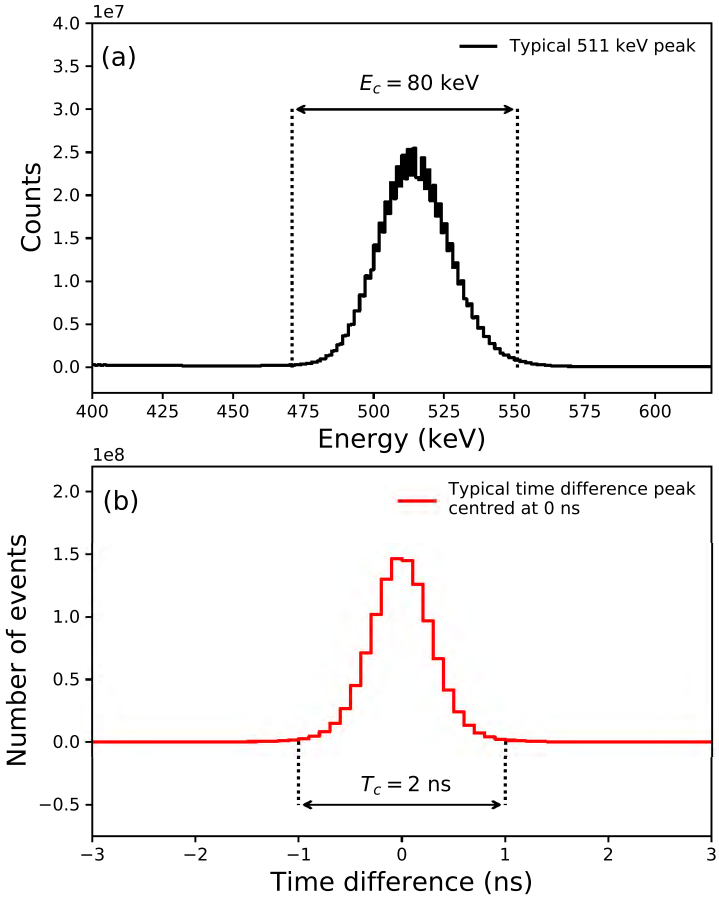

Fig. 3.20: (a) shows the energy window defined over the range 471-551 keV, while (b) shows the time window defined over 2 ns. A typical 511 keV peak (black) and time difference peak (red) are shown to be fully encapsulated by the chosen ranges. The time difference spectrum was calibrated such that its peak centroid was centred at 0 ns.

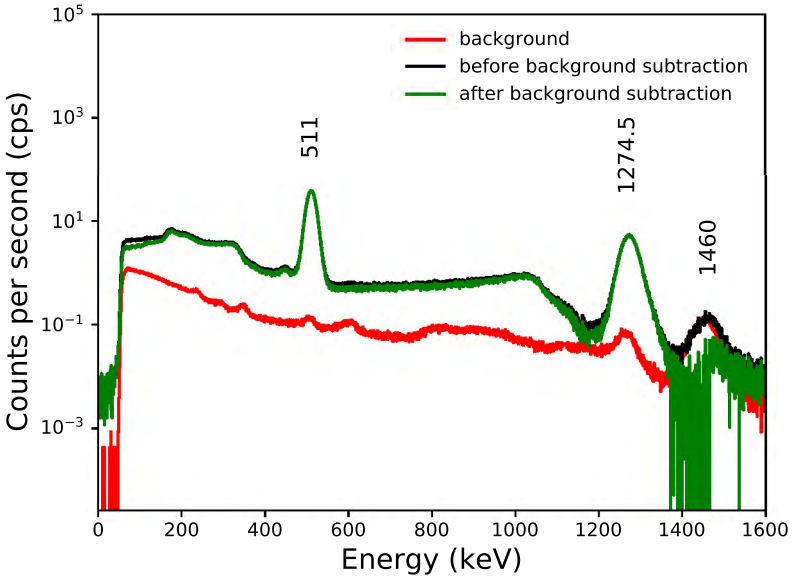

Fig. 3.21: Energy spectrum of ^{22}Na before (black) and after (green) background subtraction. The background radiation (red) is also shown. The 511 keV and 1275 keV peaks result from the decays of ^{22}Na, whereas the 1460 keV peak is due to the decay of ^{40}K present in the background.

also a few cases of peak convolution. This kind of convolution occurs when the energy resolution of the detector is insufficient to distinguish between gamma-ray peaks of similar energies. It is seen that there are two convoluted peaks centred at 411 and 444 keV. Another convolution is not as obvious, because it seemingly appears as a single photopeak. However, the gamma emissions at energies 1086 and 1112 keV are in fact separate photopeaks. Another convolution can be seen between the 1408 and 1460 keV peaks. As mentioned, the 1460 keV peak is a result of the background decay of ^{40}K, and as such, the background subtraction effectively de-convolutes the two peaks.

Appendix A provides a tabulated list of the gamma-ray emission energies (E_γ) from ^{22}Na and ^{152}Eu along with their corresponding intensities (I_γ) [7, 43]. Only energies with $I_\gamma > 0.1\%$ are considered, since energies with lower intensities are virtually imperceptible in the energy spectra shown.

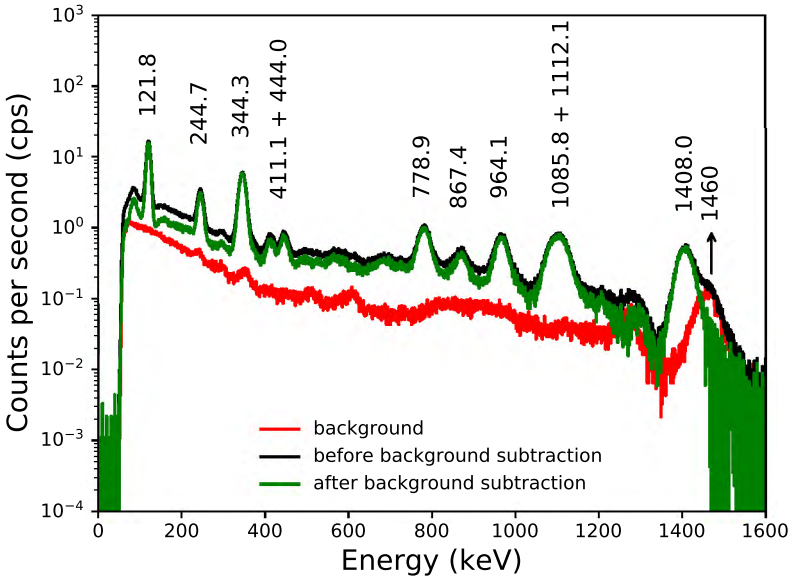

Fig. 3.22: Energy spectrum of ^{152}Eu before (black) and after (green) background subtraction, with the background (red) also indicated. All peaks indicated result from the gamma emissions of ^{152}Eu, with the only exception of the 1460 keV peak, which is due to the decay of ^{40}K present in the background.

4 Considerations for detector geometry

There were a number of factors that were considered when choosing the geometry of the detector system shown in Fig. 3.1. These considerations include the detection efficiency of the set-up, the activity of the ^{22}Na source (while ensuring high count rates), and the total dead time and pulse pile-up effects of the detector system. Most of these factors are correlated to each other in some way. For example, increasing the activity of the source at a fixed distance will have the effect of increasing both the dead time and peak pulse pile-up effects in the system. Each of these factors are considered to determine the optimal detector system set-up that maximises the detector system count rate and detection efficiency while minimising peak pulse pile-up and dead time effects.

4.1 Experimental set-up and geometry for measurements

Fig. 4.1 shows the experimental set-up that was used to conduct the efficiency, count rate, dead time, and peak pulse pile-up measurements shown in the following sections. A single 2 × 2" $LaBr_3$:Ce detector was used to measure the gamma radiation from a radioactive source (either ^{22}Na or ^{152}Eu, depending on the measurement). The detector had an operating HV of −1100 V, and was operated in singles mode (with channel trigger validation disabled for both the slow and fast signals). The rest of the associated electronics, DSP settings, and data acquisition for these measurements were the same as previously described in Section 3.2.

Fig. 4.2 shows the situation for a radioactive point source S located a distance d along the axis of a cylindrical detector of radius r. For this situation, the solid angle Ω is given as [19],

$$\Omega = 2\pi \left(1 - \frac{d}{\sqrt{d^2 + r^2}}\right). \tag{4.1}$$

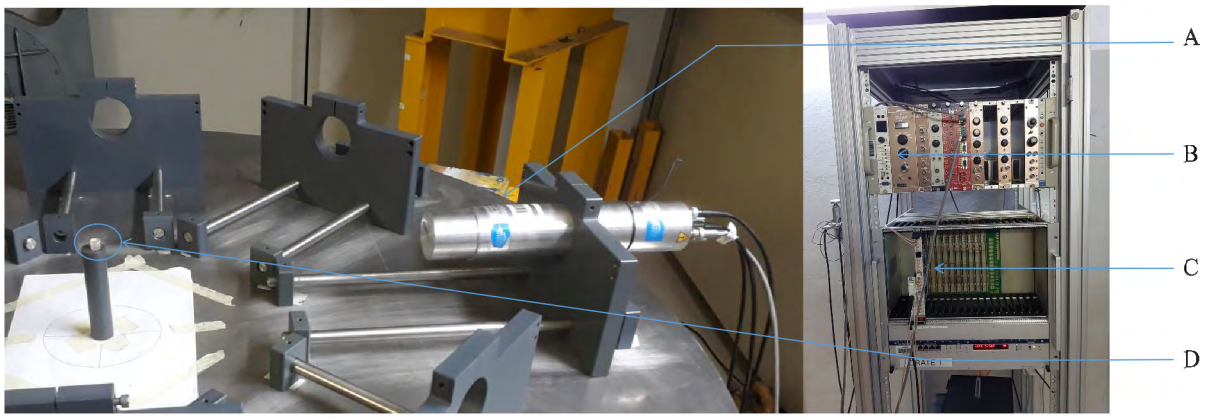

Fig. 4.1: A radioactive source is placed a measured distance away from a 2 × 2" $LaBr_3$:Ce detector. The associated electronics and DSP settings are the same as before (see Section 3.2). (A = $LaBr_3$:Ce detector, B = High voltage supply, C = Pixie-16, D = Radioactive source on plastic stand).

There is an evident similarity between the set-up in Fig. 4.1 and the situation in Fig. 4.2. By making the simplifying assumption of a point source in Fig. 4.1, Ω is then given by equation (4.1). This approximation for Ω was used in the calculations performed in the following sections.

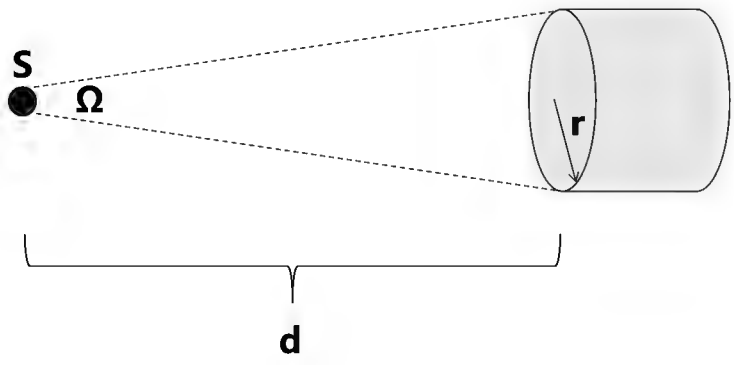

Fig. 4.2: A radioactive source S is located a distance d along the axis of a cylindrical detector of radius r. The solid angle Ω for this situation is given by equation (4.1).

4.2 Detection efficiency

The theory and relevant definitions for detection efficiency were covered in Section 2.5.2. This section will look to use those definitions to perform efficiency calculations for a particular detector geometry (described in Section 4.1). The relationships of the detection efficiency as functions of energy and source-to-detector distance are explored through both theoretical calculations and practical experiment.

4.2.1 Detection efficiency calculated from theoretical detector properties and geometry

Theoretical calculations are often a useful method of determining what results should be expected from a particular experiment. In this case, theoretical predictions of E_{FEP} and $E_{FEP,int}$ for specific energies are determined using calculations that involve the properties and geometry of the detector set-up in Fig. 4.1. The energies that were chosen for the calculations in this

section correspond to the gamma-ray emission energies of ^{152}Eu.

Following Saint-Gobain Crystal's document for efficiency calculations [44], E_{FEP} is the product of three factors, namely G, I and M, such that,

$$E_{FEP} = G \times I \times M, \tag{4.2}$$

where G represents the fraction of all space subtended by the detector, I represents the fraction of the photons transmitted by the intervening materials that reach the detector surface, and M represents the fraction of the photons absorbed by the detector.

G is the factor which concerns the geometry of the source-to-detector system. It is calculated using,

$$G = \frac{\pi r^2}{4\pi R^2}, \tag{4.3}$$

where πr^2 is the area of the detector face, and $4\pi R^2$ is the area of sphere with a radius equal to the source-to-detector distance.

I concerns the losses due to absorption by material in the path of the photon. It is calculated using,

$$I = \prod_i e^{-\mu_i \rho_i d_i}, \tag{4.4}$$

where μ_i represents the attenuation coefficient of absorption material i at a particular energy, ρ_i represents its density, and d_i represents the distance travelled by the photons through the material i. In the particular case of the detector set-up in Fig. 4.1, the notable absorption materials between the source and scintillating material include the air and the Al housing of the scintillator. So equation (4.4) then becomes,

$$I = \exp\left(-\mu_{air}\rho_{air}d_{air}\right) \exp\left(-\mu_{Al}\rho_{Al}d_{Al}\right) \tag{4.5}$$

Lastly, M is the factor which determines how many of the transmitted photons are absorbed into the material, and it is calculated by subtracting the fraction of photons that pass through the detector from 1,

$$M = 1 - e^{-\mu_s \rho_s d_s}, \tag{4.6}$$

where μ_s is the attenuation coefficient of the scintillating material at a particular energy, ρ_s represents its density, and d_s is the distance travelled by the photons through the scintillating material.

Using the XCOM photon cross sections database [45, 46] developed by the National Institute of Standards and Technology (NIST), the attenuation coefficients for air, Al and $LaBr_3$:Ce were obtained for specific gamma-ray emission energies of ^{152}Eu, and are listed in Table 4.1. It shows two sets of attenuation coefficient values, namely one which assumes coherent (or Rayleigh) scattering, and the other which assumes incoherent (or Coulomb) scattering.

In order to determine which set of attenuation coefficients is the most applicable to use for these calculations, it is useful to observe the residuals between the E_{FEP} calculated from both of these coherent and incoherent scattering values. These residuals are shown in Fig. 4.3. It is seen that these residuals agree with unity over the observed energy range, which implies that there is no discernible difference between using either of these sets of coefficients in the calculations. With this being the case, the attenuation coefficients for incoherent scattering were selected for the resulting E_{FEP} calculations. It is worth noting that the attenuation coefficients

Table 4.1: Attenuation coefficients for air, Al and $LaBr_3$:Ce for various energies are shown both with coherent and incoherent scattering effects. The energies chosen correspond to the gamma-ray emission energies of ^{152}Eu. These values were obtained from the XCOM photon cross sections database [45, 46].

	μ_{air} (cm^2g^{-1})		μ_{Al} (cm^2g^{-1})		μ_s (cm^2g^{-1})	
Energy (keV)	**Coherent**	**Incoherent**	**Coherent**	**Incoherent**	**Coherent**	**Incoherent**
121.8	1.447×10^{-1}	1.411×10^{-1}	1.522×10^{-1}	1.430×10^{-1}	9.702×10^{-1}	9.056×10^{-1}
244.7	1.150×10^{-1}	1.141×10^{-1}	1.129×10^{-1}	1.106×10^{-1}	2.212×10^{-1}	2.032×10^{-1}
344.3	1.013×10^{-1}	1.009×10^{-1}	9.863×10^{-2}	9.742×10^{-2}	1.361×10^{-1}	1.267×10^{-1}
778.9	7.165×10^{-2}	7.156×10^{-2}	6.927×10^{-2}	6.903×10^{-2}	6.806×10^{-2}	6.614×10^{-2}
867.4	6.809×10^{-2}	6.801×10^{-2}	6.584×10^{-2}	6.565×10^{-2}	6.360×10^{-2}	6.205×10^{-2}
964.1	6.472×10^{-2}	6.466×10^{-2}	6.257×10^{-2}	6.241×10^{-2}	5.961×10^{-2}	5.836×10^{-2}
1408.0	5.349×10^{-2}	5.346×10^{-2}	5.172×10^{-2}	5.165×10^{-2}	4.810×10^{-2}	4.750×10^{-2}

for coherent scattering could have been used instead, but the resulting calculations would essentially lead to the same results.

The dimensions used for the $LaBr_3$:Ce detector were the same as the model used by Mouhti *et al.* [47] (shown in Fig. 4.4).

The E_{FEP} curves shown in Fig. 4.5 (a) were calculated using the theoretical model of equation (4.2), the detector dimensions shown in Fig. 4.4, and the attenuation coefficients for incoherent scattering in Table 4.1. Three source-to-detector distances are considered, namely 15 cm, 30 cm and 45 cm. As expected, the closer the source is placed to the detector, the larger the E_{FEP} over the energy spectrum. This is due to Ω being larger at closer distances, which means more of the radiation emitted by the source will interact with the surface of the detector, leading to higher count rates being recorded. It is also seen that at higher energies, the E_{FEP} decreases. This is because at higher energies there is a lower probability that all of the energy from incident radiation will be deposited in the detector.

Fig. 4.5 (b) shows the $E_{FEP,int}$ energy curves which were obtained by applying equation (2.11) to the E_{FEP} curves in Fig. 4.5 (a). It is seen that each of the curves at the various distances are in agreement with each other, which suggests that $E_{FEP,int}$ has much less of a geometric dependence than E_{FEP} (as was previously noted in Section 2.5.2).

4.2.2 Detection efficiency obtained from measurement of a ^{152}Eu radioactive source

Using the experimental set-up in Section 4.1 (with a ^{152}Eu radioactive source of activity 4.5 (4) μCi), measurements were performed to determine the total number of counts recorded under the energy peaks of ^{152}Eu. These counts were corrected for background radiation through the method described in Section 3.7. Using these measurements, along with equations (2.10) and (2.11), the efficiency curves presented in Fig. 4.6 (a) and (b), respectively, were produced.

Fig. 4.6 (a) shows the E_{FEP} energy curves using the ^{152}Eu source placed at three separate distances away from the detector, namely, 15 cm, 30 cm and 45 cm. Similarly to the theoretically-obtained E_{FEP} curves in Fig. 4.5 (a), it is seen that the measured E_{FEP} increases as the source-to-detector distance decreases, and there is also a decrease in E_{FEP} for higher radiation energies.

Fig. 4.6 (b) shows the $E_{FEP,int}$ energy curves obtained by applying equation (2.11) on the

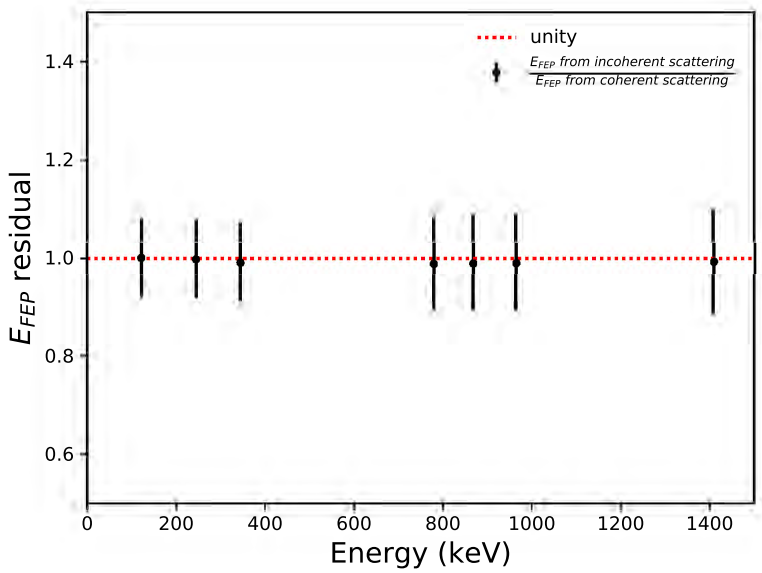

Fig. 4.3: Residual between the full-energy peak efficiencies calculated using attenuation coefficients that assume incoherent and coherent scattering over the energy range 121−1408 keV. The attenuation coefficients are provided in Table 4.1. These residuals are in agreement with unity over the observed energy range.

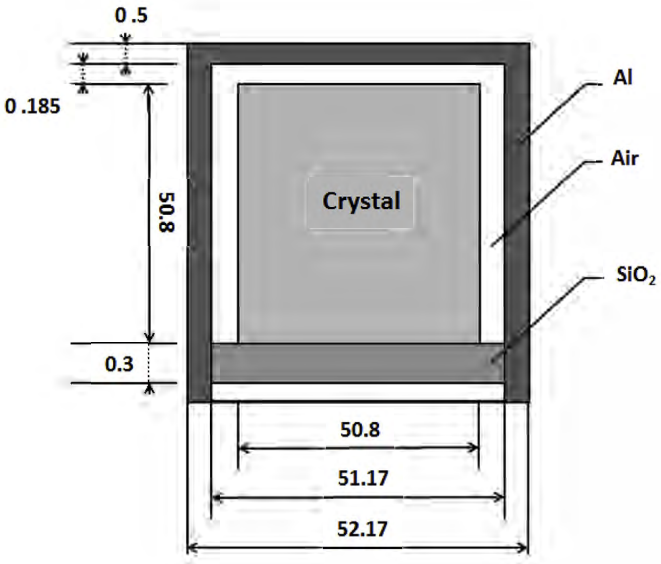

Fig. 4.4: Inner structure of the 2×2" $LaBr_3$:Ce detector considered in the calculations of the full-energy peak efficiencies using the theoretical model (4.2). The dimensions of the detector are indicated in mm. This image was adapted from Mouhti *et al.* [47]

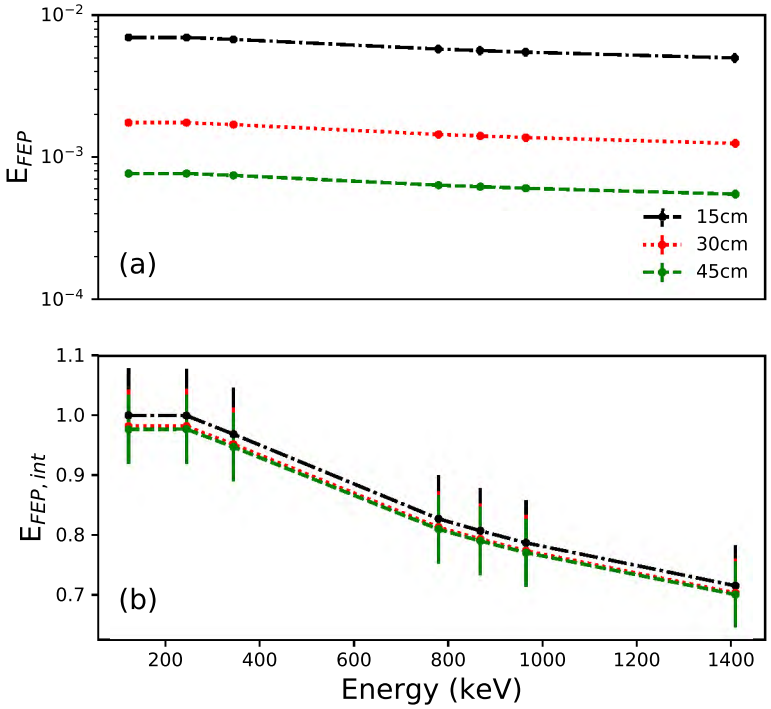

Fig. 4.5: (a) Full-energy peak efficiency, and (b) intrinsic full-energy peak efficiency, obtained from calculations using the theoretical model (4.2) for a theoretical ^{152}Eu source that is placed 15 cm (black), 30 cm (red) and 45 cm (green) from a 2 × 2" $LaBr_3$:Ce detector.

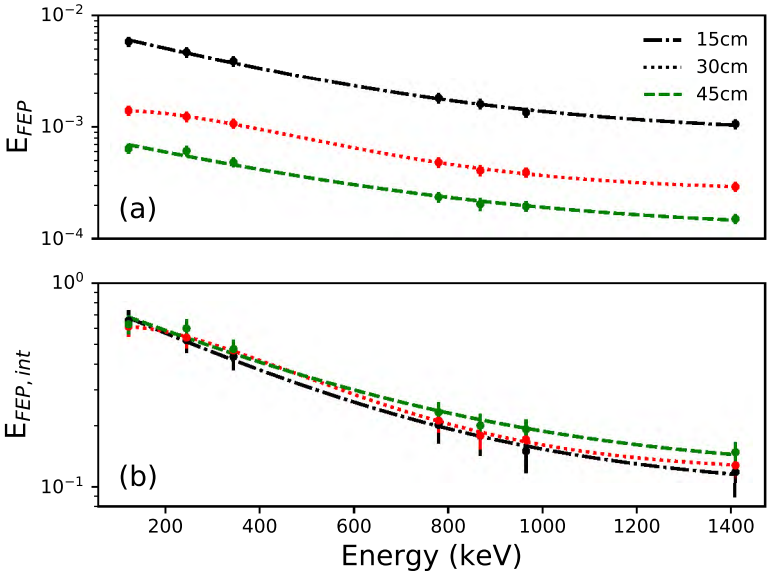

Fig. 4.6: (a) Full-energy peak efficiency and (b) intrinsic full-energy peak efficiency curves, using a ^{152}Eu radioactive source that is placed 15 cm (black), 30 cm (red) and 45 cm (green) from a 2 × 2" $LaBr_3$:Ce detector.

E_{FEP} curves in Fig. 4.6 (a). It is seen that each of the curves at the various distances are in approximate agreement with each other (which is consistent with what is shown for the theoretically-obtained $E_{FEP,int}$ curves in Fig. 4.5 (b)).

The mathematical model that is used to fit the experimental data in Fig. 4.6 (a) is the commonly-used [48] double exponential,

$$E_{FEP}(E_\gamma) = A\exp(-BE_\gamma) + C\exp(-DE_\gamma), \tag{4.7}$$

with parameters A, B, C and D (and their associated uncertainties) determined by the fit. These fit parameter values for Fig. 4.6 (a) have been tabulated in Table 4.2.

Table 4.2: Fit parameters A, B, C and D along with their associated uncertainty values for the double exponential in equation (4.7). The fit is performed for the $E_{FEP,int}$ energy curves in Fig. 4.6 (a).

Distance (cm)	A	u(A)	B	u(B)	C	u(C)	D	u(D)
15	7.45×10^{-3}	7.12×10^{-4}	2.18×10^{-3}	3.33×10^{-4}	2.13×10^{-4}	2.32×10^{-4}	8.56×10^{-4}	6.90×10^{-4}
30	1.80×10^{-3}	1.63×10^{-4}	1.69×10^{-3}	2.46×10^{-4}	4.73×10^{-7}	4.46×10^{-6}	3.96×10^{-3}	6.46×10^{-3}
45	8.22×10^{-4}	7.74×10^{-5}	1.60×10^{-3}	2.90×10^{-4}	3.86×10^{-7}	3.64×10^{-6}	3.64×10^{-3}	6.42×10^{-3}

4.2.3 Comparison between theoretical and experimental detection efficiencies

Since it is clear from observation that there is a notable difference between the theoretically- and experimentally-obtained E_{FEP} energy curves, it is informative to consider the residual between these curves. These residuals are defined as the quotient between the E_{FEP} values in Fig. 4.5 (a) and Fig. 4.6 (a), respectively. The resulting residual curves are shown in Fig. 4.7. The ideal scenario in this case would be for the residuals to be identically unity over the range of energy values (121−1408 keV), as this would mean that the theoretical calculations performed in Section 4.2.1 are consistent with the calculations from measurement in Section 4.2.2. However, it is seen that for lower energies, the residuals are around 80%. These residuals gradually decrease over the increasing energy range to around 25% at 1408 keV. This suggests that the theoretical model in equation (4.2) becomes increasingly worse for increasing energy values.

Possible explanations for this observation of the residual behaviour come from the assumptions that are made in these calculations. Firstly it is assumed that the probability for photons scattering out of the detector (out-scattering) is the same throughout the material. Ordinarily this would not be a bad assumption, however, when considering the fact that the photons are emitted from an isotropic point source, this means that the incident photons will have various orientations and impact positions at their respective points of first interaction in the scintillator. This model would then suggest that an incident photon on the outer limits of the Ω-cone would have the same probability of out-scattering as an incident photon in the centre of the Ω-cone. This is clearly not true, and is therefore a limitation in the model. This effect would also be energy dependent, since higher energy photons are likely to experience more scattering effects.

Another consideration which has not been accounted for is that higher energy photons tend to transverse more material than lower energy photons before any interaction within the scintillator. This could potentially have a significant effect on the measurement, and it should be noted that this is also energy dependent.

The calculations also do not allow for multiple photon emissions per decay (which is not consistent with the case of ^{152}Eu). These multiple photon emissions could lead to measurable increases or decreases (depending on the solid angle) in the E_{FEP} due to coincidence summing effects [49].

Lastly, Berger *et al.* [46] note several factors that are not considered for the XCOM database (which have bearing on the calculated absorption coefficients shown in Table 4.1). These include:

- Molecular and solid-state effects are not accounted for, which may modify the cross sections used in the database by up to 5% (especially in the vicinity of absorption edges).
- Relatively small cross sections (such as Delbrück scattering, two-photon Compton scattering or photo-meson production) are not included.
- Energy absorption coefficients that represent the conversion of photon energy to kinetic energy of secondary Compton-, photo-, and pair-electrons are not calculated.
- The nuclear photoeffect is not accounted for, which may contribute a few additional percent to the total attenuation coefficient in the giant-dipole resonance region from 5 MeV to 30 MeV (five times greater than the energy ranges considered in this work).

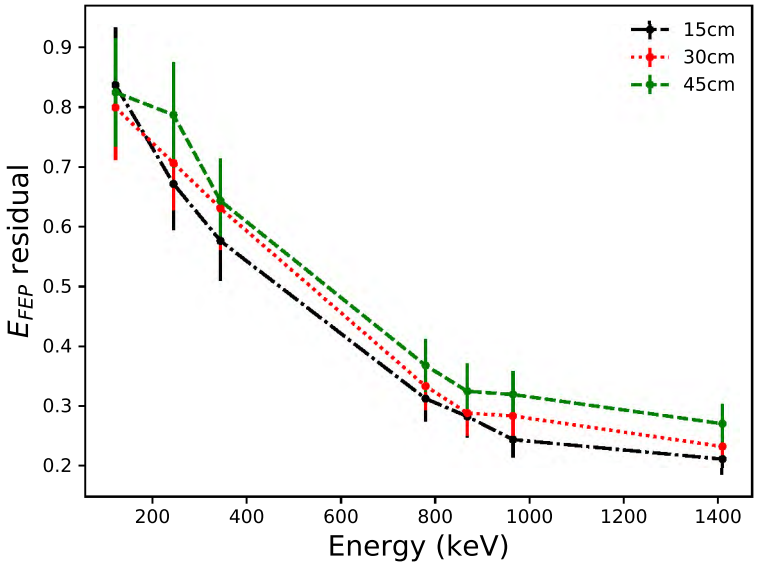

Fig. 4.7: Residuals between theoretically- and experimentally-obtained E_{FEP} over the energy range 121−1408 keV. The residual is defined as the quotient between the E_{FEP} values in Fig. 4.5 (a) and Fig. 4.6 (a), respectively, and is considered for source-to-detector distances of 15 cm (black), 30 cm (red) and 45 cm (green).

4.2.4 Detection efficiency obtained from measurement of a ^{22}Na radioactive source

Using the experimental set-up in Section 4.1 (with a ^{22}Na radioactive source of activity 9 (1) μCi), measurements were performed to determine the total number of (background-corrected) counts recorded under the energy peaks of ^{22}Na (namely, the energy peaks at 511 keV and 1275 keV). Using these measurements with equations (2.10) and (2.11), the efficiency curves shown in Fig. 4.8 (a) and (b), respectively, were produced. These measurements of the E_{FEP} and $E_{FEP,int}$ values are shown as functions of source-to-detector distance for the fixed energy peak values of 511 keV and 1275 keV.

From Fig. 4.8 (a), it is seen that E_{FEP} is dependent on both energy and source-to-detector

distance (which was previously inferred from Fig. 4.6 (a)). Fig. 4.8 (b) shows that $E_{FEP,int}$ is dependent on the incident radiation energy, but remains relatively constant as a function of source-to-detector distance. Again, this is consistent with what was observed in Fig. 4.6 (b).

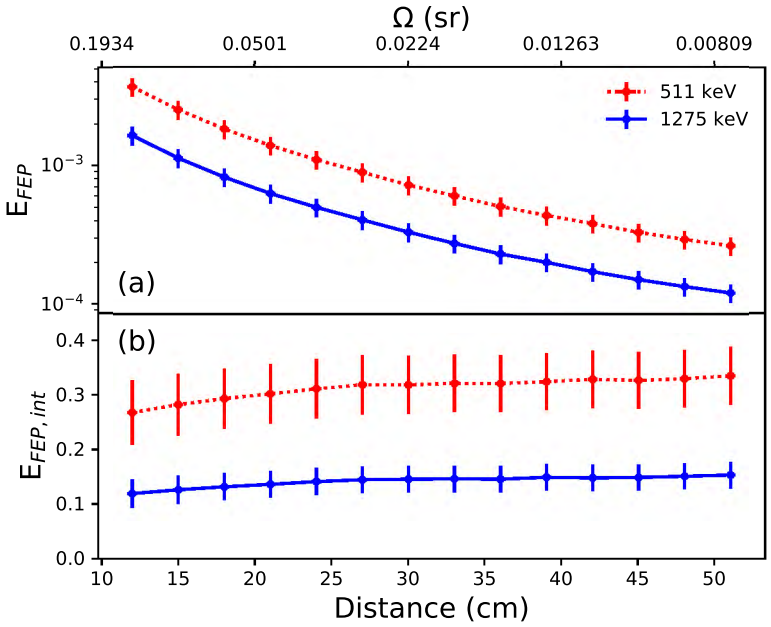

Fig. 4.8: (a) Full-energy peak efficiency and (b) intrinsic full-energy peak efficiency curves, using a ^{22}Na source at energies 511 keV (red) and 1275 keV (blue). The curves are shown as functions of source-to-detector distance (lower axis), and Ω (upper axis).

4.2.5 Comparison between detection efficiencies from experimental fit and experimental measurement

To confirm that all of the measurements and calculations performed in the preceding sections are self-consistent, a comparison is made between E_{FEP} values obtained using different methods. In Section 4.2.2, the E_{FEP} energy curves in Fig. 4.6 (a) were obtained from the measurement of a ^{152}Eu source, and were considered for source-to-detector distances of 15 cm, 30 cm, and 45 cm. In contrast, in Section 4.2.4, the E_{FEP} distance curves in Fig. 4.8 (a) were obtained from the measurement of a ^{22}Na source, and were considered at energies of 511 keV and 1275 keV. Thus between them, these E_{FEP} curves have six points in common, each of which are listed and compared in Table 4.3. The 'Fitted' E_{FEP} values are obtained from Fig. 4.6 (a), and calculated using the fit parameters in Table 4.2 and double exponential fit in equation (4.7) with $E_\gamma = 511$ keV and $E_\gamma = 1275$ keV. The 'Measured' E_{FEP} values were obtained directly from the measurements shown in Fig. 4.8 (a). From Table 4.3, it is seen that each of the corresponding 'Fitted' and 'Measured' values for E_{FEP} are in agreement (as expected).

4.3 Count rate of a single 2×2" $LaBr_3$:Ce detector

It is important for this experiment that the count rate in the detector system is maximised. The four-photon branching ratio is small ($\sim 10^{-6}$), and so a high count rate will allow for the total measurement period to be minimised (which is always ideal).

The count rate of a detector system is linearly related to both the activity of the radioactive source and the solid angle Ω of the source-to-detector system. In order to empirically relate these quantities, various count rate measurements (using the experimental set-up described in

Table 4.3: 'Fitted' and 'Measured' E_{FEP} values for the 511 keV and 1275 keV energy peaks of ^{22}Na for source-to-detector distances of 15 cm, 30 cm and 45 cm. The 'Fitted' E_{FEP} values were calculated using the fit parameters in Table 4.2 and double exponential fit in equation (4.7) with $E_\gamma = 511$ keV and $E_\gamma = 1275$ keV. The 'Measured' E_{FEP} values were obtained directly from the measurements in Fig. 4.8 (a).

	$E_\gamma = 511$ **keV**		$E_\gamma = 1275$ **keV**	
Distance (cm)	**Fitted** E_{FEP}	**Measured** E_{FEP}	**Fitted** E_{FEP}	**Measured** E_{FEP}
15	2.78 (61)$\times 10^{-3}$	2.51 (38) $\times 10^{-3}$	1.10 (91)$\times 10^{-3}$	1.13 (17)$\times 10^{-3}$
30	7.6 (12)$\times 10^{-4}$	7.2 (11)$\times 10^{-4}$	2.8 (92)$\times 10^{-4}$	3.32 (50)$\times 10^{-4}$
45	3.65 (68)$\times 10^{-4}$	3.32 (50)$\times 10^{-4}$	1.5 (50)$\times 10^{-4}$	1.52 (23)$\times 10^{-4}$

Section 4.1) were performed with ^{22}Na sources of several activities at various Ω values. Descriptions of the ^{22}Na sources' activities used in these measurements have been tabulated in Table 4.4. The table shows eight sources, with sources 1, 3, 5 and 8 using a single radioactive sample, and sources 2, 4, 6 and 7 using two samples.

Table 4.4: Information of the activities of ^{22}Na sources used for count rate measurements. ^{22}Na has a half life of 2.602 (22) years, which was used to determine the corrected activity from the radioactive decay law. Sources 1, 3, 5 and 8 use a single radioactive sample, while sources 2, 4, 6 and 7 use two radioactive samples (with the accumulative activity being equivalent to the sum of the activities of the two samples).

	source 1	**source 2**		**source 3**	**source 4**		**source 5**	**source 6**		**source 7**		**source 8**
Sample type	Single	Double		Single	Double		Single	Double		Double		Single
Initial activity (μCi)	138 (21)	134 (20)	138 (21)	39.7 (60)	39.7 (60)	18.8 (28)	76 (11)	76 (11)	21.0 (32)	134 (20)	496 (74)	496 (74)
Calibration date	12/11/2009	12/11/2009	12/11/2009	9/11/2020	9/11/2020	9/11/2020	9/11/2020	9/11/2020	9/11/2020	12/11/2009	30/07/2015	30/07/2015
Corrected activity (μCi)	9.2 (14)	7.8 (12)	8.0 (12)	39.7 (60)	39.7 (60)	18.8 (28)	76 (11)	76 (11)	21.0 (32)	7.8 (12)	130 (20)	143 (21)
Accumulative activity (μCi)	**9.2 (14)**	**15.8 (17)**		**39.7 (60)**	**58.5 (66)**		**76 (11)**	**97 (14)**		**138 (20)**		**143 (21)**

The count rates shown in this section are referred to as singles count rates (since they were measured with a single detector). In order to determine the singles count rate of a detector, it is beneficial to observe the detected number of counts as a function of time. Fig. 4.9 (a) shows this for source 2 placed at a source-to-detector distance of 14.1 cm. The most obvious observation to note is that the count rate is clearly not at a steady constant due to the presence of artefacts A, B, C and D. These artefacts are due to the dead time in the detector system, which causes a few seconds of detection to effectively be lost. These dead time effects are discussed in further detail in Section 4.5. It is interesting to note in Fig. 4.9 (b) is that if the count rate were naively calculated by simply dividing the total number of counts by the total measurement time, this would result in a 'total average' = 9694 (32) cps, which is evidently less than the observed steady-state count rate. This issue was tackled by only considering the time average over regions with no observed dead time. In the case of Fig. 4.9 (b), the range 800−1300 s was considered to produce a 'ranged average' = 9839.5 (43) cps. This is a significant improvement over the previous value, particularly to the uncertainty.

All subsequent count rate averages shown in this report were calculated by similar means.

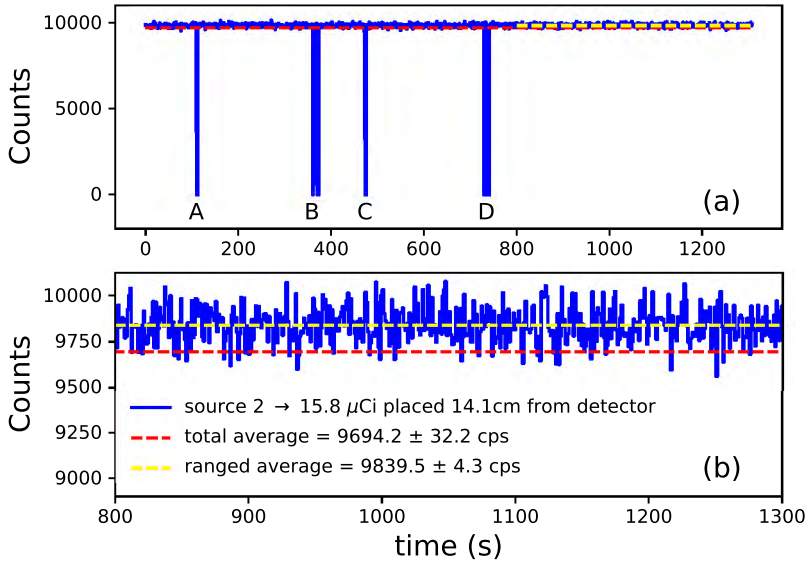

Fig. 4.9: (a) shows the number of counts detected in a single 2 × 2" $LaBr_3$:Ce detector as a function of time using source 2 placed at a source-to-detector distance of 14.1 cm. Artefacts A, B, C and D are identified regions of dead time which have the effect of significantly lowering the total average count rate.
(b) shows the time range 800−1300 s, which demonstrates a steady count rate (with no regions of observable dead time). A ranged average count rate over this region shows a clear improvement for determining the actual count rate of the detector system (through exclusion of the dead time regions).

It is useful to note that a ^{22}Na source with a larger activity placed at a smaller solid angle Ω should be equivalent (in terms of average singles count rate) to a weaker activity source placed at a larger Ω. With this is mind, it becomes beneficial to define an 'effective activity',

$$A_{\text{eff}} = \mathcal{A} \times \Omega, \tag{4.8}$$

where $\mathcal{A}$ denotes the activity of the ^{22}Na source. Fig. 4.10 shows A_{eff} as a function of average singles count rate for the (a) slow, (b) fast and (c) QDC signals. At first glance, this relationship appears to be linear, however, since the count rate is linear in both $\mathcal{A}$ and Ω, this implies that their product $A_{\text{eff}} = \mathcal{A} \times \Omega$ is (in general) quadratic in nature. For this reason, a quadratic function was fitted to the data,

$$A_{\text{eff}}(x) = ax^2 + bx, \tag{4.9}$$

where a and b represent the parameters to be determined by the fit, while x represents the average singles count rate. For each signal, the determined fit parameters are tabulated in Table 4.5, and plotted in Fig. 4.10.

Table 4.5: Parameters a and b determined from the quadratic fit in equation (4.9) for the slow, fast, and QDC signals from a 2×2" $LaBr_3$:Ce detector. These fit parameters are used to plot the quadratic functions seen in Fig. 4.10.

Fit parameters	**Slow signal**	**Fast signal**	**QDC signal**
a	$7.27\ (57) \times 10^{-10}$	$8.03\ (44) \times 10^{-10}$	$1.809\ (47) \times 10^{-9}$
b	$1.451\ (13) \times 10^{-4}$	$1.37846\ (82) \times 10^{-4}$	$1.40556\ (76) \times 10^{-4}$

With this quadratic model in place, this means that an effective activity can be related to any given average singles count rate for each of the slow, fast and QDC signals. The question that now remains is how the average singles count rate should be selected for the detector system. There is an inherent limitation on the maximum count rate that can be detected due to the measurement capabilities of the $LaBr_3$:Ce detector i.e. the singles count rate saturates at $\sim$ 65000 cps. There is, however, additional factors which are important to consider. One such factor is the effect that the count rate has on the resolution of the peaks in the energy spectrum. For simplicity, only the energy resolution of the 511 keV peak of ^{22}Na is considered for this analysis. Fig. 4.11 shows this resolution as a function of average singles count rate for the (a) slow, (b) fast, and (c) QDC signals. For the slow signal, it is seen that the energy resolution exponentially increases with average count rate to as high as 27%. In contrast, the resolution for the fast and QDC signals remain fairly constant for an increasing average count rate. Fig. 4.11 (a) is extremely useful in that it quantifies the trade-off required of energy resolution to produce high count rates for the slow signal. An exponential was chosen as a fit to the data based on the observed relationship between count rate and energy resolution. The exponential fit in Fig. 4.11 (a),

$$R_E(x) = \alpha e^{\beta x} + \kappa, \tag{4.10}$$

has fit parameters $\alpha = 0.1112\ (15)$, $\beta = 7.665\ (26) \times 10^{-5}$ and $\kappa = 4.4563\ (22)$, where R_E is the energy resolution of the 511 keV peak (which is a function of the average singles count rate x).

With some manipulation, equation (4.10) allows for a selected energy resolution to be mapped to an average count rate. For this work, an upper limit of 10% is selected for the energy resolution of the 511 keV peak for the slow signal (i.e. the energy resolution is not to exceed 10%). Using equation (4.10), this means that the average singles count rate should not exceed,

$$\mathcal{C}_{\text{max}} = 5.100\ (25) \times 10^4 \text{ cps}. \tag{4.11}$$

It is worth noting that $\mathcal{C}_{\text{max}}$ is less than the observed saturation count rate of the detector ($\sim$ 65000 cps), while preserving a reasonable energy resolution of 10% at 511 keV for the slow signal.

Substituting $\mathcal{C}_{\text{max}}$ into equation (4.9) (and using the fit parameter values provided in Table 4.5),

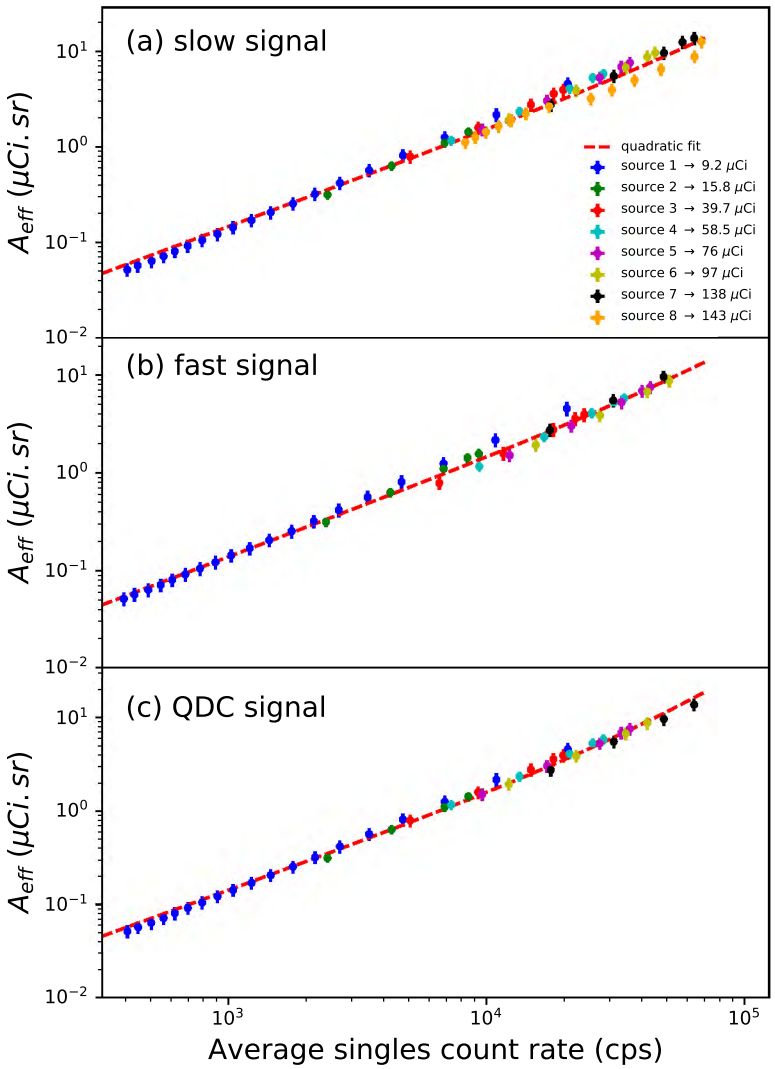

Fig. 4.10: Effective activity A_{eff} (4.8) plotted as a function of average singles count rate for the (a) slow, (b) fast, and (c) QDC signals. Sources of eight different activities placed at various Ω values were used to generate the data points (with their details tabulated in Table 4.4). The quadratic function in equation (4.9) is fitted to the data with the fit parameters being tabulated in Table 4.5.

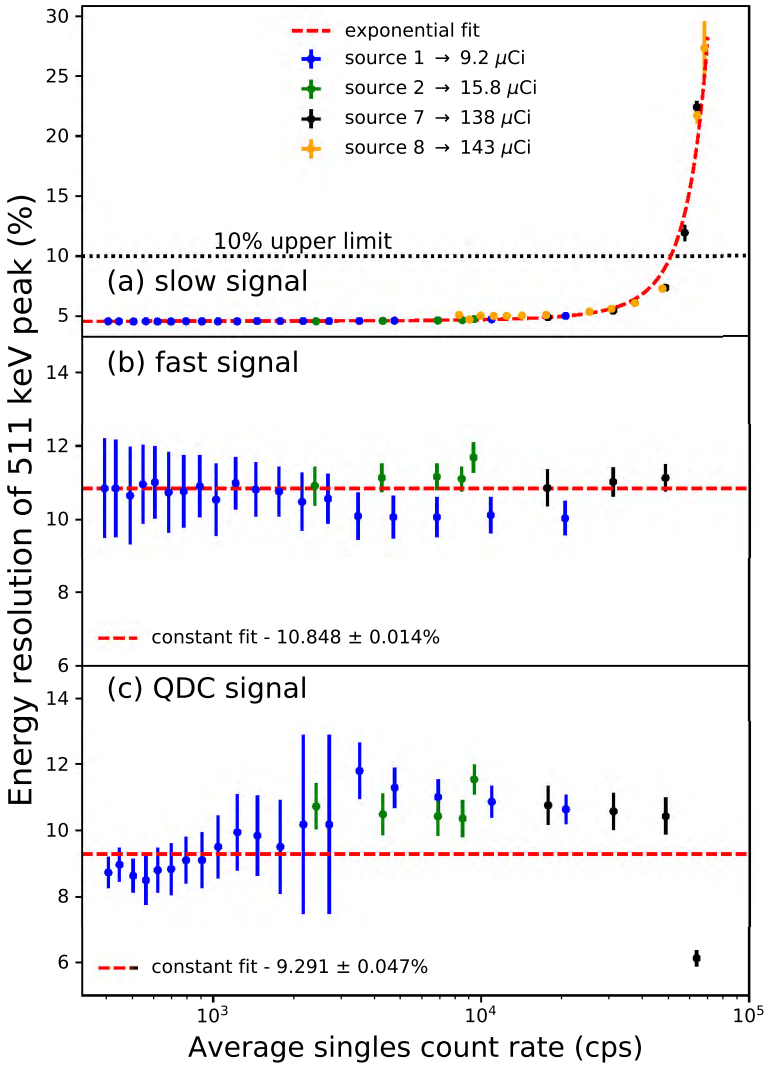

Fig. 4.11: The energy resolution of the 511 keV peak of ^{22}Na as a function of average singles count rate for the (a) slow, (b) fast, and (c) QDC signals. Sources 1, 2, 7 and 8 were placed at various Ω and used to generate the data points (with the details of their respective activities tabulated in Table 4.4). The exponential function (4.10) is fitted to the slow signal data with determined fit parameters $\alpha = 0.1112\ (15)$, $\beta = 7.665\ (26) \times 10^{-5}$ and $\kappa = 4.4563\ (22)$. An upper limit of 10% was selected for the energy resolution of the 511 keV peak for the slow signal, which corresponds to an average count rate of $\mathcal{C}_{\max} = 5.100\ (25) \times 10^4$ cps.

the effective activities for each of the slow, fast and QDC signals are shown in Table 4.6. These values will prove useful further into the work.

Table 4.6: Effective activities for slow, fast and QDC signals calculated using equation (4.9). These values correspond to an average singles count rate of 5.100 (25) $\times 10^4$ cps.

Signal type	Slow	Fast	QDC
A_{eff} (μCi.sr)	9.29 (17)	9.12 (13)	11.87 (15)

4.4 Peak pulse pile-up effects

As the count rate of a detector system increases (either through increasing the activity of the source, or by increasing Ω between the source and detector), the average time difference between the detection of two consecutive energy pulses decreases. This can consequently result in the measured pulses interfering with each other through a superposition of the signals, which could lead to the reduction of both energy resolution and photopeak efficiency. This section serves to quantify the degree to which this effect influences the measurements of 511 keV photons.

Peak pulse pile-up is a term that refers to an artificially created energy peak that is resultant from the superposition of pulses from gamma-ray emissions. It occurs when two pulses are detected within a sufficiently small time window such that they are treated as a single pulse by the acquisition system. Fig. 4.12 shows an example of the peak pile-up effect for the pulses of 511 keV and 1275 keV for the slow, and fast signals of a ^{22}Na source. As shown, the superposition of the pulses for the slow signal results in an amplitude that is equal to the sum of their individual amplitudes. This effect results in the acquisition system registering the combined superposition as a single pulse, which then is recorded as a count of energy 511 keV + 1275 keV = 1786 keV. This is how the 1786 keV peak is artificially created (since there is no physical reason for its existence). In contrast to the slow signal, it is seen that the pulses of the fast signal do not undergo any sort of superposition, because the decay constant τ of the fast signal is approximately 1000 times smaller than that of the slow signal (as demonstrated in Section 3.3). The quicker decay of the detected pulses leads to the peak pulse pile-up effect being less of an occurrence for the fast signal.

Fig. 4.13 shows energy spectra measured with the experimental set-up described in Section 4.1, and using a 9 μCi ^{22}Na source with a source-to-detector distance of 6 cm. The usual gamma-ray emissions indicated, as well as a prominent 1786 keV pile-up peak for both the slow and fast signals. It should be noted that despite the quick decay of the fast signal pulses, there is still significant pile-up which is observed.

The peak pile-up should ideally be minimised, since these are artificial counts which do not represent a physical decay. In order to observe the degree to which the peak pile-up affects the energy measurements, a peak pile-up ratio is defined as,

$$\mathcal{P} = \frac{\text{Total counts in 1786 keV peak}}{\text{Total counts in 511 keV peak}}. \tag{4.12}$$

Fig. 4.14 shows $\mathcal{P}$ plotted as a function of Ω on the lower axis, and source-to-detector distance on the upper axis. These measurements were performed using the ^{22}Na sources listed in Table 4.4, and the experimental set-up described in Section 4.1. It is seen that the effect of the peak pile-up increases with both the activity of the measured ^{22}Na source and the Ω at which it

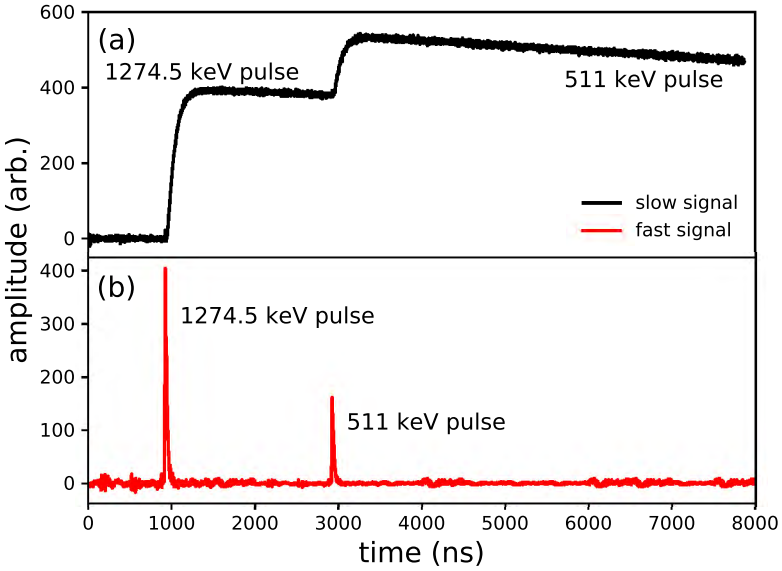

Fig. 4.12: Example of the peak pile-up effect for pulses for the (a) slow, and (b) fast signals measured using a ^{22}Na source. The pulses are separated by 2000 ns. For the slow signal, the superposition of these pulses are recorded as a single pulse by the acquisition system, which then records that signal as a count in the artificial 1786 keV peak (the sum of 511 keV and 1275 keV). For the fast signal, the 2000 ns time separation is sufficiently large such that the pulses do not interfere with each other, which results in two separate energy measurements being recorded.

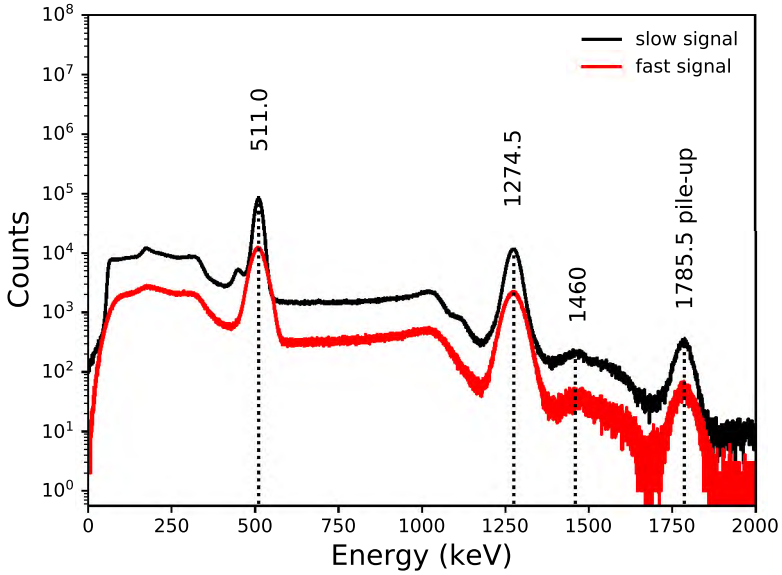

Fig. 4.13: Energy spectra of a 9 μCi ^{22}Na source placed 6 cm from a 2×2" $LaBr_3$:Ce detector for both the slow and fast signals. The usual gamma-ray peaks of 511 keV and 1275 keV are indicated, as well as the 1460 keV peak from the decay of ^{40}K in the background. Also indicated is the artificially-created 1786 keV peak produced from the pile-up of the 511 keV and 1275 keV signals. The 1786 keV pile-up peak is prominent in both the slow and fast signals.

is placed from the face of the detector. It is seen that $\mathcal{P}$ remains less than 3% over the observed range $\Omega = 0.00-0.14$ sr for each of the curves shown. This implies that less that 3% of 511 keV peak counts are 'lost' due to the peak pile-up effect. And so, this evidently shows that for this particular investigation, the peak pile-up effect is not a major factor that affects the measurement of 511 keV gamma-rays.

Despite the peak pile-up being on the order of a few percent, it is still important that this factor has been quantified, as this allows for the 'missing counts' in the 511 keV peak from the final measurements to be accounted for.

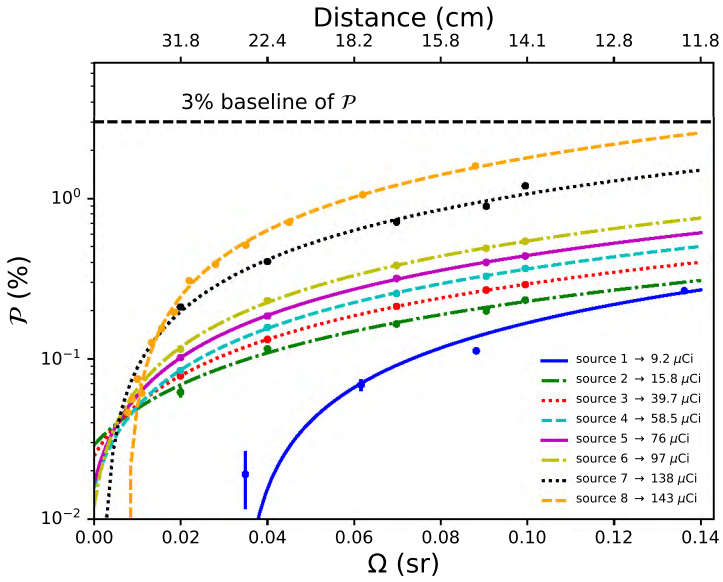

Fig. 4.14: The ratios between the counts in the 1786 keV and 511 keV peaks (denoted as $\mathcal{P}$) are shown as a function of Ω (and source-to-detector distance) for various ^{22}Na source activities. Sources of eight different activities were used to generate the data points (with their details tabulated in Table 4.4). $\mathcal{P}$ is seen to increase with both Ω and source activity, but evidently remains less than 3% over the observed range $\Omega = 0.00-0.14$ sr.

4.5 Dead time

The dead time of a detector system refers to the amount of time that the system is unable to record measurements due to the processing of incoming measurements of (usually) high count rates. It was noted in Fig. 4.9 that there were several artefacts that were present in the count rate spectrum due to dead time effects. These sections of dead time are likely caused by delays in the processing of the measurement data.

Typically when discussing dead time, there are two general models that are considered - namely paralyzable and nonparalyzable (both of which were discussed in Section 2.5.3). However, it does not appear that these artefacts in Fig. 4.9 are modelled by either of these, since it is clear from observation that they are not a consequence of high count rates (since they also appear in spectra where the count rates are relatively low).

In either case of high or low count rates, it's seen that these sections of dead time accumulate to a maximum of several seconds over a measurement time of several minutes. This means that the percentage of counts that are lost due to these dead time effects (or 'dead time losses') are, at most, less than 1%.

4.6 Considerations of E_{FEP} and $\mathcal{P}$ to determine an ideal detector geometry

In the previous sections, considerations were made of the full-energy peak efficiency E_{FEP} (Fig. 4.8 (a)) and the ratio $\mathcal{P}$ between the counts in the 1786 and 511 keV peaks (Fig. 4.14) as a function of source-to-detector distance for various source activities. However, it was mentioned in Section 4.4 that the maximum 511 keV 'count losses' due to the peak pile-up effect are small (less than 3%), and so it does not necessarily matter how $\mathcal{P}$ varies with any particular activity. It can thus be argued that maximising E_{FEP} becomes the most important factor to consider when selecting a source-to-detector distance for the geometry of the detector system.

To ensure a maximised E_{FEP}, the ^{22}Na source should be placed as close to the face of the detector as possible. However, there is a practical consideration which prevents the source from being placed any closer than 12 cm from the detector. When considering the experimental set-up with each of the eight detectors in place (as in Fig. 4.15), it becomes clear that due to the construction of the detector braces that holds each detector in place, the closest that the detectors are able to be situated symmetrically around the ^{22}Na source is at a source-to-detector distance of 12 cm, which was the geometry used for the main measurements of this work (see Section 3.1).

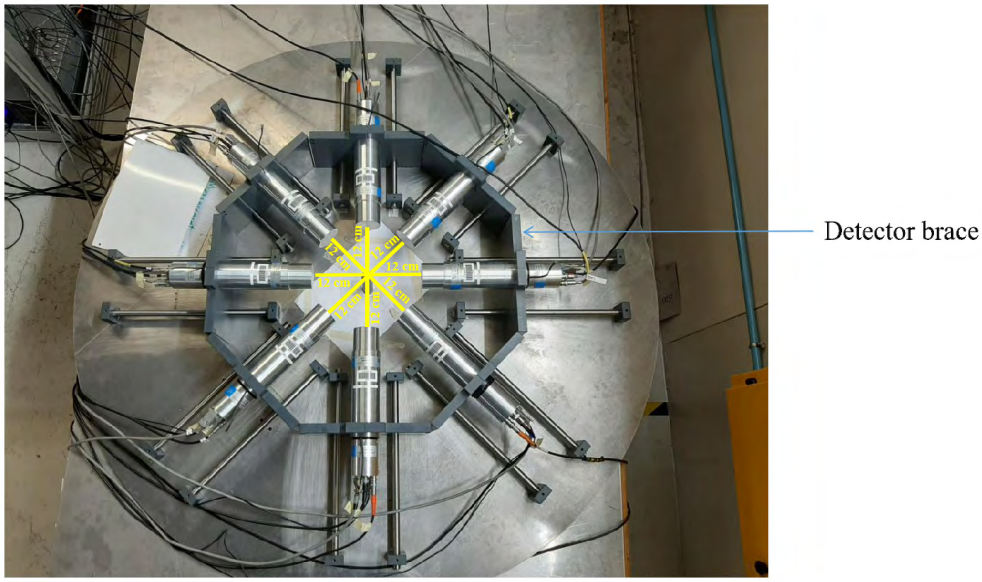

Fig. 4.15: Eight 2×2" $LaBr_3$:Ce detectors situated symmetrically around a ^{22}Na source. Each detector is placed at the closest possible distance of 12 cm from the source. The detector braces (indicated in the figure) prevent the detectors from physically being placed any closer symmetrically around the source.

4.7 Selection of the activity of the ^{22}Na source for a given detector geometry

In Section 4.3, the 'effective activity' A_{eff} was defined in equation (4.8), as well as tabulated in Table 4.6 for the slow, fast and QDC signals. These values in Table 4.6 corresponded to the singles count rate that produced a 10% energy resolution at 511 keV for the slow signal. Using these A_{eff} values, along with the source-to-detector distance of 12 cm, the source activity $\mathcal{A} = A_{\text{eff}}/\Omega$ was determined. Table 4.7 shows A_{eff} with corresponding $\mathcal{A}$ for each of the slow, fast and QDC signals. This table provides the activities of the ^{22}Na sources that correspond to an average singles count rate of $\mathcal{C}_{\text{max}} = 5.100\ (25) \times 10^4$ cps for each of the slow, fast and QDC signals.

It should be noted that the activities in Table 4.7 were not used in the main measurements for this work (see Table 3.1) due to source availability.

Table 4.7: Effective activities (denoted A_{eff}) and the corresponding activities (denoted $\mathcal{A}$) for slow, fast and QDC signals. $\mathcal{A}$ is calculated from A_{eff}/Ω, where $\Omega = 0.1362\ (49)$ sr (which corresponds to a source-to-detector distance of 12 cm). These values correspond to an average singles count rate of $\mathcal{C}_{\text{max}} = 5.100\ (25) \times 10^4$ cps.

Signal	A_{eff} (μCi.sr)	$\mathcal{A} = A_{\text{eff}}/\Omega$ (μCi)
Slow	9.29 (17)	68.2 (28)
Fast	9.12 (13)	67.0 (26)
QDC	11.87 (15)	87.2 (33)

4.8 Summary

So to summarise the previous sections, when a source of activity $\mathcal{A}$ (shown in Table 4.7) is placed at a source-to-detector distance of 12 cm (or $\Omega = 0.1362\ (49)$ sr), the average singles count rate will be $5.100\ (25) \times 10^4$ cps, and the energy resolution of the slow signal will be 10% at 511 keV. The dead time losses will be less than 1% of all the detected counts, while the number of 511 keV counts lost due to the peak pulse pile-up effect will account for less than 3% of all detected 511 keV gamma-rays. From the measurements in Fig. 4.8 (a), it was seen that (for the case of a single detector) with a source-to-detector distance of 12 cm at 511 keV, $E_{FEP} = 0.37\ (6)\%$. And so, extending this E_{FEP} value to the eight detector system (such as the one described in Section 3.1 for the main measurements of this work), the total full-energy peak detection efficiency at 511 keV is given by,

$$E_{FEP,tot} = 8 \times 0.37\ (6)\% = 2.9\ (4)\%. \tag{4.13}$$

The assumption is that each detector of the eight detector system has identical detection efficiency, and so $E_{FEP,tot}$ can be obtained by multiplying the E_{FEP} of a single detector at a particular energy by a factor of 8.

5 Data processing, analyses and results

Presented in this section is the analysis of the list-mode data obtained from the main experiment of this work (described in Section 3.1 and Section 3.2). The data obtained from these measurements was analysed using a sorting code that was developed in the C programming language by myself and Dr. Pete Jones[2]. This sorting code filtered the data using the energy (E_c) and time (T_c) windows that were discussed in Section 3.6. From this data reduction process, two types of gated multiplicity spectra were produced. The spectra produced using the T_c window are referred to as T_c-gated, while the spectra produced using both the T_c and E_c windows are referred to as T_c-E_c-gated.

ROOT software (version ROOT 6.14/06) [41] was used to perform the majority of the analyses presented in this section, while Python (version Python 3.7.3) was used for the generation and plotting of the various spectra.

5.1 Generating multiplicity spectra

In order to effectively relate gamma-ray events measured at a specific energy within a specific time window for several pairs of detectors (as required for this investigation), multiplicity spectra were produced. These spectra account for events measured using several different combinations of detectors, and effectively assist with filtering out the event interactions relevant to this study.

5.1.1 Outline of sorting code used to produce multiplicity spectra

Using the E_c and T_c windows established in Section 3.6, multiplicity spectra were generated for several different combinations of pairs of $LaBr_3$:Ce detectors. The sorting code runs through each pair of $LaBr_3$:Ce detectors to determine whether the recorded events in each meet the timing and/or energy requirements defined by E_c and T_c. A typical run through the sorting code to generate the multiplicity spectra is summarised below:

- The time difference between events in detectors j and $k \geq j+1$ is calculated and calibrated such that the time difference peak is centred at some constant offset $t > 0$ (which is later set to 0 ns).
- If the time difference lies within the pre-defined time window T_c, a counter (denoted m_1) is incremented by 1. As the sorting code runs through each pair of detectors, m_1 will therefore be incremented by the number of detector pairs which have gamma-ray events measured in coincidence.
- The events in each detector j and k are then checked for whether they correspond to the annihilation photon energy. If they lie within the energy window defined by E_c, then a separate counter (denoted m_2) is incremented by 1. m_2 will be incremented by the number of detector pairs which have events measured both in coincidence and at the same energy as the annihilation photon.
- After the sorting code has run through each pair of detectors, the values of m_1 and m_2 are binned separately, which generates two different multiplicity plots. The plot that bins m_1 values (T_c-gated plot) shows the multiplicity for coincident gamma-ray events, while the plot that bins m_2 (T_c-E_c-gated plot) shows the multiplicity for coincident events measured at the energy of the annihilation photon.
- This algorithm is repeated until all of the recorded data is processed.

[2]Senior scientist at iThemba LABS, and co-supervisor of this Masters dissertation

As an illustrative example of the above process, let's assume x and y are natural numbers such that $x > y$. For a typical single run through the sorting code, if events recorded in x different pairs of detectors are deemed to be in coincidence, this would imply that $m_1 = x$. If only y of these coincident detector pairs are resultant from annihilation events, this implies that $m_2 = y$. As such, a count will be binned into bin number x for the T_c-gated plot, while a count will be binned into bin number y for the T_c-E_c-gated plot.

5.1.2 Multiplicity spectra

Fig. 5.1 shows both multiplicity plots (T_c-gated and T_c-E_c-gated) that were generated through the sorting code. The number of different detector pairs (or multiplicity) is denoted as $\mathcal{M}$ along the x-axis. As discussed in Section 3.6, the energy and time windows for these plots were set to ranges of $E_c = 80$ keV and $T_c = 2$ ns, respectively. T_c-gated and T_c-E_c-gated plots have been produced for each of the measurement series R01-R05 (see Table 3.1). It is noted that the counts of the T_c-E_c-gated plots are roughly a few orders of magnitude less than those of the corresponding T_c-gated plots. This observation is expected, since there are less data reduction restrictions placed on the generation of the T_c-gated spectra.

In order to avoid repetitive analysis on the spectra produced from each of the five measurement series, it is beneficial to combine the data in Fig. 5.1 through a summing process. This summing process was performed such that the counts in each of the respective five spectra in Fig. 5.1 (a) and (b) were summed on a bin-by-bin basis. These summed contributions are shown in Fig. 5.2.

It should be noted that the sorting code was written in such a way that these measured events were sorted into detector pair multiplicities. As such, the nature of this sorting allows for the use of the binomial formula,

$$\binom{n}{k=2} = \frac{n!}{k!(n-k)!} = \frac{n!}{2(n-2)!}, \tag{5.1}$$

where $k = 2$ because the code sorts the events into multiplicities of detector pairs. Equation (5.1) provides a relation between the number of detectors that detected an event to the bin number (or multiplicity $\mathcal{M}$) in which the event was placed. Hence, the case of $n = 2$ would correspond to the number of counts recorded between any two detectors, and is calculated as,

$$\binom{2}{2} = 1. \tag{5.2}$$

This shows that a pair of detectors has a multiplicity of $\mathcal{M} = 1$, and so all 2γ events will be recorded in bin number 1 of the T_c-E_c-gated plot. Excluding accidental background interactions, the majority of these 2γ events ($\sim 60\%$ for most materials [1]) are resultant from direct annihilation, while the rest arise from the 2γ decay of Ps. For ease of reference, the counts corresponding to $\mathcal{M} = 1$ in the T_c-E_c-gated plot are denoted as $N_{2\gamma}$.

For the case of four detectors, $n = 4$, and so equation (5.1) becomes,

$$\binom{4}{2} = 6. \tag{5.3}$$

So the case of four detectors has a multiplicity of $\mathcal{M} = 6$, and hence, all possible 4γ events (the majority of which are from the 4γ decay of Ps) will be recorded in bin number 6 of the T_c-E_c-gated plot. For ease of reference, the counts corresponding to $\mathcal{M} = 6$ in the T_c-E_c-gated plot are denoted as $N_{4\gamma}$. The counts corresponding to other $\mathcal{M}$ values are resultant from other detector multiplicities that are not of interest to this work.

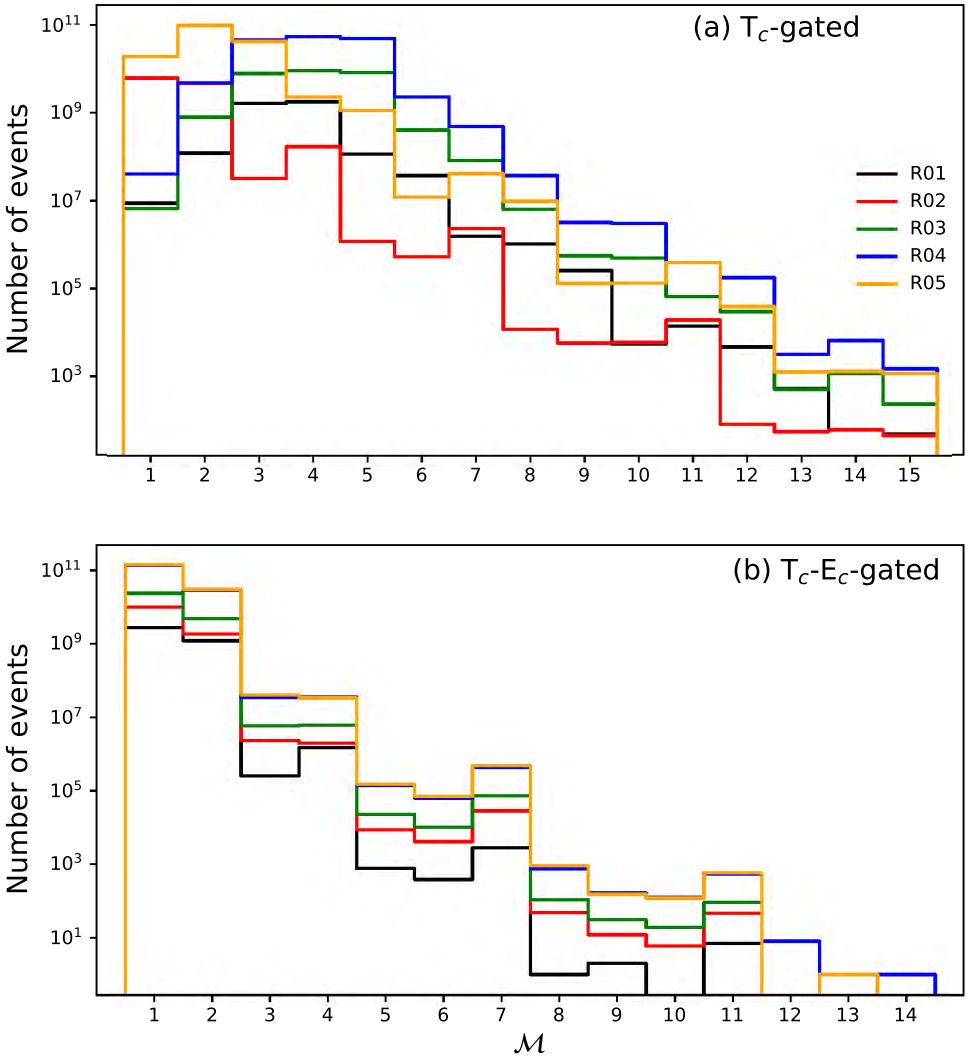

Fig. 5.1: The multiplicity ($\mathcal{M}$) is shown for both (a) T_c-gated, and (b) T_c-E_c-gated spectra produced from the measurement series R01-R05 (see Table 3.1). The time window was set to a range $T_c = 2$ ns, while the energy window was set to $E_c = 80$ keV.

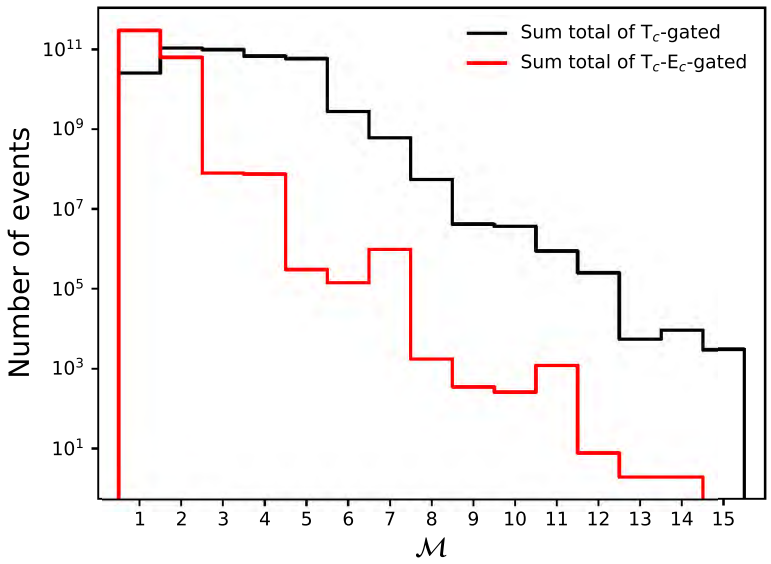

Fig. 5.2: $\mathcal{M}$ is shown for the summed contributions of both the T_c-gated (black), and T_c-E_c-gated (red) spectra. These summed contributions are resultant from the summing on a bin-by-bin basis of the T_c-gated and T_c-E_c-gated spectra obtained from each of the five measurement series R01-R05.

Table 5.1 highlights the key results obtained from the T_c-E_c-gated plot of Fig. 5.2, specifically $N_{2\gamma}$ and $N_{4\gamma}$, which are used for the 4γ branching ratio calculation in Section 5.3. The uncertainties presented are resultant from the uncertainties introduced by the selection of window values for E_c and T_c (systematic). These uncertainty calculations are shown in the following section.

Table 5.1: The values for $N_{2\gamma}$ (corresponding to the counts in $\mathcal{M} = 1$) and $N_{4\gamma}$ (corresponding to the counts in $\mathcal{M} = 6$) from the T_c-E_c-gated plot of Fig. 5.2 are highlighted as key results.

N	$\mathcal{M}$	**Number of counts**
$N_{2\gamma}$	1	3.02 (21) $\times 10^{11}$
$N_{4\gamma}$	6	1.45 (55) $\times 10^{5}$

5.2 Uncertainty analysis of counts in the multiplicity spectra

There are two types of uncertainties identified when considering the uncertainty of the counts of the multiplicity spectra in Fig. 5.2. These include the uncertainty from the coincident counting of event multiplicities (statistical), and the selection of window filter values for E_c and T_c (systematic). For this analysis, the statistical uncertainty is neglected, since it was found that the systematic uncertainty was significantly larger (by several orders of magnitude). It should also be mentioned that the relatively long measurement period of this work (highlighted in Section 5.3.2) reduces the statistical noise of the measurement, and hence, the systematic uncertainty is the main contribution to the uncertainty of the counts in Fig. 5.2.

5.2.1 Using several different range values for E_c and T_c (systematic uncertainty)

The effects of using several different range values for E_c and T_c in the sorting code are investigated in this section. The T_c-E_c-gated spectra that are resultant from these variations are discussed and compared. For practical purposes, only the effects on the T_c-E_c-gated spectra of measurement series R01 are considered, since R01 corresponds to the shortest experimental run with the least amount of measurement data to process (see Table 3.1).

For the data reduction of this work, the energy and time windows were set to $E_c = 80$ keV and $T_c = 2$ ns, respectively. For this reason, the counts corresponding to these filter conditions are used as reference values.

The findings from this uncertainty analysis are extended to the data obtained from the whole measurement series (R01-R05).

5.2.1.1 Varying E_c with fixed $T_c = 2$ ns

Table 5.2 lists the various E_c ranges that were considered with a fixed $T_c = 2$ ns. It should be noted that these ranges are all centred around the 511 keV photon annihilation energy peak. Fig. 5.3 (a) provides an illustration of these E_c ranges over a typical 511 keV peak that was measured in these experiments.

Table 5.2: The various E_c range values that were used in the sorting code (with a fixed $T_c = 2$ ns). Also shown are the start and end range values for E_c, which is visually represented in Fig. 5.3 (a).

Start range of E_c (keV)	**End range of E_c (keV)**	**E_c (keV)**
491	531	40
471	551	80
451	571	120
421	601	180

Fig. 5.3 (b) shows the T_c-E_c-gated spectra of R01 filtered using the various E_c range values. It is seen that varying E_c has significant effects on how the measured data is distributed in the binning process. In particular, this study is interested in the counts recorded in bin $\mathcal{M} = 1$ (i.e. $N_{2\gamma}$) and bin $\mathcal{M} = 6$ (i.e. $N_{4\gamma}$). Table 5.3 provides a comparison of $N_{2\gamma}$ and $N_{4\gamma}$ for each E_c range value. The reference counts (corresponding to $E_c = 80$ keV and $T_c = 2$ ns) are noted as,

$$N_{2\gamma,ref} = 2.6319 \times 10^9, \tag{5.4}$$

and,

$$N_{4\gamma,ref} = 381. \tag{5.5}$$

Table 5.3: The values for $N_{2\gamma}$ and $N_{4\gamma}$ resulting from Fig. 5.3 (b) are shown in relation to their corresponding E_c range value. The time window has been fixed to $T_c = 2$ ns.

		Number of counts			
$\mathcal{M}$	**N**	$E_c = 40$ **keV**	$E_c = 80$ **keV**	$E_c = 120$ **keV**	$E_c = 180$ **keV**
1	$N_{2\gamma}$	2.9381×10^9	2.6319×10^9	2.5941×10^9	2.5831×10^9
6	$N_{4\gamma}$	191	381	432	466

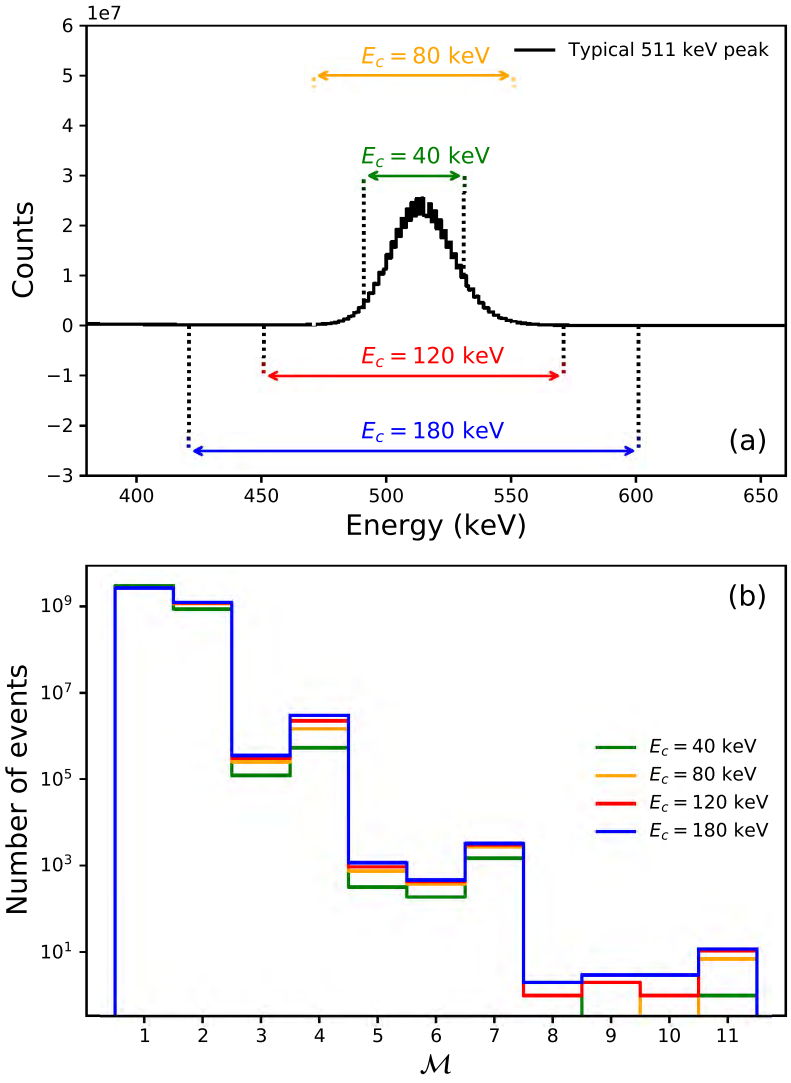

Fig. 5.3: (a) shows the various E_c range values used in the sorting code (40 keV, 80 keV, 120 keV and 180 keV) over a typical 511 keV photon annihilation peak. (b) shows the T_c-E_c-gated spectra of R01 that corresponds to each of the selected E_c range values with fixed $T_c = 2$ ns.

In order to quantify the variation between the counts observed in Table 5.3, a 'standard deviation' of the reference values is defined as,

$$\sigma_{n\gamma} = \sqrt{\frac{\sum_{i=1}^{3}(N_{n\gamma,i} - N_{n\gamma,ref})^2}{3}}, \tag{5.6}$$

where the summation is performed over the three non-reference counts. Equation (5.6) provides a suitable method to estimate the uncertainty contribution from varying the E_c filters. Performing the calculation using the values in Table 5.3, it is found that,

$$\sigma_{2\gamma,E_c} = 1.8038 \times 10^8, \tag{5.7}$$

and,

$$\sigma_{4\gamma,E_c} = 124. \tag{5.8}$$

5.2.1.2 Varying T_c with fixed $E_c = 80$ keV

Table 5.4 lists the various T_c ranges that were considered with a fixed $E_c = 80$ keV. These T_c ranges are centred around an arbitrary constant offset $t > 0$. Fig. 5.4 (a) provides an illustration of these T_c ranges over a typical time difference peak. In this case, the constant offset was calibrated such that $t = 0$.

Table 5.4: The various T_c range values that were used in the sorting code (with a fixed $E_c = 80$ keV). Also shown are the start and end range values for T_c (centred around an arbitrary constant offset $t > 0$), which is visually represented in Fig. 5.4 (a).

Start range of T_c (ns)	**End range of T_c (ns)**	**T_c (ns)**
$t - 0.5$	$t + 0.5$	1
$t - 1$	$t + 1$	2
$t - 2$	$t + 2$	4
$t - 3$	$t + 3$	6

Fig. 5.4 (b) shows the T_c-E_c-gated spectra of R01 filtered using the various T_c range values. As in the case of varying E_c, it is seen that varying T_c also has significant effects on how the measured data is binned. Table 5.5 provides a comparison of $N_{2\gamma}$ and $N_{4\gamma}$ for each T_c range value.

Table 5.5: The values for $N_{2\gamma}$ and $N_{4\gamma}$ resulting from Fig. 5.4 (b) are shown in relation to their corresponding T_c range value. The energy window has been fixed to $E_c = 80$ keV.

		Number of counts			
$\mathcal{M}$	**N**	$T_c = 1$ **ns**	$T_c = 2$ **ns**	$T_c = 4$ **ns**	$T_c = 6$ **ns**
1	$N_{2\gamma}$	2.6724×10^9	2.6319×10^9	2.6311×10^9	2.6309×10^9
6	$N_{4\gamma}$	360	381	277	316

Similar to the previous section, equation (5.6) can be used to estimate the uncertainty contribution from varying the T_c filter. Performing the calculation using the values in Table 5.5, it is found that,

$$\sigma_{2\gamma,T_c} = 2.3406 \times 10^7, \tag{5.9}$$

and,

$$\sigma_{4\gamma,T_c} = 72. \tag{5.10}$$

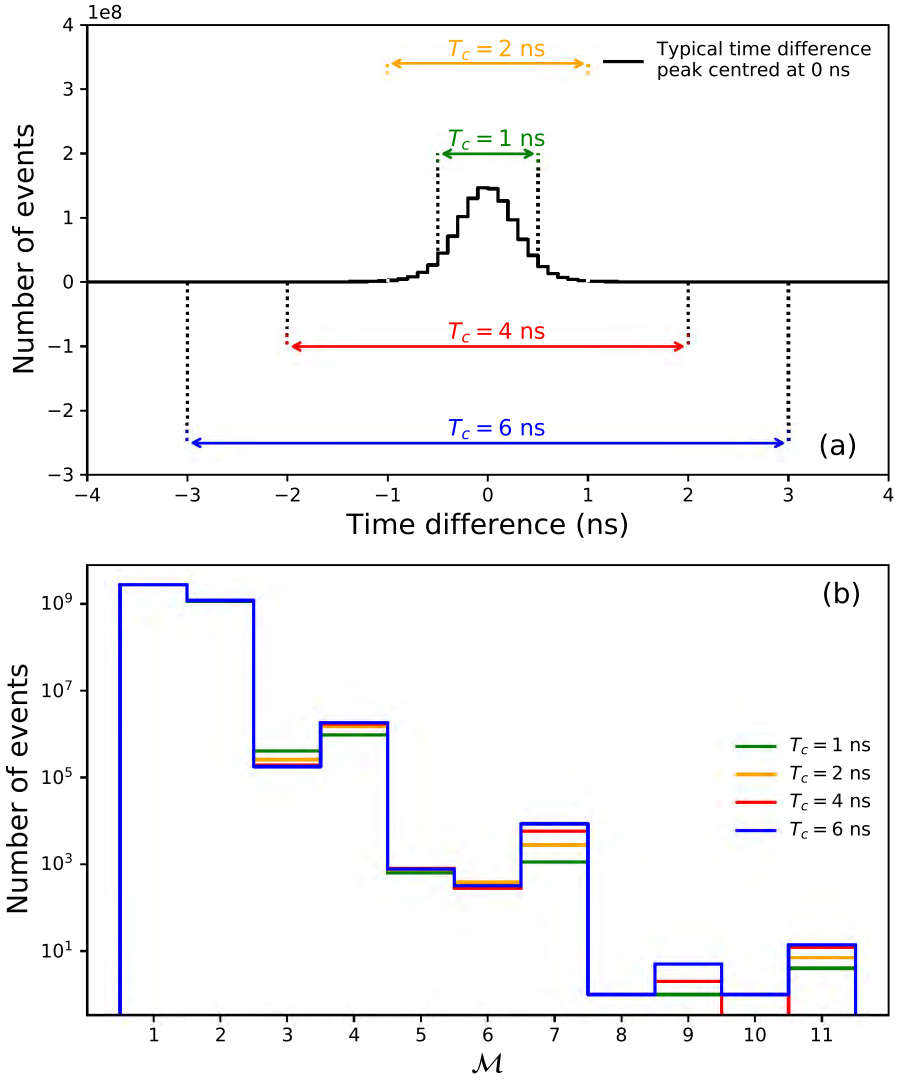

Fig. 5.4: (a) shows the various T_c range values used in the sorting code (1 ns, 2 ns, 4 ns and 6 ns) over a typical time difference peak centred at 0 ns. (b) shows the T_c-E_c-gated spectra of R01 that corresponds to each of the selected T_c range values with fixed $E_c = 80$ keV.

5.2.2 Combination of uncertainties and extension to larger measurement

Table 5.6 provides a summary of the uncertainty estimations obtained from the previous section (namely, equations (5.7), (5.8), (5.9), and (5.10)). These uncertainties are combined as the sum of the squares using,

$$\sigma_{n\gamma,total} = \sqrt{\sigma^2_{n\gamma,E_c} + \sigma^2_{n\gamma,T_c}}. \tag{5.11}$$

Equation (5.11) combines the uncertainty contributions from the selection of the E_c filter ($\sigma_{n\gamma,E_c}$) and T_c filter ($\sigma_{n\gamma,T_c}$) to produce a *total* uncertainty ($\sigma_{n\gamma,total}$) for the reference counts $N_{n\gamma,ref}$. Performing the calculations with the values in Table 5.6, it is found that,

$$\sigma_{2\gamma,total} = 1.819 \times 10^8, \tag{5.12}$$

and,

$$\sigma_{4\gamma,total} = 143. \tag{5.13}$$

Table 5.6: Summary of the uncertainty estimations of $N_{2\gamma}$ and $N_{4\gamma}$ for varying filter conditions.

Filter that was varied	**Uncertainty estimate**	
	$N_{2\gamma}$	$N_{4\gamma}$
E_c	1.8038×10^8	124
T_c	2.3406×10^7	72

Factoring in the above uncertainties, $N_{2\gamma,ref}$ (5.4) and $N_{4\gamma,ref}$ (5.5) become,

$$N_{2\gamma,ref} = 2.63\ (18) \times 10^9, \tag{5.14}$$

and,

$$N_{4\gamma,ref} = 3.8\ (14) \times 10^2. \tag{5.15}$$

In the assumption that this uncertainty analysis remains valid for the entire measurement series[3] (R01-R05), it is expected that the uncertainties of the counts for R01 is proportional to the uncertainties of the counts for the entire measurement series. Equations (5.14) and (5.15) show that there is a 7% and 38% uncertainty for $N_{2\gamma,ref}$ and $N_{4\gamma,ref}$, respectively. Hence, the uncertainties for $N_{2\gamma}$ and $N_{4\gamma}$ also correspond to 7% and 38%, as was shown in Table 5.1.

[3]The only significant change between measurement run R01 and the rest of the measurement series (R02-R05) was the use of a stronger source (see Table 3.1). While this change had the effect of increasing the count rate of the detector system, there is no reason to believe it would have an effect on the data reduction process performed post-acquisition.

5.3 Calculations and discussion

This subsection presents the main outcome from this study - the calculation of the four-photon branching ratio of p-Ps (denoted as $\mathrm{BR}_{4\gamma}$). From similar experiments, there have been five previous measurements of $\mathrm{BR}_{4\gamma}$ [8–12], and these are compared to measurement and experiment of this work.

5.3.1 Branching ratio of four-photon decay of parapositronium

In their paper, Vetter & Freedman [12] determined $\mathrm{BR}_{4\gamma}$ using,

$$\mathrm{BR}_{4\gamma} = \frac{(N_{4\gamma} - B_{4\gamma})\epsilon_{2\gamma}}{N_{2\gamma}\epsilon_{4\gamma}}. \tag{5.16}$$

where $N_{n\gamma}$ represents the number of $n\gamma$ events observed, $B_{4\gamma}$ is the expected number of 4γ background events, and $\epsilon_{n\gamma}$ is the detection efficiency of the detector array for $n\gamma$ annihilations. (5.16) is derived from the ratio between the number of detected 4γ events with the number of detected 2γ events (both normalised with their respective detection efficiencies). Lastly, the correction term $B_{4\gamma}$ accounts for the accidental detections of 4γ background events.

In Table 5.1, the values for $N_{2\gamma}$ and $N_{4\gamma}$ were highlighted as key results from the T_c-E_c-gated plot of Fig. 5.2. In order to complete the calculation of (5.16), what remains now is to obtain estimate values for $B_{4\gamma}$, $\epsilon_{2\gamma}$ and $\epsilon_{4\gamma}$. Looking back at previous measurements of $\mathrm{BR}_{4\gamma}$, Adachi *et al.* [8, 10], von Busch *et al.* [9], Yang *et al.* [11], and Vetter & Freedman [12] evaluated these quantities (or similar) by performing Monte Carlo detector simulations for their respective experiments. Such simulations are beyond the scope of the current work, and is suggested as follow up. However, there is presently enough information to provide a suitable estimate of $\mathrm{BR}_{4\gamma}$ using this work's measured values for $N_{2\gamma}$ and $N_{4\gamma}$. At its most fundamental level, (5.16) is essentially the ratio between the number of detected 4γ events with the number of detected 2γ events. Neglecting the secondary considerations of 4γ background subtraction and efficiency normalisations, a suitable 'first order' approximation for $\mathrm{BR}_{4\gamma}$ can be obtained as,

$$\mathrm{BR}_{4\gamma} \sim \frac{N_{4\gamma}}{N_{2\gamma}} = 4.8\ (19) \times 10^{-7}. \tag{5.17}$$

While this result is not a true measurement of $\mathrm{BR}_{4\gamma}$, it does seem to be a fairly promising estimation. The accepted value for $\mathrm{BR}_{4\gamma}$ was shown in Section 2.2 to be given by [6, 18],

$$\mathrm{BR}_{4\gamma,theory} = 1.4388\ (21) \times 10^{-6}, \tag{5.18}$$

which is a factor of 3 from the estimate in equation (5.17).

5.3.2 Comparison with measurements of previous experiments

With the estimate of equation (5.17) obtained, it is beneficial to compare the experiment and estimate result of this work to those of previous measurements from similar experiments. Table 5.7 provides a list of all previous measurements of $\mathrm{BR}_{4\gamma}$ with their corresponding authors and publication dates. Also shown are the measurement periods and total events recorded from each of the respective experimental campaigns, which are contrasted against those of this work. It should be noted that information for some of these experiments were not provided in their publication, and these have been indicated with a dash. It is seen that this work's measurement period compares well with those of the previous measurements, as it was significantly longer than the measurement periods of von Busch *et al.* and Vetter & Freedman, but shorter than Adachi *et al.* and Yang *et al.* It is also seen that the number of events recorded for this work

Table 5.7: Previous measurements of the 4γ branching ratio of p-Ps are shown in terms of the authors who published the result, the publication year, measurement period, total events recorded and their respective measurements of $BR_{4\gamma}$. Also shown and compared is the result and measurement details of this work.

Author	**Year of publication**	**Measurement period (hours)**	**Total events recorded**	**$BR_{4\gamma}$ ($\times 10^{-6}$)**
Adachi *et al.* [8]	1990	–	1.2×10^{12} e^+	1.30 (35)
von Busch *et al.* [9]	1994	480	4.9×10^{10}	1.50 (11)
Adachi *et al.* [10]	1994	4400	3.8×10^{12} e^+	1.48 (18)
Yang *et al.* [11]	1996	5611	–	1.19 (26)
Vetter & Freedman [12]	2002	263	1.18×10^{10}	1.14 (39)
Measurement of this dissertation		1433	5×10^{11}	~ 0.48 (19)

was greater than those recorded by both von Busch *et al.* and Vetter & Freedman, but less than the number of positrons measured in both measurements by Adachi *et al.*

To further aid in the comparisons, Fig. 5.5 illustrates the timeline of the performed measurements of $BR_{4\gamma}$, along with the 'first order' estimate of this work given by equation (5.17). It is seen that each of the previous measurements are in agreement with the accepted QED value given by equation (5.18). It is unsurprising that the estimated result from this work is not in agreement with the QED value (or any of the previous measurements), since several simplifying assumptions were made in its calculation. Undoubtedly, the accuracy of this result would increase with the inclusion of the neglected factors ($\epsilon_{2\gamma}$, $\epsilon_{4\gamma}$ and $B_{4\gamma}$) in the calculation of equation (5.16).

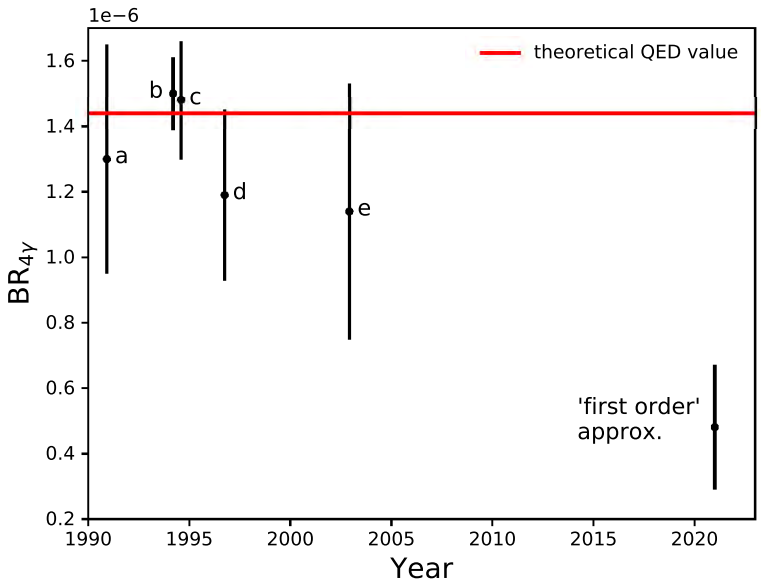

Fig. 5.5: Comparison of previous measurements of the 4γ branching ratio of p-Ps with the approximate first order result of this work. These measurements are shown by the year of publication. (a = Adachi *et al.* [8], b = von Busch *et al.* [9], c = Adachi *et al.* [10], d = Yang *et al.* [11], and e = Vetter & Freedman [12]).

6 Summary and further work

The aim of this study was to demonstrate the measurement feasibility of the four-photon branching ratio of p-Ps (denoted $BR_{4\gamma}$) using the experimental set-up described in Section 3. A complete calculation of $BR_{4\gamma}$ was not performed, since key factors from equation (5.16) (specifically $B_{4\gamma}$, $\epsilon_{2\gamma}$ and $\epsilon_{4\gamma}$) were not evaluated. However, key results for $N_{2\gamma}$ and $N_{4\gamma}$ (see Table 5.1) were obtained through the generation of multiplicity spectra that allowed for the separation of the data into a binned distribution (the process of which was outlined in Section 5.1.1). The ratio between the values of $N_{4\gamma}$ and $N_{2\gamma}$ allowed for an order of magnitude to be estimated for $BR_{4\gamma}$ given by,

$$BR_{4\gamma} \sim 5\ (2) \times 10^{-7}.$$

This estimation was compared to the accepted QED value, as well as previous measurements from similar experiments, and was found to differ by a factor of 3.

There are several possible avenues for further work and/or improvement on this study. The most obvious limitation of this work is the lack of a final measurement result for $BR_{4\gamma}$. An improvement, therefore, would be to evaluate the factors $B_{4\gamma}$, $\epsilon_{2\gamma}$ and $\epsilon_{4\gamma}$ using Monte Carlo simulations for this work's experimental set-up. Factoring in these additional results using equation (5.16) will allow for a complete calculation to be performed, and will provide a conclusive measurement of $BR_{4\gamma}$ (comparable to the literature values quoted).

A possible extension to this work includes an investigation of the other branching ratios of Ps using Fig. 5.2. While the analyses of this study only consider $N_{2\gamma}$ and $N_{4\gamma}$ from the T_c-E_c-gated plot, the counts corresponding to other multiplicities could be used in separate analyses. For example, all possible 3γ events (including those resulting from the 3γ decay of o-Ps) are recorded in bin $\mathcal{M} = 3$ of the T_c-E_c-gated plot, which presents an opportunity for further analyses to determine the 3γ branching ratio.

A further improvement would be to use a detector system structure which does not inherently limit the source-to-detector distance. In Section 4.6, it was argued that the most important factor to consider when choosing the detector geometry was maximising the full-energy peak efficiency (E_{FEP}) of the detector system. In order to maximise E_{FEP}, this meant choosing a minimum source-to-detector distance such that each of the eight $LaBr_3$:Ce detectors in the detector system was placed symmetrically from the radioactive source. However, it was shown in Fig. 4.15 that there was an inherent physical limitation on this distance, since the detector braces (which holds each detector in place) only allowed for a minimum source-to-detector distance of 12 cm.

Finally, it is recommended that further investigation is performed on the selection of the energy (E_c) and time (T_c) windows that are set in the sorting code of the data. The uncertainty analyses presented in Section 5.2.1 show that the values of these windows have significant effects on the values obtained for $N_{2\gamma}$ and $N_{4\gamma}$, which will clearly have an impact on the calculated value for $BR_{4\gamma}$. This work used fixed window values of $E_c = 80$ keV and $T_c = 2$ ns. However, the values for these windows were chosen fairly arbitrarily by inspection, and there is undoubtedly scope for a more sophisticated selection of these values to be performed.

A Appendix

Table A.1: Gamma-ray emission energies from ^{22}Na and ^{152}Eu radioactive sources with their respective intensities. These intensities show the number of photons produced at energy E_γ per 100 disintegrations. Only energies with $I_\gamma > 0.1\%$ have been tabulated.

Source	E_γ **(keV)**	I_γ **(%)**
^{22}**Na** [7]	511	180.7 (2)
	1274.537 (7)	99.94 (13)
^{152}**Eu** [43]	121.7817 (3)	28.41 (13)
	244.6974 (8)	7.55 (4)
	295.9387 (17)	0.442 (3)
	329.425 (21)	0.129 (6)
	344.2785 (12)	26.59 (12)
	367.7891 (20)	0.862 (5)
	411.1165 (12)	2.238 (10)
	416.048 (8)	0.1090 (17)
	443.965 (3)	2.80 (2)
	488.6792 (20)	0.4139 (24)
	503.474 (5)	0.1533 (18)
	563.990 (7)	0.457 (13)
	566.442 (5)	0.131 (4)
	586.265 (3)	0.462 (4)
	656.489 (5)	0.1437 (18)
	674.675 (3)	0.170 (4)
	678.623 (5)	0.470 (4)
	688.670 (5)	0.841 (6)
	719.349 (4)	0.268 (13)
	764.900 (9)	0.190 (4)
	778.9045 (24)	12.97 (6)
	810.451 (5)	0.317 (3)
	841.574 (5)	0.163 (2)
	867.380 (3)	4.243 (23)
	919.337 (4)	0.429 (5)
	926.317 (15)	0.273 (4)
	963.390 (12)	0.1341 (20)
	964.079 (18)	14.50 (6)
	1005.272 (17)	0.665 (23)
	1084 (1)	0.244 (8)
	1085.837 (10)	10.13 (10)
	1089.737 (5)	1.73 (1)
	1109.174 (12)	0.186 (4)
	1112.076 (3)	13.41 (6)
	1212.948 (11)	1.416 (9)
	1249.938 (13)	0.186 (3)
	1292.778 (19)	0.104 (3)
	1299.142 (8)	1.633 (9)
	1408.013 (3)	20.85 (8)
	1457.643 (11)	0.498 (4)

References

[1] Castellaz P, Siegle A and Stoll H 2002 *Journal of Nuclear and Radiochemical Sciences* **3** R1–R7

[2] Mogensen O and Jacobsen F 1982 *Chemical Physics* **73** 223–234

[3] Fermi E and Yang C N 1949 *Physical Review* **76** 1739–1743

[4] Wolfenstein L and Ravenhall D G 1952 *Physical Review* **88** 279–282

[5] Harpen M D 2003 *Medical Physics* **31** 57–61

[6] Czarnecki A and Karshenboim S G 1999 (*Preprint* hep-ph/9911410)

[7] Bé M M, Chisté V, Dulieu C, Mougeot X, Browne E, Chechev V, Kuzmenko N, Kondev F, Luca A, Galán M, Nichols A, Arinc A and Huang X 2010 *Table of Radionuclides* (*Monographie BIPM-5* vol 5) (Pavillon de Breteuil, F-92310 Sèvres, France: Bureau International des Poids et Mesures) ISBN 92-822-2234-8

[8] Adachi S, Chiba M, Hirose T, Nagayama S, Nakamitsu Y, Sato T and Yamada T 1990 *Physical Review Letters* **65** 2634–2637

[9] von Busch H, Thirolf P, Ender C, Habs D, Köck F, Schulze T and Schwalm D 1994 *Physics Letters B* **325** 300–307

[10] Adachi S, Chiba M, Hirose T, Nagayama S, Nakamitsu Y, Sato T and Yamada T 1994 *Physical Review A* **49** 3201–3208

[11] Yang J, Chiba M, Hamatsu R, Hirose T, Matsumoto T and Yu J 1996 *Physical Review A* **54** 1952

[12] Vetter P A and Freedman S J 2002 *Physical Review A* **66** 052505

[13] Coleman P G 2000 *Positron beams and their applications* (World Scientific)

[14] Procházka I 2001 *Materials Structure* **8** 55

[15] Brandt W 1983 *Proceedings of the International School of Physics Enrico Fermi*

[16] Kobayashi Y, Haraya K, Kamiya Y and Hattori S 1992 *Bulletin of the Chemical Society of Japan* **65** 160–163

[17] Mogensen O and Eldrup M 1977 Positronium bloch function, and trapping of positronium in vacancies, in ice Tech. rep. Risoe National Lab.

[18] Vetter P A 2004 *Modern Physics Letters A* **19** 871–885

[19] Knoll G F 2000 *Radiation Detection and Measurement* 3rd ed (New York: Wiley) ISBN 0-471-07338-5

[20] Sempere Roldan P 2011 *Quality control and preparation of the PWO crystals for the electromagnetic calorimeter of CMS* Ph.D. thesis Santiago de Compostela U.

[21] Martin J and Wen C D 2006 *Medical Physics* **33** 4773–

[22] Lilley J 2001 *Nuclear Physics* (Wiley) ISBN 978-0-471-97936-4

[23] Gilmore G 2008 *Practical gamma-ray spectrometry* (Chichester, England Hoboken, NJ: Wiley) ISBN 9780470861981

[24] Derenzo S, Weber M, Bourret-Courchesne E and Klintenberg M 2003 *Nuclear Instruments and Methods in Physics Research Section A: Accelerators, Spectrometers, Detectors and Associated Equipment* **505** 111–117

[25] 2013 Photomultiplier tube and scintillator image URL https://commons.wikimedia.org/wiki/File:PhotoMultiplierTubeAndScintillator.svg

[26] Ogundare F O, Oniya E O and Balogun F A 2008 *Pramana* **70** 863–874

[27] Cooper P N 2011 *Introduction to Nuclear Radiation Detectors* (Cambridge University Press) ISBN 9780521281324

[28] Limkitjaroenporn P, Hongtong W, Kim H J and Kaewkhao J 2018 *Journal of Physics: Conference Series* **970** 012016

[29] Leutz H, Schulz G and Van Gelderen L 1966 *Nuclear Instruments and Methods* **40** 257–260

[30] Tsipenyuk Y M 2009 *Physical methods, instruments and measurements* (Eolss Publishers Company Limited)

[31] Etim I, Obu J and Ushie O 2012 *Lat.-Am. J. Phys. Educ.* **6**

[32] Löher B, Savran D, Fiori E, Miklavec M, Pietralla N and Vencelj M 2012 *Nuclear Instruments and Methods in Physics Research Section A: Accelerators, Spectrometers, Detectors and Associated Equipment* **686** 1 – 6 ISSN 0168-9002

[33] van Loef E, Dorenbos L, van Eijk C, Krämer K and Güdel H 2001 *IEEE Transactions on Nuclear Science* **48** 341–345

[34] van Loef E, Dorenbos L, van Eijk C, Krämer K and Güdel H 2001 *Applied physics letters* **79** 1573–1575

[35] Vedia V, Mach H, Fraile L, Udías J and Lalkovski S 2015 *Nuclear Instruments and Methods in Physics Research Section A: Accelerators, Spectrometers, Detectors and Associated Equipment* **795** 144–150

[36] Chaudhuri S D, Banerjee D, Bhattacharjee T, Raja S W, Acharya R and Pujari P K 2020 *Journal of Radioanalytical and Nuclear Chemistry* **324** 829–835

[37] XIA 2005 *User's Manual Digital Gamma Finder (DGF) PIXIE-16* URL http://www.phys.utk.edu/expnuclear/LeRIBSS/Pixie16_UserManual1.0.6.pdf

[38] Jones P 2013 ithemba labs annual report URL https://tlabs.ac.za/wp-content/uploads/pdf/annual_reports/Annual_Report_2013_small.pdf

[39] Midas website URL http://npg.dl.ac.uk/MIDAS/

[40] Lmfit: Non-linear least-squares minimization and curve-fitting for python URL https://lmfit.github.io/lmfit-py/

[41] Brun R and Rademakers F 1997 *Nuclear Instruments and Methods in Physics Research Section A: Accelerators, Spectrometers, Detectors and Associated Equipment* **389** 81–86 ISSN 0168-9002 new Computing Techniques in Physics Research V

[42] Root: Tmath namespace reference guide URL https://root.cern/root/html606/namespaceTMath.html

[43] Bé M M, Chisté V, Dulieu C, Browne E, Chechev V, Kuzmenko N, Helmer R, Nichols A, Schönfeld E and Dersch R 2004 *Table of Radionuclides* (*Monographie BIPM-5* vol 2) (Pavillon de Breteuil, F-92310 Sèvres, France: Bureau International des Poids et Mesures) ISBN 92-822-2207-1

[44] Saint-Gobain-Crystals 2016 Efficiency calculations for selected scintillators URL https://www.crystals.saint-gobain.com/sites/imdf.crystals.com/files/documents/efficiency-calculations.pdf

[45] NIST-XCOM Photon cross sections database URL https://physics.nist.gov/PhysRefData/Xcom/html/xcom1.html

[46] Berger M, Hubbell J, Seltzer S, Chang J, Coursey J, Sukumar R, Zucker D and Olsen K 1987 Xcom-photon cross sections database, nist standard reference database 8

[47] Mouhti I, Elanique A, Messous M, Belhorma B and Benahmed A 2018 *Journal of Radiation Research and Applied Sciences* **11** 335–339

[48] Thilagam L, Priya M R and Mohapatra D K 2015 *Radiation Protection and Environment* **38** 130

[49] Novković D, Đurašević M, Kandić A, Vukanac I, Šešlak B and Milošević Z 2016 *Applied Radiation and Isotopes* **107** 138–144